

# **Aspects of Designing Efficient Interfacial Solar Steam Generators for Freshwater and Electricity Production**

**Thesis submitted for the award of the Degree**

**of**

**Doctor of Philosophy**

**in the Department of Physics**

**By**

**Tawseef Ahmad Wani**

**(2018RPH0029)**

**Under the supervision of**

**Dr. Ashok Bera**



विद्याधनं सर्वधनं प्रधानम्

भारतीय प्रौद्योगिकी  
संस्थान जम्मू

INDIAN INSTITUTE OF  
TECHNOLOGY JAMMU

**Indian Institute of Technology**

**Jammu**

**February 2023**

## Declaration

I hereby declare that the matter embodied in this thesis entitled "**Aspects of Designing Efficient Interfacial Solar Steam Generators for Freshwater and Electricity Production**" is the result of investigations carried out by me in the Department of Physics, Indian Institute of Technology, Jammu, India, under the supervision of **Dr. Ashok Bera** and it has not been submitted elsewhere for the award of any degree or diploma, membership, etc. In keeping with the general practice of reporting scientific observations, due acknowledgments have been made whenever the work described is based on the findings of other investigators. Any omission that might have occurred due to oversight or error in judgment is regretted. A complete bibliography of the books and journals referred in this thesis is given at the end of each chapter.

February 2023  
Indian Institute of Technology, Jammu

Tawseef Ahmad Wani  
2018RPH0029

## **Certificate**

This is to certify that the work presented in this thesis entitled "**Aspects of Designing Efficient Interfacial Solar Steam Generators for Freshwater and Electricity Production**" submitted by Tawseef Ahmad Wani, bearing enrolment 2018RPH0029, Department of Physics, Indian Institute of Technology, Jammu, for the award of the degree of Doctor of Philosophy (Ph.D.) is wholly based on his work under my supervision. The contents of the thesis, neither full nor any part of it, have been submitted to any other institute for any diploma, degree, or academic award.

Dr. Ashok Bera  
(Supervisor)

## Abstract

Freshwater scarcity is becoming a daunting challenge to the sustainable development of human society due to unsustainable economic practices, demographic changes, and rapid urbanization. Interfacial solar steam generation (ISSG) technology has provided a potential answer to this challenge by delivering an eco-friendly and low-cost method of freshwater production. This technique extracts steam from water using solar light as the sole energy source with the assistance of photothermal materials. The present work mainly discusses the development of the critical components for achieving high evaporation performance, including photothermal materials, structural designs, and thermal insulators, and designed a proper condensation setup for efficient steam condensation to achieve the final goal of freshwater collection. The work also sheds some light on a simple yet efficient strategy for synergistic electricity production in an ISSG system.

Initially, the thesis presents the preparation of a cylindrical evaporator made from flamed coconut husk (FCH). The high light absorption caused by the porous structure and the external heat harvesting capability helps the FCH-based evaporator to achieve a maximum evaporation rate of  $3.5 \text{ kg m}^{-2} \text{ h}^{-1}$  under 1 sun illumination, along with corresponding evaporation efficiency of above 100%. The lack of a proper approach for salt rejection in this device led to the further development of a conical evaporator made from filter paper coated with nanoparticles of direct and narrow bandgap  $\text{LaMO}_3$  ( $M = \text{Ni, Co}$ ). The combined effect of the high light absorption ( $\sim 95\%$ ) of  $\text{LaMO}_3$  and the conical structure results in a moderate evaporation rate of  $\sim 2.4 \text{ kg m}^{-2} \text{ h}^{-1}$  for both materials under 1 sun illumination. Through proper water flow management, the salt crystals deposit on the top edges and some portions of the outer surface and eventually fall under gravity during the night-time, thus providing a solution for the problem of salt clogging with the extra advantage of salt harvesting.

Maintaining a proper water supply under high salinity or high solar intensity becomes a problem in a long-run operation using the conical evaporator made of filter papers. To rectify such issue permanently, a design with separate evaporation and absorption surfaces was developed, in which the  $\text{LaMO}_3$  material was coated on a stainless steel sheet, and the filter paper was wrapped from the outside. With this design, the device shows an optimized evaporation rate of  $1.4 \text{ kg m}^{-2} \text{ h}^{-1}$  under 1 sun illumination at the salt concentration of 20 wt% for five days of continuous operation. Also, the evaporation rate increases linearly with increasing solar intensity. To achieve the final goal of water collection, the conical evaporator with separated evaporation and light-absorbing surfaces was used in a cylinder-shaped copper

condenser to avoid the optical losses otherwise present in conventional solar stills. By sending water from the reservoir to the evaporator surface through the condenser surface via cotton cloth, the device offers a collection rate of  $1.4 \text{ L m}^{-2} \text{ h}^{-1}$  under 1 sun illumination, leading to about 100% collection to evaporation rate ratio. Because of its low cost, simple design technique, and high collection-to-evaporation rate ratio, this device provides a step forward for utilizing the ISSG technique toward practicality.

Finally, the thesis discusses two approaches of simultaneous production of all-day-long electricity and freshwater by exploiting the water-conducting channels. In the first approach, four 2-legged filter paper strips with electrodes at the two side ends were connected to a conical evaporator, in which the saltwater was conducted through one leg and regular tapwater through another. The open-circuit voltage ( $V_{OC}$ ) of 150 mV across the electrodes was produced for 3.5 wt% of salt concentration, which increases to 250 mV for 20 wt% concentration. The device achieved a  $V_{OC}$  of 920 mV with a power density of  $9.9 \text{ mW m}^{-2}$  by connecting all four strips in series. In the second approach, four strips of filter paper are attached to the four outer walls of a cuboidal evaporator with an illumination area of  $1.5 \times 1.5 \text{ cm}^2$ . When salt water of 20 wt% concentration is conducted, each strip produces a  $V_{OC}$  of 750 mV. The device shows a  $V_{OC}$  of 2.7 V when all four strips are connected in a series combination and enough power to run some functional appliances without using any energy storage device or any scaling up of the device. Therefore, the results of this thesis promote ISSG as a promising alternative to the solar-driven water-energy nexus.

# Acknowledgements

## *All praises to the Allah, the Creator and Sustainer of the worlds*

In the pursuit of this academic endeavor, I feel I have been singularly fortunate. I will fail in my duty if I do not record my profound sense of indebtedness and heartfelt gratitude to my supervisor, *Dr. Ashok Bera*, Department of Physics, Indian Institute of Technology (IIT) Jammu, whose inspiration, guidance, and constant support have been invaluable throughout the course of this work. His understanding and expertise in my research area greatly improved this thesis's contents.

I would like to thank the Department of Physics IIT Jammu for providing me the experimental facilities and the financial support that made this work possible. A special thanks to the committee members *Dr. Rahul R. Salunkhe* and *Dr. Pankaj Chauhan* for their part played in carrying this work through to completion. I have benefitted immensely from their acute remarks, comments, and suggestions on how to improve my work.

I thank my lab mate, *Parul Garg*, for her utmost cooperation, selfless help, and endless moral support during my research. I want to express my special obligation to my dearest colleagues *Nitish Kumar*, *Ved P. Joshi*, *Priya Kaith*, *Prakash K. Pathak*, and *Neetu Bansal* for their encouragement and maintaining a friendly atmosphere.

I am also thankful to my Ph.D. batchmates *Dr. M. Ayoub Sofi*, *Burhan Wafai*, *Kamal*, *Dr. Mehran M. Zargar*, *Ajaz A. Mir*, *Suhaib-ul-Reyaz*, *Abdul H. Wani*, *Harsh V. Singh*, *Javid Ahmad*, *Inayatullah* and *Sakal Singla* for their company and help during my time in IIT Jammu.

Finally, the ones who believed in me and provided unconditional love, care, sacrifice, and blessing throughout my studies, my beloved family. It's my mother, *Shareefa Banoo*, and my father, *Gull Mohd Wani*, who brought me up and supported me in becoming the person I want to be. I also acknowledge my elder brothers *Imtiyaz A. Wani*, *Nisar A. Wani*, and *Aijaz A. Wani* without their love, support, and affection, this work would not have seen the light of the day. I also want to thank my other family members for being so supportive while I was working on my thesis.

Lastly, I want to thank my teachers, friends and all the other elders who have contributed to what I am today.

Tawseef Ahmad Wani

(2018RPH0029)

# Contents

|   |              |
|---|--------------|
| <b>Contents</b>   | <b>vii</b>   |
| <b>List of Figure</b>   | <b>xi</b>    |
| <b>List of Tables</b>   | <b>xvii</b>  |
| <b>List of Abbreviations</b>  | <b>xviii</b> |
| <br>  |              |
| <b>1. Introduction to Interfacial Solar Steam Generation</b>            | <b>1-8</b>   |
| 1.1. Historical background.....   | 2            |
| 1.2. Why solar steam generation?.....                                   | 2            |
| 1.3. Why interfacial solar steam generation?.....                       | 4            |
| 1.4. Motivation of the thesis.....                                      | 5            |
| 1.5. Organization of the thesis.....                                    | 6            |
| 1.6. References.....  | 7            |
| <br>  |              |
| <b>2. Basics of Interfacial Solar Steam Generation</b>                  | <b>9-33</b>  |
| 2.1. Introduction.....  | 10           |
| 2.2. Evaporation performance of ISSG system.....                        | 10           |
| 2.3. Strategies to enhance evaporation efficiency/rate.....             | 11           |
| 2.3.1. Photothermal materials.....                                      | 12           |
| 2.3.2. Thermal management.....  | 14           |
| 2.3.2.1. Suppressing the thermal loss to the underlying water.....      | 15           |
| 2.3.2.2. Reducing the reflection loss.....                              | 16           |
| 2.3.2.3. Suppressing thermal loss to the surroundings.....              | 17           |
| 2.3.3. Absorbing thermal energy from the environment.....               | 17           |
| 2.3.4. Controlling the water transport.....                             | 18           |
| 2.3.5. Reducing the vaporization enthalpy.....                          | 19           |
| 2.4. Salt mitigation from the absorber surface.....                     | 20           |
| 2.4.1. Mechanical washing .....   | 20           |
| 2.4.2. Diffusion of salt ions back to the bulk water/self-cleaning..... | 21           |
| 2.4.3. Direct water resistance and salt ion repulsion.....              | 21           |
| 2.4.4. Site-specific salt discharge.....                                | 22           |

|   |              |
|---|--------------|
| 2.5. Condensation of the generated steam.....   | 23           |
| 2.6. Applications of ISSG.....  | 24           |
| 2.6.1. Desalination.....  | 25           |
| 2.6.2. Wastewater purification.....   | 25           |
| 2.6.3. Energy generation.....   | 26           |
| 2.7. References.....  | 27           |
| <br>  |              |
| <b>3. Synthesis and Characterization Techniques of Photothermal Materials</b>               | <b>34-46</b> |
| 3.1. Introduction.....  | 35           |
| 3.2. Synthesis of nanomaterials.....  | 35           |
| 3.3. Characterizations of photothermal materials.....                                       | 36           |
| 3.3.1. X-ray diffraction.....   | 37           |
| 3.3.2. Scanning electron microscopy.....  | 38           |
| 3.3.3. UV-vis-NIR spectroscopy.....   | 39           |
| 3.3.3.1. Analysis of liquid samples.....  | 40           |
| 3.3.3.2. Analysis of powder samples.....  | 40           |
| 3.3.3.3. Band gap energies analysis.....  | 41           |
| 3.3.4. Fourier transform infrared spectroscopy.....   | 42           |
| 3.3.5. X-ray photoelectron spectroscopy.....  | 43           |
| 3.3.6. Brunauer-Emmett-Teller analysis.....   | 44           |
| 3.4. References.....  | 46           |
| <br>  |              |
| <b>4. Coconut Husk as Photothermal Material for Highly Efficient Solar Steam Generation</b> | <b>47-62</b> |
| 4.1. Introduction.....  | 48           |
| 4.2. Experimental section.....  | 49           |
| 4.2.1. Materials.....   | 49           |
| 4.2.2. Fabrication of FCH evaporator.....   | 49           |
| 4.2.3. Material characterizations.....  | 50           |
| 4.2.4. SSG measurements.....  | 50           |
| 4.3. Results and discussion.....  | 51           |
| 4.4. Conclusion.....  | 59           |
| 4.5. References.....  | 60           |

|  |               |
|--|---------------|
| <b>5. Materials and Designs Structures for Efficient Salt Rejection</b>  | <b>63-82</b>  |
| 5.1. Introduction.....   | 64            |
| 5.2. Experimental section.....   | 65            |
| 5.2.1. Materials.....  | 65            |
| 5.2.2. Preparation of LCO and LNO NPs.....   | 65            |
| 5.2.3. Preparation of LNO/LCO-based 2D and conical 3D devices.....   | 66            |
| 5.2.4. Material characterizations.....   | 66            |
| 5.2.5. SSG measurements.....   | 67            |
| 5.3. Results and discussion.....   | 67            |
| 5.4. Conclusion.....   | 80            |
| 5.5. References.....   | 80            |
| <br>   |               |
| <b>6. In-Situ Latent Heat Transfer for Nearly 100% Condensation in Single-Stage Interfacial Solar Steam Generation</b> | <b>83-93</b>  |
| 6.1. Introduction.....   | 84            |
| 6.2. Experimental section.....   | 85            |
| 6.2.1. Materials.....  | 85            |
| 6.2.2. Fabrication of solar water purifier.....  | 85            |
| 6.2.3. Material characterizations.....   | 86            |
| 6.2.4. SSG measurements.....   | 86            |
| 6.3. Results and discussion.....   | 86            |
| 6.4. Conclusion.....   | 91            |
| 6.5. References.....   | 91            |
| <br>   |               |
| <b>7. Simultaneous Freshwater and Electricity Generation in ISSG</b>   | <b>94-108</b> |
| 7.1. Introduction.....   | 95            |
| 7.2. Experimental section.....   | 96            |
| 7.2.1. Materials.....  | 96            |
| 7.2.2. Device fabrication.....   | 96            |
| 7.2.3. Material characterizations.....   | 97            |
| 7.2.4. Solar steam and electricity generation measurement.....   | 97            |
| 7.3. Results and discussion.....   | 97            |

|                                   |                |
|-----------------------------------|----------------|
| 7.4. Conclusion.....              | 106            |
| 7.5. References.....              | 107            |
| <b>8. Summary and Conclusions</b> | <b>109-113</b> |
| <b>List of publications</b>       | <b>114</b>     |

# List of Figures

|  |    |
|--|----|
| 1.1. Various forms of solar heating in SSG (a) bottom heating and (b) volumetric heating.....  | 3  |
| 1.2. ISSG system (a) without and (b) with thermal insulation layer.....  | 4  |
| 2.1. Schematic illustration of basics of ISSG.....   | 10 |
| 2.2. Schematic diagram of (a) 2D plane and (b) 3D conical structures of ISSG device showing the management of reflection loss in 3D.....   | 16 |
| 2.3. Schematic diagram of ISSG based on hydrogel showing three different water types—bound, intermediate, and free water.....  | 19 |
| 3.1. Reflection of X-rays from two planes of atoms in a solid.....   | 37 |
| 3.2. Schematic diagram of an FESEM.....  | 39 |
| 3.3. Block diagram of UV-vis-NIR spectrophotometer.....  | 40 |
| 3.4. Schematic illustration of measurement of diffuse reflectance of a (a) 2D film sample and (b) cone-shaped sample using an integrating sphere .....   | 41 |
| 3.5. Schematic diagram of FTIR spectrometer.....   | 42 |
| 3.6. Energy level diagram illustrates the basic XPS equation.....  | 44 |
| 3.7. Block diagram of BET setup.....   | 45 |
| 4.1. Photographs showing stepwise fabrication of FCH-based evaporator.....   | 49 |
| 4.2. (a) FTIR and (b) XPS survey spectra of FCH and RCH. High-resolution XPS spectra of (c) C1s orbitals of RCH, (d) C1s orbitals of FCH, (e) O1s orbitals of RCH and (f) O1s orbitals of FCH.....   | 51 |
| 4.3. SEM images of the FCH evaporator (a) side view and (b) top view. (c) SEM image of the top of a single fibre. (d) Schematic diagram showing the advantage of coconut coir in light absorption and steam escape. N <sub>2</sub> -adsorption/desorption isotherms of (e) RCH and (f) FCH. The insets show their respective multipoint BET curves.....  | 52 |
| 4.4. (a) Diffused reflectance spectra of dry and wet FCH. The solar irradiation spectrum is shown in a light blue area. The inset shows the diffused reflectance of the RCH. (b) Transient response of environmental temperature and top surface temperature after keeping the 2D evaporator in contact with water in the dark. The thermal image in the inset shows the spatial distribution of temperature after | 53 |

|   |    |
|---|----|
| saturation. (c) Time course of the surface temperature of dry and wet FCH under 1 sun and insets are IR thermal images of FCH in dry and wet states after 1 h of illumination. (d) IR thermal images of 3D FCH evaporator after 1 h of light illumination under 1, 2 and 3 sun.....   |    |
| 4.5. Mass change of (a) FCH evaporator with different heights under 1 sun illumination and (b) 2D and 3D FCH evaporators in the dark and 1 sun illumination. (c) Mass change of 3D FCH evaporator at higher intensities. (d) ER versus cycle number at a series of solar power intensities.....   | 56 |
| 4.6. Schematic diagram of the 3D FCH evaporator with radius 1 cm and length 6 cm showing the heat exchange with the environment.....  | 57 |
| 4.7. (a) Photograph for the side view (left) and top view (right) of the prototype of FCH based SSG system. UV-vis spectrum of (b) MB solution, (c) detergent, and soap water before and after purification. The respective insets show the photographs of the solutions before and after purification. (d) Retention of 3D FCH evaporator for saltwater for a duration of 10 h. The insets are the optical image of accumulated salt on 3D FCH evaporator's surface after 10 h under high solar intensity (left) and self-cleaned FCH under dark for another 10 h (right)..... | 58 |
| 5.1. Schematic illustration of the hydrothermal synthesis of LNO NPs.....   | 65 |
| 5.2. Schematic illustration of the preparation of 2D and conical 3D devices.....  | 66 |
| 5.3. Crystal structure of rhombohedral (a) LCO and (b) LNO. (c) X-ray diffraction pattern LCO and LNO NPs. FESEM images of (d) LCO and (e) LNO.....   | 68 |
| 5.4. EDS elemental mapping graphs of (a) La (b) Co (c) O of LCO and (d) La (e) Ni (f) O of LNO. EDS spectrum of (g) LCO and (h) LNO.....  | 68 |
| 5.5. XPS survey spectra of (a) LCO and (b) LNO. High resolution XPS spectrum of (c) La 3d, (d) Co 2p, (e) O 1s for LCO and (f) La 3d, (g) Ni 2p, (h) O 1s for LNO NPs.....  | 69 |
| 5.6. Band structure and PDOS plot of (a) LCO and (b) LNO, where the Fermi level is set at zero. In the band structure plot, the blue and yellow lines represent the spin-up and spin-down states. (c) Comparison of diffused reflectance spectra of commonly used photothermal materials with LNO and LCO. (d) Absorption spectra of the LCO and LNO. Inset shows the enlarged view of the diffused reflectance spectra for LCO and LNO.....  | 71 |

|  |    |
|--|----|
| 5.7. Diffused reflectance of 2D film shaped sample of (a) LCO and (b) LNO in both dry and wet conditions. Transient surface temperature response of the 2D (c) LNO and (d) LCO in dry and wet states under 1 sun illumination. The insets show the thermal images of the sample after saturation.....  | 72 |
| 5.8. (a) The conventional setup for 2D ISSG. (b) Cross-sectional FESEM image of absorber-coated filter paper. (c) Mass change of water using LCO and LNO-based evaporators and compared with that of water in the dark and under 1 sun illumination. (d) ER for two evaporators for continuous 10 cycles.....  | 73 |
| 5.9. (a) Diffuse reflectance spectra of dry and wet 3D cone-shaped LNO evaporator. The left inset shows the digital photograph of a typical arrangement for the 3D ISSG. Schematic of 2D (middle) and 3D (right) showing the advantage of 3D conical over 2D ISSG. (b) Mass change profile of eight different 3D ISSG devices using LNO absorber layer to calculate the average ER. (c) Mass change of water using 3D cone-shaped LNO-based evaporators and compared with that of conical pristine filter paper under 1 sun illumination. The insets show the IR thermal images of the cone after saturation. (d) Mass change of water using 3D cone-shaped LNO-based evaporators at different illumination intensities..... | 75 |
| 5.10. (a) ER of single-layered and double-layered 3D cone-shaped LNO evaporator under saltwater. (b) ER of the device made of filter paper with a lower water flow rate. Inset shows the digital photographs of the top and side view of the device before and after 12 h of continuous operation under saltwater. Digital photographs of single-layered 3D cone-shaped LNO evaporator (c) top view (d) side view after 12 h and (e) after putting overnight in the dark and double layered 3D cone shaped LNO evaporator (e) top view (f) side view after 12 h and (g) after putting overnight in the dark. (i) Mass change profile of LNO-cone for continuous 1-week operation.....  | 77 |
| 5.11. (a) Convention conical evaporator with absorbing surface acting as evaporation surface. (b) Impermeable conical evaporator with separated absorbing and evaporation surfaces. (c) Mass change profile of 3D impermeable cone for 1h under dark and 1 sun illumination. (d) ER of the 3D impermeable cone with varying solar intensity.....   | 78 |
| 5.12. Digital photographs of (a-c) the accumulated salt on the evaporator for four days of continuous operation under 20 wt% salt concentration and (d) mechanical   | 79 |

|   |    |
|---|----|
| salt removal. (e) Mass change profile water using a 3D impermeable cone for continuous 5 days.....  |    |
| 6.1. Schematic diagram of the solar water purifier.....   | 86 |
| 6.2. (a) Mass change profile of 3D impermeable cone for 1h under dark and 1 sun illumination. (b) UV-vis-NIR spectra of cone-shaped structure coated with different photothermal materials.....   | 87 |
| 6.3. Schematic of the solar water purifier when water is supplied from inside the condenser. (b) ER and CR of the purifier for 10 h of continuous operation under 1 sun illumination. (c) The temperature profile of the condenser surface and the generated steam under 1 sun illumination with inside water supply.....   | 88 |
| 6.4. Digital photographs of the (a) side and (b) top view of the actual purifier. (c) CR of the purifier with water supplied through the outer surface of the condenser under 1 sun illumination. d) CR of the purifier with different photothermal materials. (d) Comparison of CR of the purifier with recent reports. (f) Comparison of ER and CR of the device under high solar intensities. Inset shows the salt precipitation on the tip. (g) Continuous operation of the device for a week using simulated seawater of 3.5 wt% NaCl concentration..... | 89 |
| 6.5. Temperature profile of (a) the inside surface of the condenser, the generated steam, (b) the sink under 1 sun illumination, and (c) the outer condenser surface under dark and 1 sun illumination with water supply from outside.....  | 89 |
| 6.6. UV–vis spectrum of (a) MB and (b) MO solutions before and after purification and corresponding insets show the color images of MB and MO solutions before and after purification. Evaluation of water purity using a multimeter with a constant distance between electrodes for (c) saltwater and (d) purified water. (e) Ion concentration of seawater before and after purification.....   | 90 |
| 7.1. Schematic diagram of (a) a single two-legged strip showing the ionic concentration gradient perpendicular to the direction of fluid flow and (b) the two strips connected to the evaporator showing simultaneous generation of steam and electricity.....  | 98 |
| 7.2. (a) Photograph showing the setup for simultaneous voltage and steam generation. (b) Mass change curves under different illumination conditions. (c) Time response of $V_{OC}$ and $I_{SC}$ of the two individual strips. (d) Continuous operation of the device for 6 h in light, followed by 6 h in the dark, and (e) 8 days of continuous operation  | 99 |

of the device for both voltage and steam generation with 10 h in light, followed by 14 h in the dark. The blue dot in the voltage graph indicates the value in the morning (just before the light source was turned on), and the red dot represents the value in the evening (just before the light source was turned off).....

7.3. (a) Photograph of the dried strip after 10 h of continuous operation. (b) The SEM image shows the salinity gradient. EDX images showing the ionic concentration gradient for (c) Na and (d) Cl. (e) Time response of  $V_{OC}$  across the strip when solutions of different salt concentrations are transported in two legs. (f) Time response of  $V_{OC}$  across the strip with tap water on one leg and solutions of different ions flowed on the other..... 100

7.4. (a) The  $V_{OC}$  and  $I_{SC}$  of 4 strips connected in series, keeping one leg of every device at 20 wt% saltwater and tap water on the other. (b) Comparison of  $V_{OC}$  of our device with recent reports. (c) Current–voltage values of several individual strips and their series/parallel combinations. Variation of output (d) voltage and current, and (e) power density of the device measured as a function of external load resistance when all four strips were connected in series. (f) Voltage–time curves of 470 and 4700  $\mu F$  capacitors being charged by four strips in series, inset shows the screenshot of a video of a glowing red LED taken after connecting it across two charged capacitors (4700  $\mu F$ ) attached in parallel..... 101

7.5. (a) Schematic model of a cuboid-shaped freshwater-electricity generator with four filter paper strips attached to the outer surfaces. (b) Mass change curves of salt water under different illumination conditions. Time response of  $V_{OC}$  and  $I_{SC}$  of the device connecting all four strips in (c) parallel and (d) series. Insets of the respective figures show the device with the strips connected in parallel and series. (e) Continuous operation of the device for 6 h in the dark followed by 6 h under 1 sun illumination. (f) Time response of  $V_{OC}$  and  $I_{SC}$  for the device of height 5 cm with all four strips connected in series..... 102

7.6. Optical photographs of (a) glowing green LED and (b) calculator powered by the device with all the four strips connected in a series combination. (c) Photograph of the digital watch run by the device with two pairs of series-connected strips connected in parallel. Variation of output (d) voltage and current, and (e) power density of the device measured as a function of external load resistance when all four strips were connected in series..... 104

7.7. (a) Schematic illustration of electrolyte flow-induced streaming potential within a microchannel. (b) Variation of the  $V_{OC}$  against different strip widths. (c) Variation of the  $V_{OC}$  against different saltwater concentrations and the inset show the variation of  $V_{OC}$  with different materials. (d) Time response of  $V_{OC}$  with different flow rates originated from varying the ER with change in illumination intensities. (e) Measurement of  $V_{OC}$  and  $I_{SC}$  for different electrolyte solutions flowing through a single strip. (f) Time response of  $V_{OC}$  for a single strip with and without taping the whole strip under natural evaporation..... 105

# List of Tables

|  |     |
|--|-----|
| 4.1. Comparison of ER of the 3D-FCH evaporator with recently reported 3D evaporators at 1 sun solar intensity.....                           | 56  |
| 4.2. Conductivity and pH values of different contaminated solutions before and after purification compared with that of DI and RO water..... | 59  |
| 5.1. Comparison of ERs of LNO and LCO absorber-based evaporators with recently reported metal oxides.....                                    | 76  |
| 7.1. Comparison of the evaporation and electricity performances of devices with some recent reports.....                                     | 103 |

# List of Abbreviations

---

| Abbreviation | Description                                     |
|--------------|---|
| SSG          | Solar Steam Generation                          |
| ISSG         | Interfacial Solar Steam Generation              |
| ER           | Evaporation Rate                                |
| CR           | Collection Rate                                 |
| SS           | Stainless Steel                                 |
| SEM          | Scanning Electron Microscopy                    |
| FESEM        | Field Emission Scanning Electron Microscopy     |
| EDX          | Energy-Dispersive X-Ray                         |
| FTIR         | Fourier-Transform Infrared                      |
| XRD          | X-Ray Diffraction                               |
| XPS          | X-Ray Photoelectron Spectroscopy                |
| BET          | Brunauer-Emmett-Teller                          |
| JCPDS        | Joint Committee on Powder Diffraction Standards |
| HOMO         | Highest Occupied Molecular Orbital              |
| LUMO         | Lowest Unoccupied Molecular Orbital             |
| GO           | Graphene Oxide                                  |
| rGO          | reduced Graphene Oxide                          |
| CNTs         | Carbon Nanotubes                                |
| MWCNTs       | Multi-Walled Carbon Nanotubes                   |
| NPs          | Nanoparticles                                   |
| PPy          | Polypyrrole                                     |
| PVDF         | Polyvinylidene Fluoride                         |
| PET          | Polyethylene Terephthalate                      |
| WHO          | World Health Organization                       |
| EPA          | Environmental Protection Agency                 |
| MB           | Methyl Blue                                     |
| MO           | Methyl Orange                                   |
| TEG          | Thermoelectric Generator                        |
| LPG          | Liquefied Petroleum Gas                         |

---

---

|       |   |
|-------|---|
| FCH   | Flamed Coconut Husk                             |
| RCH   | Raw Coconut Husk                                |
| LCO   | $\text{LaCoO}_3$                                |
| LNO   | $\text{LaNiO}_3$                                |
| JCPDS | Joint Committee on Powder Diffraction Standards |
| GGA   | Generalized Gradient Approximation              |
| DFT   | Density Functional Theory                       |
| PDOS  | Partial Density of States                       |
| VBM   | Valence Band Maxima                             |
| CBM   | Conduction Band Minima                          |
| SSA   | Selective Solar Absorber                        |
| AAS   | Atomic Absorption Spectroscopy                  |

---

# Chapter 1

## **Introduction to Interfacial Solar Steam Generation**

Historical background

Why solar steam generation?

Why interfacial solar steam generation?

Motivation of the thesis

Organization of the thesis

References

## 1.1. Historical background

During the last few decades, freshwater scarcity has become a significant challenge to the sustainable development of human society because of the increasing demands caused by the growing population and improving living standards.<sup>[1,2]</sup> As per recent reports,<sup>[3-5]</sup> 66% of the global population currently faces severe water scarcity at least one month a year, and half a billion face it for a whole year.<sup>[6]</sup> Although 71% earth's surface is covered with water, only 3% is fresh, and the rest is too salty to drink. Therefore, converting seawater into freshwater is critical for solving global freshwater scarcity. Presently, more than twenty thousand global desalination plants produce over 13 million cubic meters of freshwater per day.<sup>[7]</sup> These plants are either membrane-based, like reverse osmosis and electrodialysis, or thermal-based, like multistage flash and multi-effect distillation. In membrane-based desalination, the saline water is passed through membranes via high-pressure pumps, whereas in thermal-based desalination, the saline water is evaporated by heating and then condensed to produce pure water.<sup>[8]</sup> These desalination technologies consume a tremendous amount of energy which mostly comes from fossil fuels.<sup>[9-11]</sup> The increasing demand-to-supply ratio of fossil-fuel-based energy and the generation of greenhouse gases during its production compelled researchers to find an alternate technology for seawater desalination. Therefore, various renewable energy sources, such as wind, biogas, and sunlight, have been utilized for freshwater production.<sup>[10]</sup>

Moreover, the simultaneous generation of freshwater and energy using any of these renewable energy resources will be an excellent strategy to deal with global energy and water challenges. Interestingly, the places with high water scarcity are located in regions with high solar radiation. Therefore, solar-powered desalination will be the most suitable approach for freshwater production. Some desalination systems, such as solar humidification-dehumidification and solar chimneys, are directly driven by solar energy.<sup>[12]</sup> But the low production capacity of these systems limits large-scale applications.<sup>[13]</sup> Hence finding cost-effective and efficient solar desalination technology is essential to overcome the upcoming global freshwater challenges. On the other hand, if the same technology can produce electricity during freshwater production, it can be an ideal solution for the global water-energy nexus.

## 1.2. Why solar steam generation?

Solar steam generation (SSG) is a technique where water is directly vapourised using solar light, and then the steam is condensed to generate freshwater. The development of SSG technology starts from the natural evaporation process in which the water absorbs sunlight and

converts it into vapor. Due to water's low light absorption (< 20%) ability, natural evaporation is inefficient.<sup>[14]</sup> The steam generation rate can be improved with the help of photothermal materials that absorb most of the incident solar light and convert it into thermal energy. In solar stills or solar ponds, which have been used since ancient times, the light absorption was increased by black painting the bottom of the water reservoir. The light absorber material at the bottom surface converts the absorbed light to heat which is then used to evaporate the water over it (Figure 1.1a). The heat produced by the bottom absorber layer is mainly used to increase the bulk water's temperature rather than wholly contributing to evaporation, resulting in low evaporation efficiency of 30-45%. Recently, volumetric heating has gained tremendous interest in reducing these surface heat losses, showing significant improvement in the steam generation rate by dispersing photothermal nanomaterials into bulk water (Figure 1.1b).<sup>[15,16]</sup> The enhancement of the evaporation performance of SSG is accredited to i) the advancement of nanotechnology that enabled the synthesis of efficient and low-cost photothermal materials and ii) the fast development in their synthesis and morphology. Due to the enhanced evaporation rate (ER), low-cost, simple design technique, and solar energy as the sole energy source, SSG has emerged as a promising alternative for freshwater production.<sup>[17-20]</sup> However, this system is also accompanied by various heat losses as the heat produced is wasted in increasing the temperature of the portion of bulk water that does not participate in vapor generation, leading to a moderate evaporation efficiency.

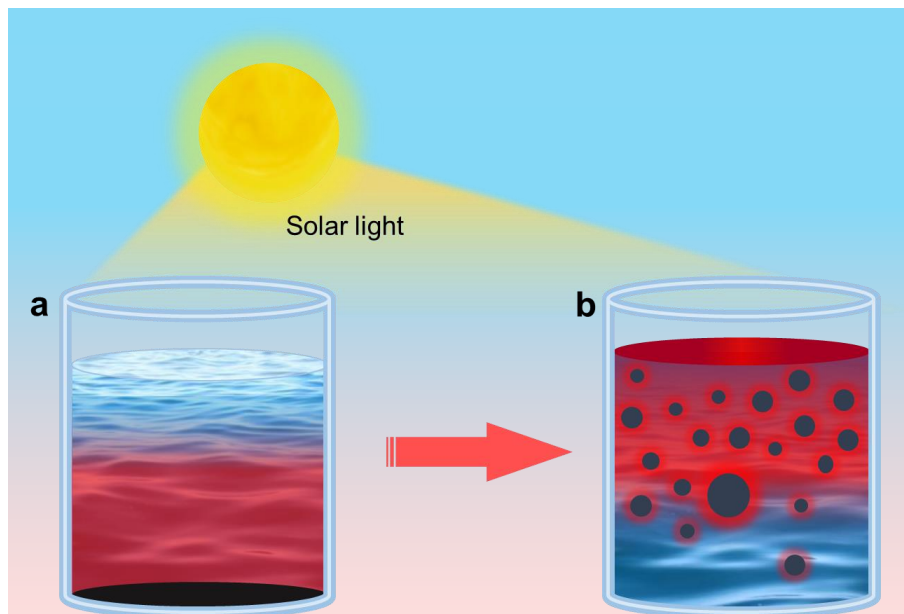


**Figure 1.1.** Various forms of solar heating in SSG (a) bottom heating and (b) volumetric heating.

### 1.3. Why interfacial solar steam generation?

The concept of interfacial solar steam generation (ISSG) was introduced to minimize volumetric heat losses in SSG and improve the ER.<sup>[2,21–23]</sup> In this approach, both sunlight collection and steam production occur at the air-water interface by placing a layer of photothermal material on the water surface (Figure 1.2a).<sup>[14]</sup> In such a structure, the generated heat is restricted over a thin layer to increase the temperature only at the surface and not the entire bulk water. This leads to the substantial reduction of conduction loss to the underlying bulk water, which was otherwise present in the case of volumetric heating. The ER was improved further by thermally separating the absorber layer from bulk water but linked via a confined water path (Figure 1.2b). In this way, the ISSG is independent of the quantity of the underlying bulk water hence can be assumed that the temperature of the bulk water remains close to the ambient temperature.

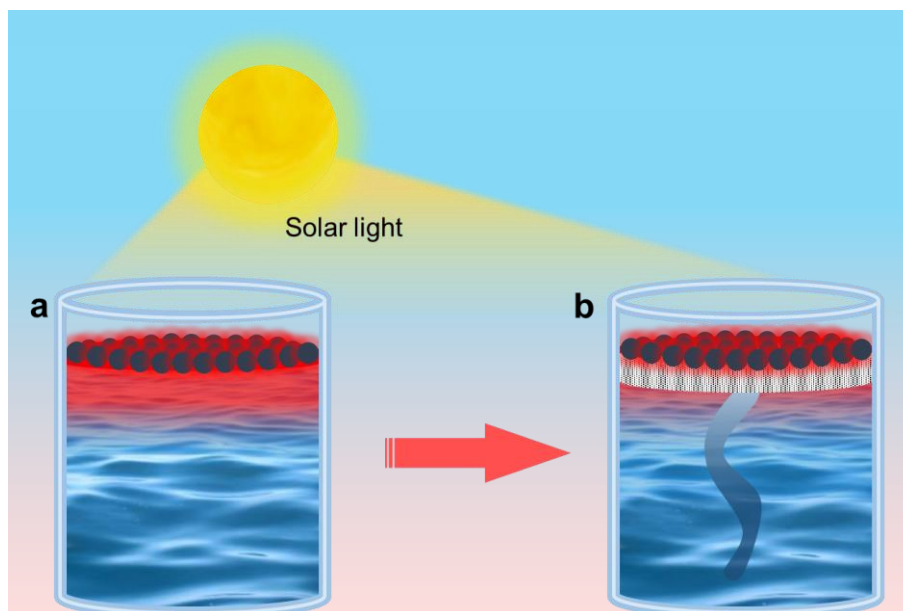


**Figure 1.2.** ISSG system (a) without and (b) with thermal insulation layer.

A typical ISSG system is usually a double-layered structure with a top photothermal layer placed on the water surface to absorb sunlight and then convert it into thermal energy via the photothermal effect. This layer is made to have high light absorption ability over the full range of solar spectrum and high light-to-heat conversion efficiency. The bottom layer performs two functions one is to transport water from bulk to the absorber surface through the interconnected channels present in it via capillary forces, and the second is to provide thermal insulation between the absorber surface and bulk water to reduce the heat losses. Generally, these types of systems are known as 2D ISSG. Furthermore, various materials, structural designs, and

fabrication methods have been extensively investigated to enhance ER and light-to-heat conversion efficiency. In addition to freshwater production, ISSG has also demonstrated enormous potential in various other applications, such as electricity generation, medical sterilization, salt collection, *etc.*, making it an ideal way of freshwater production using renewable energy resources.<sup>[24–27]</sup>

## **1.4. Motivation of the thesis**

The past decade has witnessed tremendous progress in developing novel photothermal materials for ISSG to enhance evaporation performance. The primary focus was on the materials having high light absorption ability over the full range of the solar spectrum. However, in conventional ISSG systems, when the light is incident on the surface of the solar absorber, some part reflects into the surrounding atmosphere and thus cannot be utilized for evaporation. In addition to the reflection loss, some amount of the generated heat is lost to the environment through radiation, convection, and conduction processes, leading to lower evaporation efficiency. Hence, the first motivation of this thesis is to find efficient photothermal materials and a suitable design architecture to achieve an optimized ER by effectively utilizing the available solar energy.

Further, the salt-resistant performance is one of the major concerns of the ISSG system for long-term desalination, especially when dealing with water sources of high salinity. During desalination, the water evaporates and leaves behind the dissolved salts on the absorber surface, which eventually not only blocks the incident light but also restricts the water transport and ultimately leads to lower evaporation performance.<sup>[28]</sup> To resolve such issues, researchers reported some thin structures with superhydrophobic surfaces to avoid salt precipitation but have compromised with the thermal insulation properties, eventually leading to high conduction heat losses.<sup>[29]</sup> Efforts have also been made to develop superior designs in which the salt precipitated in the daytime diffuses back to the bulk water in the night-time and thus leaves the absorber surface free from salt.<sup>[30,31]</sup> The back diffusion of the salt in the bulk water produces high-concentrated brine, which creates problems for the aquatic ecosystem and deprives the opportunity to extract valuable minerals.<sup>[7,32]</sup> Therefore, it is urgent to find a suitable device that can reduce thermal losses and address the salt-clogging problem to ensure long-term desalination performance with simultaneous salt harvesting, which is the second motivation of the thesis.

Although several efforts have been made to improve the ER of an ISSG system in the open atmosphere, efficient steam condensation and designing an integrated water production system remain significant challenges. Most of the reports, if not all, use a transparent top for the condensation of evaporated water, which found a considerable discrepancy between the ER and the final water collection rate (CR) due to inefficient condensation. This discrepancy is attributed to the blockage of sunlight by the condensed mist on the condenser surface, absorption of the portion of light by the inner steam layer, and increased humidity inside the closed chamber of the purifier. Therefore, the third motivation is developing an innovative design with an efficient water collection yield which is crucial to utilize ISSG at its full potential.

Among the other promising applications of ISSG, electricity generation has attracted considerable attention as it may provide renewable and decentralized clean water-electricity solutions that are especially useful for rural areas and developing countries. In this view, efforts have been reported for simultaneous electricity production using different forms of energy present in the ISSG system, like the internal enthalpy and kinetic energy of the generated steam, the temperature gradient created by interfacial evaporation, and the salinity gradient between the evaporation surface and bulk water. The electricity generated in such systems was not possible during the night-time because electricity production requires high illumination intensity to maintain a sufficient temperature or salinity gradient, which restricts their performance only to the light illumination time. Furthermore, the generated power was insufficient to continuously operate a practical device (like an LED) without using energy storage devices, limiting their large-scale application. Therefore, it is essential to find an alternative system that can produce sufficient power, regardless of the illumination conditions, to run functional appliances directly without using any energy storage devices, which is the final motivation of this thesis.

## **1.5. Organization of the thesis**

The work in this thesis is organized into eight chapters. The introduction presented in this chapter is followed by Chapter 2, which provides a review of the synthesis and characterization of nanomaterials for photothermal applications. Chapter 3 discusses a detailed summary of the recent developments, challenges, and applications of ISSG. Chapter 4 discusses the synthesis and characterizations of a low-cost carbon-based photothermal material derived from coconut husk and its evaporation performances. Chapter 5 presents the synthesis and characterizations

of LaMO<sub>3</sub> (M = Ni, Co) nanoparticles (NPs) and their application as photothermal materials in designing a cone-shaped evaporator for efficient salt rejection. In chapter 6, a complete solar water purification device is fabricated that condenses nearly 100% of generated steam and produces water at the rate of 1.4 L m<sup>-2</sup> h<sup>-1</sup> under 1 sun illumination. In chapter 7, a device capable of simultaneously producing freshwater and all-day-long electricity was developed, which had sufficient power to run a digital watch and a digital calculator continuously. Finally, the conclusion and the future scope of the work are presented in chapter 8.

## 1.6. References

- [1] N. Mancosu, R. Snyder, G. Kyriakakis, D. Spano, *Water* **2015**, 7, 975.
- [2] L. Zhu, M. Gao, C. K. N. Peh, G. W. Ho, *Nano Energy* **2019**, 57, 507.
- [3] L. Zhou, X. Li, G. W. Ni, S. Zhu, J. Zhu, *Natl. Sci. Rev.* **2019**, 6, 562.
- [4] C. Xiao, L. Chen, P. Mu, J. Jia, H. Sun, Z. Zhu, W. Liang, A. Li, *ChemistrySelect* **2019**, 4, 7891.
- [5] C. Zhang, H. Liang, Z. Xu, Z. Wang, *Adv. Sci.* **2019**, 6, 1900883.
- [6] M. M. Mekonnen, A. Y. Hoekstra, *Sci. Adv.* **2016**, 2, e1500323.
- [7] N. Shekarchi, F. Shahnia, *Int. J. Energy Res.* **2019**, 43, 1357.
- [8] H. Sharon, K. S. Reddy, *Renew. Sustain. Energy Rev.* **2015**, 41, 1080.
- [9] M. Höök, X. Tang, *Energy Policy* **2013**, 52, 797.
- [10] I. Dincer, C. Acar, *Int. J. Energy Res.* **2015**, 39, 585.
- [11] I. Capellán-Pérez, M. Mediavilla, C. de Castro, Ó. Carpintero, L. J. Miguel, *Energy* **2014**, 77, 641.
- [12] G. P. Narayan, J. H. Lienhard, in *Desalination*, John Wiley & Sons, Inc., Hoboken, NJ, USA, **2014**, pp. 425–472.
- [13] G. P. Narayan, M. H. Sharqawy, E. K. Summers, J. H. Lienhard, S. M. Zubair, M. A. A. Antar, *Renew. Sustain. Energy Rev.* **2010**, 14, 1187.
- [14] H. Ghasemi, G. Ni, A. M. Marconnet, J. Loomis, S. Yerci, N. Miljkovic, G. Chen, *Nat. Commun.* **2014**, 5, 4449.
- [15] X. Liu, Y. Xuan, *Nanoscale* **2017**, 9, 14854.
- [16] A. Lenert, E. N. Wang, *Sol. Energy* **2012**, 86, 253.
- [17] V. Kashyap, H. Ghasemi, *J. Mater. Chem. A* **2020**, 8, 7035.
- [18] M. R. Qtaishat, F. Banat, *Desalination* **2013**, 308, 186.
- [19] Z. Xu, Z. Li, Y. Jiang, G. Xu, M. Zhu, W.-C. Law, K.-T. Yong, Y. Wang, C. Yang, B.

- Dong, F. Xing, *J. Mater. Chem. A* **2020**, *8*, 25571.
- [20] F. He, X. Wu, J. Gao, Z. Wang, *J. Mater. Chem. A* **2021**, *9*, 27121.
- [21] P. Tao, G. Ni, C. Song, W. Shang, J. Wu, J. Zhu, G. Chen, T. Deng, *Nat. Energy* **2018**, *3*, 1031.
- [22] H. Liu, Z. Huang, K. Liu, X. Hu, J. Zhou, *Adv. Energy Mater.* **2019**, *9*, 1900310.
- [23] J. Li, M. Du, G. Lv, L. Zhou, X. Li, L. Bertoluzzi, C. Liu, S. Zhu, J. Zhu, *Adv. Mater.* **2018**, *30*, 1805159.
- [24] P. Yang, K. Liu, Q. Chen, J. Li, J. Duan, G. Xue, Z. Xu, W. Xie, J. Zhou, *Energy Environ. Sci.* **2017**, *10*, 1923.
- [25] Y. Zhang, S. K. Ravi, S. C. Tan, *Nano Energy* **2019**, *65*, 104006.
- [26] H. Jiang, L. Ai, M. Chen, J. Jiang, *ACS Sustain. Chem. Eng.* **2020**, *8*, 10833.
- [27] H. Wang, W. Xie, B. Yu, B. Qi, R. Liu, X. Zhuang, S. Liu, P. Liu, J. Duan, J. Zhou, *Adv. Energy Mater.* **2021**, *11*, 2100481.
- [28] G. Liu, T. Chen, J. Xu, G. Yao, J. Xie, Y. Cheng, Z. Miao, K. Wang, *Cell Reports Phys. Sci.* **2021**, *2*, 100310.
- [29] C. Chen, Y. Kuang, L. Hu, *Joule* **2019**, *3*, 683.
- [30] M. Zhu, Y. Li, F. Chen, X. Zhu, J. Dai, Y. Li, Z. Yang, X. Yan, J. Song, Y. Wang, E. Hitz, W. Luo, M. Lu, B. Yang, L. Hu, *Adv. Energy Mater.* **2018**, *8*, 1701028.
- [31] Y. Kuang, C. Chen, S. He, E. M. Hitz, Y. Wang, W. Gan, R. Mi, L. Hu, *Adv. Mater.* **2019**, *31*, 1900498.
- [32] C. Zhang, Y. Shi, L. Shi, H. Li, R. Li, S. Hong, S. Zhuo, T. Zhang, P. Wang, *Nat. Commun.* **2021**, *12*, 998.

## **Chapter 2**

### **Basics of Interfacial Solar Steam Generation**

Introduction

Evaporation performance of ISSG system

Strategies to enhance evaporation efficiency/rate

Salt mitigation from the absorber surface

Condensation of the generated steam

Applications of ISSG

References

## 2.1. Introduction

The advancement of nanotechnology has led researchers to shift their attention back to the old technology of solar-powered water evaporation due to the growing concern over environmental sustainability and energy demands.<sup>[1]</sup> Solar energy is a diffuse energy source, and this technology's primary motivation is to achieve a high-water ER using un-concentrated solar light with the help of photothermal nanomaterial and then condensing the evaporated steam without affecting the ER. In this chapter, we will first discuss the process to evaluate the performance of a solar evaporation system, followed by the recent developments to improve the ER and the condensation rate of ISSG, and finally, the additional application of SSG towards energy generation (Figure 2.1).

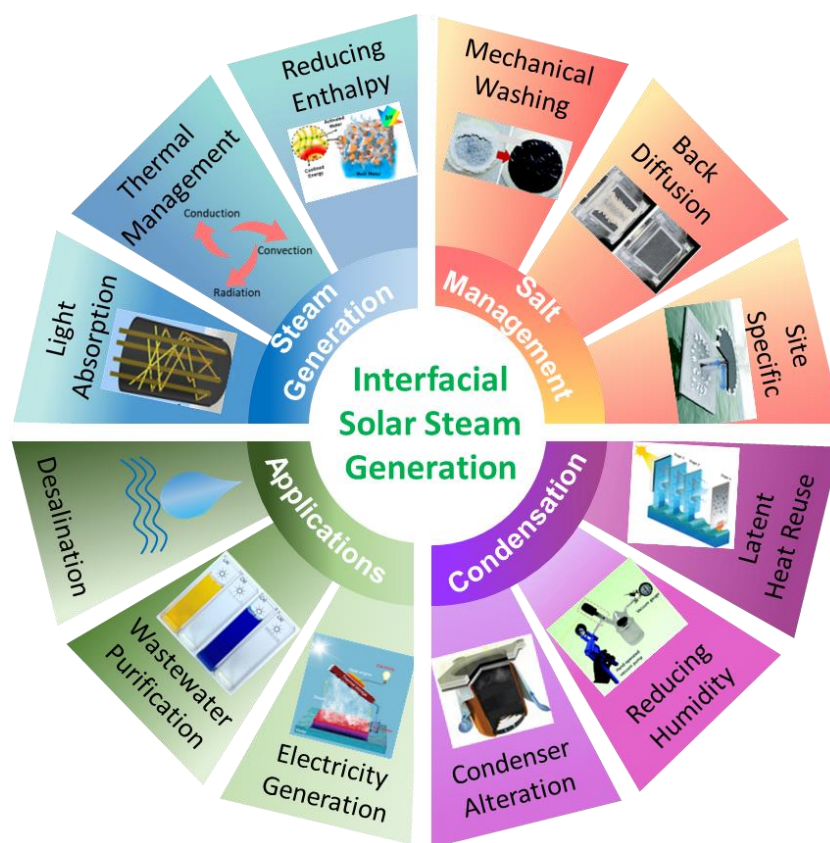


**Figure 2.1.** Schematic illustration of basics of ISSG.

## 2.2. Evaporation performance of ISSG system

The evaporation performance of an ISSG system is evaluated by its capacity to evaporate under solar illumination and is assessed by a parameter called evaporation efficiency. The

evaporation efficiency ( $\eta$ ) is defined by the ratio of the amount of thermal energy used for water evaporation ( $q_{eva}$ ) to the total incident solar light input ( $q_{in}$ ), and is given as follows<sup>[2]</sup>

$$\eta = \frac{q_{eva}}{q_{in}} = \frac{\dot{m}h_{LV}}{C_{opt}P_{in}} \quad (2.1)$$

Where  $\dot{m}$  ( $= \dot{m}_{light} - \dot{m}_{dark}$ ) is the solar-driven ER of water under solar illumination,  $C_{opt}$  is the optical concentration,  $P_{in}$  is the solar irradiation under 1 sun ( $1 \text{ kW m}^{-2}$ ) illumination, and  $h_{LV}$  made up of specific heat and enthalpy of vaporization is calculated as

$$h_{LV} = C_s \Delta T + \Delta h \quad (2.2)$$

where  $C_s$  ( $= 4.18 \text{ J g}^{-1} \text{ K}^{-1}$ ) is the specific heat capacity of water and  $\Delta T$  is the increase in water's temperature, and  $\Delta h$  is the enthalpy of vaporization on relative temperatures. The value of  $\Delta h$  depends mainly on temperature, and the value ( $2257 \text{ kJ kg}^{-1}$ ) at  $100 \text{ }^\circ\text{C}$  is usually used in the calculations.<sup>[3]</sup>

The ER ( $\dot{m}$ ) is defined as the rate at which the mass of water is converted into vapor per unit area. It is measured by the slope of the mass loss curve obtained with linear fitting in the steady state. Generally, the projected area is used for the ER and evaporation efficiency calculations. Therefore, the ER  $\dot{m}$  is calculated using the equation (2.3):

$$\dot{m} = \frac{dm}{dt} \quad (2.3)$$

where  $m$  is the total mass of the evaporated water and  $t$  is the time.

From equation (2.1), it is evident that the evaporation efficiency of an ISSG system mainly depends on the  $\dot{m}$ , and the other parameters are usually constant. Hence discussing the strategy to improve the ER is the same as enhancing the evaporation efficiency in other ways. In the actual experiment, the whole setup of the evaporator is placed on an analytical balance to record the mass changes of the water during evaporation in real time to evaluate the ER of an ISSG. The light is illuminated from a solar simulator or a xenon lamp with AM 1.5 optical filter, and the intensity is measured with the help of a power meter. An infrared camera or a thermocouple records the evaporation surface temperature and its distribution. The humidity and the temperature of the surroundings are maintained at fixed values throughout the experiment.

### **2.3. Strategies to enhance evaporation efficiency/rate**

Many efforts have been invested in increasing the efficiency of ISSG using different approaches, which are classified mainly into three following approaches: i) finding suitable photothermal materials with high solar light absorption capability with superior light-to-heat

conversion efficiency, ii) effective heat management, iii) controlling the water supply to the system. The following sections provide a detailed discussion of the above-discussed strategies.

### 2.3.1. Photothermal materials

The photothermal material is used to absorb solar light over the whole solar spectrum and then convert the absorbed light into heat. Hence, selecting a photothermal material is crucial in enhancing the overall evaporation efficiency. The ability of a material to absorb solar light is evaluated by its solar absorptance ( $\alpha$ ), defined as the ratio of total absorbed radiation energy to the whole incoming light. The total solar absorptance  $\alpha(\theta)$  of a material at a given incident angle  $\theta$  is obtained by weighting the average of the material's spectral absorptance with the solar spectral irradiance of the standard spectrum (AM 1.5). The  $\alpha(\theta)$  is described using the equation (2.4)<sup>[4]</sup>

$$\alpha(\theta) = \frac{\int_{300}^{2500} [1-R(\theta,\lambda)] I(\theta,\lambda) d\lambda}{\int_{300}^{2500} I(\lambda) d\lambda} \quad (2.4)$$

where  $I(\theta,\lambda)$  and  $R(\theta,\lambda)$  are the light intensity function of the solar spectrum and the reflectivity function of the sample at wavelength  $\lambda$ , respectively.

In the last few years, many photothermal materials, like plasmonic metals,<sup>[5-7]</sup> carbon-based materials,<sup>[8,9]</sup> semiconductors,<sup>[10-12]</sup> and polymers and their hybrids,<sup>[13-15]</sup> have been extensively investigated. The sunlight-to-heat conversion of these photothermal materials occurs via one of the three mechanisms: i) plasmonic localized heating, ii) electron-hole generation and relaxation, and iii) thermal vibration of molecules. The materials like hybrid photothermal compounds may involve more than one mechanism. The plasmon resonance effect is exhibited in the metal NPs.<sup>[16]</sup> The plasmon effect occurs when the frequency of the photon matches the natural frequency of the surface electrons resulting in the coherent oscillation of electrons.<sup>[17]</sup> On light illumination, the electrons excite from occupied states to unoccupied states forming hot electrons,<sup>[18]</sup> which then decay through electron-electron scattering and redistributing the hot electron energy, increasing the localized surface temperature of the material. Au and Ag are the most commonly used plasmonic metals for photothermal applications,<sup>[7,19,20]</sup> and other metals such as Al, Cu, Co, Ni, Mo, and Pt have also been adopted recently.<sup>[21-26]</sup>

When light with similar or higher energy than the band gap falls on the semiconducting material, the electron-hole pairs are generated. For narrow bandgap semiconductors, most of the incident photons have energy higher than that of the bandgap, leading to the generation of the above bandgap electron-hole pairs, and when the electron-hole pairs recombine near the

bandgap edge, energy is released in the form of heat through the thermalization process.<sup>[27][28]</sup> As light absorption depends mainly on the band gap of a semiconductor, it can be enhanced by manipulating the energy band gap of the material. For example, the light absorption of TiO<sub>2</sub> of band gap 3.2 eV, responding only to the UV region, has been extended by narrowing its band gap. Ti<sub>2</sub>O<sub>3</sub> and Mg-reduced TiO<sub>x</sub> have been developed to absorb light with wavelengths ranging from 300 to 2500 nm, thanks to their small band gaps.<sup>[29][30]</sup> In addition, a series of other narrow-bandgap semiconductors have been validated as effective photothermal materials, including MoO<sub>3-x</sub>,<sup>[31]</sup> CuFeSe<sub>2</sub>,<sup>[10]</sup> Fe<sub>3</sub>O<sub>4</sub>,<sup>[32][33]</sup> MnFe<sub>2</sub>O<sub>4</sub>,<sup>[33]</sup> ZnFe<sub>2</sub>O<sub>4</sub>,<sup>[33]</sup> Cu<sub>12</sub>Sb<sub>4</sub>S<sub>13</sub>,<sup>[34]</sup> HCuPO,<sup>[35]</sup> (Cu<sub>2</sub>SnSe<sub>3</sub>, Cu<sub>2</sub>ZnSnSe<sub>4</sub>),<sup>[36]</sup> CoFe<sub>2</sub>O<sub>4</sub>,<sup>[33]</sup> BiInSe<sub>3</sub>,<sup>[37]</sup> SnSe,<sup>[38]</sup> Al–Ti–O,<sup>[39]</sup> NiO,<sup>[40]</sup> *etc.*

In the case of carbon materials and some polymers, heat is produced due to the lattice vibrations upon light absorption.<sup>[41]</sup> With a small amount of energy, the loosely held electrons easily excite from  $\pi$  orbital to  $\pi^*$  orbital. The excited electrons move from the lower energy state (highest occupied molecular orbital, HOMO) to the higher energy state (lowest unoccupied molecular orbital, LUMO), and when the electrons deexcite to the ground state, the energy is released in the form of thermal energy.<sup>[16]</sup> Different carbon-based photothermal materials with superior light absorption coefficients were reported for interfacial water evaporation, such as carbon black,<sup>[42]</sup> graphene,<sup>[43]</sup> graphene oxide (GO),<sup>[44]</sup> reduced graphene oxide (rGO), carbon nanotubes (CNTs),<sup>[45]</sup> carbon fabric,<sup>[46]</sup> foams.<sup>[47]</sup> In addition, some natural plant species like bamboo,<sup>[48]</sup> corncob,<sup>[49]</sup> corn-stalk,<sup>[50]</sup> carrot,<sup>[51]</sup> fruit residues,<sup>[52]</sup> green algae,<sup>[53]</sup> loofah,<sup>[54]</sup> magnolia fruit,<sup>[55]</sup> mushroom,<sup>[51]</sup> lotus leaf and seedpods,<sup>[56,57]</sup> sugarcane,<sup>[58]</sup> sunflower head,<sup>[59]</sup> tofu,<sup>[60]</sup> and wood pieces<sup>[44,61–63]</sup> have been used as photothermal materials in ISSG, to make it cost-effective.

In addition to a single photothermal material, materials' hybridization has been used to enhance absorption and photothermal properties. For instance, Wang *et al.* reported a membrane of nanocomposite of rGO and multi-walled carbon nanotubes (MWCNTs) with surface temperatures 10 °C and 5 °C greater than that of pristine rGO and MWCNTs membranes, respectively.<sup>[64]</sup> Similarly, Liu's group reported the composite of plasmonic Au and carbon-based material with an efficiency of 33.84%, which is 73.8 and 405% higher than the pure carbon spheres and Au NPs, respectively.<sup>[65]</sup> Therefore, the synergistic effect of Au NPs and carbon spheres leads to enhanced optical absorptions, electron-phonon interactions, and thermal conductances at the interfaces.

It is important to note that the choice of substrate material on which the solar absorbers are coated also plays an appealing role in enhancing the evaporation performance of an ISSG

system. For example, Zhu *et al.* prepared an ISSG system by decorating the metal NPs into the 3D mesoporous matrix of the natural wood substrate.<sup>[7]</sup> In this case, the wood substrate acts as an efficient light-trapping media due to the waveguide effect of the microchannels and shows a light absorption of 99% over the whole range of the solar spectrum. Another way of selecting the substrate material is to choose the suitable refractive index. When light travels from one medium of refractive index  $n_1$  to the other medium of refractive index  $n_2$ , the associated reflectivity ( $R$ ) at the interface is calculated by the Fresnel equation:

$$R = \left( \frac{n_1 - n_2}{n_1 + n_2} \right)^2 \quad (2.5)$$

Therefore, choosing the refractive index of the substrate material in between the refractive indices of the two media will ultimately reduce the reflection loss. Taking this into account, Wang's group used nylon with a refractive index of 1.53 as a substrate material which was able to absorb over 94% of solar light in a wet state.<sup>[66]</sup> Similarly, a quartz glass with a refractive index (1.46) close to that of water (1.33) was used as a substrate for  $\text{CuCr}_2\text{O}_4$  NPs, showing excellent black properties in the wet state and hence high ER of  $1.319 \text{ kg m}^{-2} \text{ h}^{-1}$  under 1 sun illumination.<sup>[67]</sup>

### 2.3.2. Thermal management

In the ISSG system, the heat produced by the photothermal material should ideally be utilized for vapor generation. But some part of the generated heat is dissipated in the following ways: i) optical loss (including reflection loss) and thermal losses (including conduction, radiation, and convection heat loss). The total solar energy ( $q_{total}$ ) is calculated by the equation (2.6) [68][69]

$$q_{total} = q_{evap} + q_{ref} + q_{cond} + q_{conv} + q_{rad} \quad (2.6)$$

where  $q_{evap}$ ,  $q_{ref}$ ,  $q_{cond}$ ,  $q_{conv}$ , and  $q_{rad}$  are phase-change enthalpy, reflection loss, conduction losses, convection loss, and radiation loss, respectively. On light illumination on the absorber surface of an evaporator, reflection, and transmission are always associated with light absorption. Since most evaporator surfaces are opaque, in general, the transmission loss is neglected.

The conduction heat loss occurs when the evaporator is directly placed on the water surface. A part of the heat produced by the photothermal material transfer downwards and increases the temperature of the bulk water, which doesn't contribute to the steam generation. The conduction heat loss  $q_{cond}$  to the water underneath, given by Fourier's law:

$$q_{cond} = C_s \times m_b \times \Delta T_b \quad (2.7)$$

where  $m_b$  is the mass of bulk water and  $\Delta T_b$  is the rise in temperature of bulk water.

All the other thermal loss mechanisms depend on the temperature difference between the absorber surface and the surrounding environment. In a conventional ISSG system, the temperature of the photothermal layer is higher than the surrounding, leading to heat losses to the surroundings through radiation and convection. The radiation loss  $q_{rad}$  is calculated by Stefan-Boltzmann equation

$$q_{rad} = \sigma \times \varepsilon \times S_e \times (T_{pt}^4 - T_{amb}^4) \quad (2.8)$$

where  $\sigma$  is the Stefan Boltzmann constant,  $\varepsilon$  is the emissivity of the photothermal layer,  $S_e$  is the evaporation area of the solar absorbing surface,  $T_{pt}$  is the average temperature of the photothermal layer, and  $T_{amb}$  represents the ambient temperature.

The convection heat loss, which occurs due to the flow of fluid, also contributes significantly to the total heat losses associated with the ISSG system. The convection heat loss to the environment is given by Newton's law of cooling and is calculated by the equation (2.9)

$$q_{conv} = h \times S_e \times (T_{pt} - T_{amb}) \quad (2.9)$$

where  $h$  denotes the convective heat transfer coefficient of the SSG system.

Although the heat is localized at the interface in the ISSG system, there is still about 7%, 5%, and 43% radiation loss, convection loss, and conduction loss, respectively, associated if the absorber is in direct contact with bulk water without any thermal management design.<sup>[70]</sup> Therefore, the thermal management of solar evaporators becomes necessary to reduce the above heat losses. In this regard, intense efforts have been invested to suppress these thermal losses using advanced materials and/or device designs, which are discussed in the following sections.

### **2.3.2.1. Suppressing the thermal loss to the underlying water**

The heat dissipation to the underlying bulk water is a major loss among the various heat loss mechanisms. When the solar absorber is in direct contact with the bulk water, a significant portion of the heat transfers downwards to increase the temperature of the bulk water, which has no direct contribution to evaporation. Researchers use both intrinsic and extrinsic management strategies to suppress the downward thermal loss. In the intrinsic case, the thermal conductivity of the absorber is reduced via microstructural designs using microporous structures. To localize the heat generated by the solar absorber, Ghasemi *et al.* demonstrated for the first time a double-layer structure consisting of a carbon foam layer acting as a thermal insulator supporting an absorber layer of exfoliated graphite.<sup>[2]</sup> By using the thermal insulation

layer to minimize the direct contact between the absorber and the bulk water, they attained the solar-to-vapor efficiency of 85% under 10 sun of solar intensity. Similarly, other microporous absorbers such as nanofibre aerogel,<sup>[71]</sup> wood,<sup>[63]</sup> hydrogel,<sup>[72]</sup> and rGO/nanocellulose<sup>[45]</sup> with low thermal conductivities have been employed in ISSG. For such designs, the water transports from the bulk to the top evaporator surface through the interconnected pores of the microporous material. During transportation, the water in the micropores of the material degrades its thermal insulation property.<sup>[73]</sup> Therefore, an optimization of the microporosity is adopted to balance the adequate water supply while keeping the maximum thermal insulation property. In the extrinsic case, the heat loss to the bulk water is reduced by using a thermal insulator as a separator between the solar absorber and the bulk water. Zhu's group demonstrated a floating, thermally insulating, and hydrophobic polystyrene foam-based ISSG with GO as a solar absorber material.<sup>[74]</sup> The solar-to-vapor efficiency of 78% was achieved at 1 sun of solar intensity, and the calculated conduction energy loss was only 5% of the total input solar energy.

### 2.3.2.2. Reducing the reflection loss

Controlling the reflection losses of incident light is another promising strategy to boost overall efficiency. Generally, when the light is incident on a conventional 2D solar absorber, some part reflects into the surrounding atmosphere and thus cannot be utilized for evaporation purposes (Figure 2.2a). Therefore, reducing or reusing the reflected part can improve solar utilization efficiency and the ER. In this direction, researchers found that selecting a suitable 3D evaporator to minimize the reflection heat loss by multiple reflections (Figure 2.2b). For

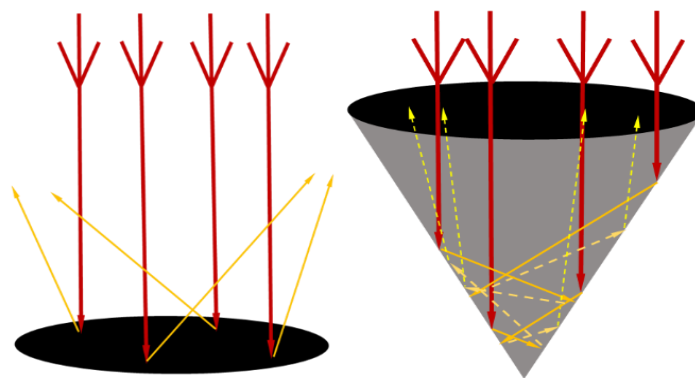


**Figure 2.2.** Schematic diagram of (a) 2D plane and (b) 3D conical structure of ISSG device showing the management of reflection loss in 3D.

example, an artificial cone-structured ISSG system fabricated by coating polypyrrole (PPy) on a polyvinylidene fluoride (PVDF) membrane with a tuneable apex angle was reported to achieve enhanced solar evaporation.<sup>[75]</sup> With the decrease in the apex angle, the diffused

reflectance of the cone increases due to the increase in the times of reflection. Subsequently, Wang and coworkers introduced a cup-shaped photothermal structure with mixed metal oxides as the absorbing layer, which shows an evaporation efficiency close to 100% under 1 sun illumination.<sup>[4]</sup> The high efficiency was attributed to recovering the diffused reflection loss by the walls of the cup. Similarly, Hong *et al.* reported a deployable 3D origami-based ISSG device, which was able to utilize nearly the whole incident energy.<sup>[76]</sup> All these results indicate that the 3D designs of the evaporator have enormous potential to minimize the reflection losses and enhance the light-to-heat conversion efficiency.

### **2.3.2.3. Suppressing thermal loss to the surroundings**

The heat loss to the ambient is another major energy loss generally associated with ISSG systems with high surface temperatures. When the temperature of the evaporator is relatively higher than that of the adjacent surroundings, the heat flows to the surroundings through radiation and convection mechanisms, as discussed earlier. One way to suppress heat loss to the environment is to reduce the surface temperature of the evaporator. Selective solar absorbers (SSA) possessing efficient light absorption and low thermal emission have been exploited recently. For example, Ni *et al.*, for the first time, used a commercial spectrally selective absorber with light absorbance of 93% and emissivity of 7%, for the radiation loss suppression and were able to reduce the radiation loss by about one order of magnitude.<sup>[77]</sup> Another approach people adopted is to increase the effective area of the evaporator. The surface temperature reduces when a high amount of steam escaping from the surface takes away the phase change enthalpy. Based on this strategy, the carbonized mushroom was used to achieve an ER of  $1.475 \text{ kg m}^{-2} \text{ h}^{-1}$ .<sup>[78]</sup> The increased evaporation area of the mushroom decreases the surface temperature of the evaporator and hence reduces the radiation loss. Similarly, a 3D umbrella-like artificial transpiration device with 85% of conversion efficiency was proposed by Li *et al.*,<sup>[70]</sup> which has the lowest surface temperature of 32.7 °C, leading to only 8% energy wastage via convection and radiation loss without any thermal insulation.

### **2.3.3. Absorbing thermal energy from the environment**

A new concept of energy harvesting from the environment has been adopted to increase evaporation efficiency. Theoretically, for 2D ISSG, the ER can go up to  $1.47 \text{ kg m}^{-2} \text{ h}^{-1}$ , corresponding to 100% of efficiency.<sup>[79]</sup> There are many studies in which the reported ER is higher than the theoretical limit because of the 3D designs.<sup>[80][4][81]</sup> The energy can be gained from the environment using some structural designs of the ISSG system. In these designs, the

temperature of the side surface of the evaporator is lower than the surrounding temperature leading to the harvesting of extra energy from the environment via radiative and convective mechanisms. This extra energy enhances the ER and thus exceeds the evaporation efficiency by over 100%. Zhu's group in 2018 reported a cylinder-shaped ISSG system made of nanoparticle-coated cellulose with a low projected area that was able to minimize the energy losses from the top surface and maximize the energy gain from the environment from the side surfaces and achieved an evaporation efficiency over 100%.<sup>[82]</sup> Similarly, Shi *et al.* designed a 3D cup-structured ISSG system with an ER of  $2.04 \text{ kg m}^{-2} \text{ h}^{-1}$  under 1 sun illumination and achieved an energy efficiency of close to 100%.<sup>[4]</sup> In addition to the energy gain from the surrounding air, Xu's group developed a structure that reverses the conduction heat loss by introducing a cold evaporation surface between the evaporating surface and the bulk water.<sup>[83]</sup> The design was able to extract the heat energy from both environment and the bulk water, achieving an ER of  $2.95 \text{ kg m}^{-2} \text{ h}^{-1}$  and energy efficiency beyond the theoretical limit. The same group eventually reported an ISSG system with energy efficiency far exceeding the theoretical limit by completely eliminating the energy losses to the environment.<sup>[83]</sup> They used a heat sink below room temperature to capture heat from the atmosphere, which caused the energy efficiency to cross the theoretical limit.

### 2.3.4. Controlling the water transport

In ISSG, the water is continuously transported from the bulk to the absorber layer through capillary action to maintain uninterrupted evaporation under illumination. Maintaining an adequate water supply using well-designed water transporting channels is another important aspect of enhancing evaporation performance. For strong capillary force, the device sends more water than the ER, which leads to the wastage of heat energy and hinders the vapors from escaping. On the other hand, a slow water flow compared to the ER will increase the temperature of the evaporation layer, leading to heat loss to the environment. Various efforts have been invested in controlling the water content of the device through which not only the energy loss was reduced but also facilitated the steam outflow and hence significantly enhanced the evaporation performance. Based on the design, the water pathways are classified into three categories: 3D, 2D, and 1D. <sup>[73][84]</sup> In 3D, an interconnected porous material in direct contact with the underlying water pumps water to the absorber layer. Various porous materials such as hydrogels,<sup>[72,85]</sup> aerogels,<sup>[85,86]</sup> wood,<sup>[44,63]</sup> sponges,<sup>[87,88]</sup> and cotton,<sup>[69]</sup> have been used to transport water. In 3D water pathways, during water transport, the water in the open pores causes the thermal conductivity to increase, which leads to conduction heat loss to the bulk

water. Zhu's group reported a 2D water pathway by simply wrapping hydrophilic cellulose on a cylinder-shaped foam<sup>[74]</sup>, which simultaneously reduced heat loss along with an efficient water supply and provided a solar-to-vapor efficiency of 80%. The same group reported a 1D water pathway structure made of a cotton rod connected with an umbrella-like absorber without any thermal insulation.<sup>[70]</sup> It effectively reduced the associated heat losses, thus enabling them to achieve 85% energy efficiency.

### **2.3.5. Reducing the vaporization enthalpy**

Reducing the latent heat of vaporization is also an excellent strategy to enhance the ER. Reducing the latent heat of vaporization lowers the energy required to evaporate water.<sup>[89][90]</sup> Zhao *et al.* reported a hydrogel-based ISSG device and achieved an ER of  $3.2 \text{ kg m}^{-2} \text{ h}^{-1}$  under 1 sun illumination.<sup>[91]</sup> The higher ER than the theoretical limit was attributed to the reduction of the latent heat of water present in the nanostructured molecular meshes of the hydrogel. The authors claimed that the latent heat was reduced to 40% of the value of the bulk water. Hydrogels are formed by the cross-linking of the polymer chains. The water in the hydrated hydrogels exists in three forms; bound, intermediate, and free water, as shown in Figure 2.3.<sup>[90]</sup> The water captured by the polar functional groups on hydrophilic polymer chains through

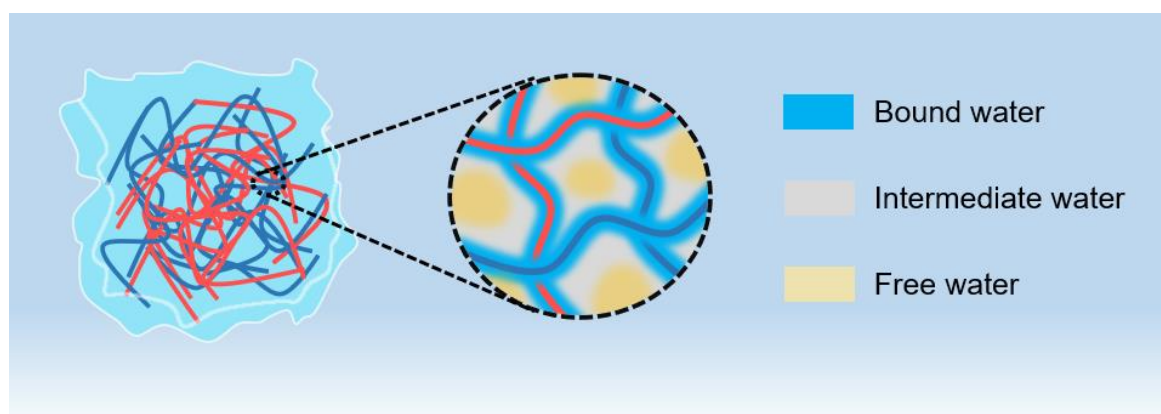


**Figure 2.3.** Schematic illustration of ISSG based on hydrogel showing three different water types—bound, intermediate, and free water.

strong interactions is termed bound water. The water away from the polymer chains with identical properties, like bulk water, is termed free water.<sup>[92]</sup> In free water, the molecule interacts with the four adjacent water molecules with hydrogen bonding, making it highly stable with high vaporization enthalpy. The water molecules, which are bound with less than four water molecules and weakly bound with the polymer chains, form the intermediate water. Intermediate water requires less energy to vaporize than bulk water because fewer hydrogen

bonds have to be broken to separate it from bulk water.<sup>[89]</sup> Therefore, intermediate water evaporates faster in the form of clusters resulting in enhanced efficiency.

## 2.4. Salt mitigation from the absorber surface

During the desalination process using ISSG, the salt crystals accumulate on the absorber surface, creating two serious problems: i) restricting the incident light from reaching the absorber material and ii) blocking the water supply path.<sup>[93]</sup> These eventually reduce the overall evaporation performance and the lifetime of the device. Hence, the salt-fouling issue is another major bottleneck for the development of ISSG. Efforts have been carried out to eliminate this issue by adopting different strategies and achieving salt-resistant properties. These strategies are broadly classified into four categories: i) mechanical washing, ii) diffusion of salt ions back to the bulk water, iii) site-specific salt discharge, and iv) preventing salt ions from directly contacting the absorber surface. The following sections discuss these strategies one by one.<sup>[94]</sup>

### 2.4.1. Mechanical washing

The periodic mechanical cleaning of the salts deposited on the absorbing surface during evaporation is the most appealing way to address the salt-blocking problem in ISSG. In this method, the solar absorbing layer must be strong enough to withstand the periodic brushing or sonication. This method is, therefore, effective as long as the structure of the evaporator has good mechanical strength and is particularly suitable for flexible and elastic membrane evaporators. For example, Ren *et al.* designed a hierarchical foam<sup>[95]</sup> of graphene with evaporation efficiency > 90% in seawater desalination. After long-term operations under high light intensity, the salt precipitated on the absorber surface was removed by directly washing the material several times or dip-rinsing. Similarly, Jin *et al.* demonstrated a highly stable,<sup>[66]</sup> flexible nonwoven photothermal cloth composed of nylon nanofibers with the encapsulation of carbon black NPs. The salt deposited during desalination on the surface was easily removed as soon as the salt affected the light absorption by mild handwashing. After washing, the device maintains its initial ER. In a similar way, Zhu's group reported for the first time a carbonized tofu with the advantages of low cost, high durability, and long-lasting.<sup>[60]</sup> They achieved the maximum ER of  $1.65 \text{ kg m}^{-2} \text{ h}^{-1}$  with a conversion efficiency of 87.26% under 1 sun illumination. The salt accumulated on the absorber surface during desalination was removed directly by soaking the evaporator in the water.

### **2.4.2. Diffusion of salt ions back into the bulk water/self-cleaning**

Natural dissolution of salt crystals in the bulk water, or in other words, self-cleaning, is another feasible alternative solution to the problem of salt accumulation. The salt crystals precipitate on the evaporator surface automatically dissolve during the night through the interdiffusion of salt under a low ER. The salt dissolution mainly depends upon the porosity and the hydrophilicity of the material, i.e., the self-cleaning of salt will be faster for highly porous and hydrophilic material. The naturally occurring wood possesses a porous structure and hydrophilic properties, making it a promising candidate for self-cleaning material. Hu's group developed a plasmonic wood by decorating the metal NPs on the matrix of natural wood.<sup>[7]</sup> The plasmonic wood with high light absorption (~99%), high porosity, and low tortuosity achieved the ER of  $11.8 \text{ kg m}^{-2} \text{ h}^{-1}$  under 10 sun illumination. Under 5 sun illumination, the saline water evaporates from the surface and leaves behind salt crystals. The formed salt crystals gradually dissolved back into the saline bulk water when the light was turned off (night-time). The water transport remained constant for 8 h of continuous operation due to the large diameter of the microchannels of the plasmonic wood, which otherwise get blocked by salt crystallization in the low-diameter microchannel. These properties enable the plasmonic wood-based ISSG device to show excellent cycling performance for a continuous 144 h without degradation. Furthermore, Kaung *et al.*<sup>[96]</sup> reported a self-regenerating ISSG system having excellent antifouling properties by drilling small channels within a wood substrate and achieved long-term stability for over 100 h of continuous operation and attained the highest efficiency of around 75% in 20 wt% of NaCl solution under 1 sun illumination. Recently, another strategy of self-cleaning via self-rotation was adopted by Zhu's<sup>[97]</sup> and Xu's<sup>[97]</sup> group, in which they developed a floatable spherical ISSG system of density lower than the seawater with a hydrophilic surface. Under continuous light illumination, the evaporation of seawater leads to the accumulation of salt crystals on the top surface of the sphere, which eventually induces a rotation of the sphere. The rotation of the sphere causes the salt-accumulated portions to turn downwards for self-cleaning and some other portions to turn upwards for evaporation.

### **2.4.3. Direct water resistance and salt ion repulsion**

Generally, the ISSG system consists of a hydrophilic absorber layer, which tends to get degraded by salt accumulation during evaporation. Replacing the hydrophilic layer with a hydrophobic surface of a non-wetting feature is a practical approach for preventing salt accumulation. In this approach, people use the Janus-type structures in which the solar

absorbing and the water pumping layers are decoupled on each side with a hydrophilic bottom layer for water supply and a hydrophobic top layer for light absorption. In 2018, Zhu *et al.*<sup>[98]</sup> proposed a double-layered hydrophilic/hydrophobic structure with a bottom hydrophilic layer made of polyacrylonitrile for water transport submerged into water and a top hydrophobic layer made of carbon black-coated polymethyl methacrylate for light absorption. This design allows only the bottom layer to accumulate salt but avoids the salt accumulation on the absorber surface, providing a better way to tackle the problem of salt accumulation when dealing with high-salinity brine. Generally, 3D solar evaporators have high ER than 2D evaporators and hence have a higher salt crystallization rate. Therefore, it is difficult for 3D evaporators to operate continuously for a long time without salt crystallization on the absorber surface. Recently Yu *et al.* proposed a conical Janus evaporator with a hydrophilic cylinder of cotton mesh to provide a path for salt discharge from the high salt area to the underlying water.<sup>[99]</sup> This design achieved a continuous ER of  $2.8 \text{ kg m}^{-2} \text{ h}^{-1}$  under 1 sun of light intensity without the salt precipitation on the evaporation surface. The ER was maintained for continuous operation of 400 h in the salinity of 20 wt% NaCl solution. The hydrophobic layer loses its property for long-term operation due to some photochemical oxidation under highly intense light illumination. Yin's group provides a solution to this problem by coating the hydrophobic layer of polydimethylsiloxane to prevent the hydrophobic layer from photochemical oxidation.<sup>[100]</sup> The evaporator demonstrated an excellent salt rejection capability and showed an ER of  $1.38 \text{ kg m}^{-2} \text{ h}^{-1}$  for 400 min of continuous operation or 90 days of intermittent work. Another approach to avoid salt accumulation on the absorber surface is contactless ISSG. In this type of design, the ISSG is not in direct contact with the bulk water; instead, the structure absorbs the incident solar radiation and then re-radiates in the infrared range, which is absorbed by the upper layer within the penetration depth of sub-200  $\mu\text{m}$  of the water and converts into steam.<sup>[101]</sup>

#### **2.4.4. Site-specific salt discharge**

So far, in all the cases, the salt is discharged into the bulk water instead of being completely separated. Hence using such solar desalination techniques on a large scale will have a severe problem with aquatic life and some other environmental impacts. Isolating the salt after crystallization during evaporation not only resolves the ecological issues but also allows the harvesting of salt and other minerals simultaneously with freshwater production. Recently, efforts have been reported for simultaneous salt production in ISSG using proper structural management. For example, Xia *et al.* followed site-specific salt discharge in which the water

is pushed to some specific sites using capillary forces.<sup>[102]</sup> They reported a 2D structure of CNT coated on super-hydrophilic filter paper in which the water was supplied using cotton thread inserted at the center of the evaporation disc. During evaporation from the absorbing surface, the salt tends to approach the edges, resulting in salt crystallization at the edges of the evaporation disc. Finally, the crystallized salts at the edges automatically fell off under gravity by weakening the binding force between salt crystals and the evaporator. The device shows simultaneous evaporation and salt harvesting for continuous operation of 600 h without stopping the light illumination. A similar approach was used for a 3D cup-shaped ISSG system where the single-directional flow moves salt to the walls of the cup and keeps the bottom part free from salt, resulting in the evaporator maintaining a stable ER.<sup>[103]</sup> Recently, Wu *et al.* reported a bio-mimetic 3D cone-shaped design with gradient distribution interfacial water film using its microporous structure.<sup>[104]</sup> During the evaporation of 25 wt% NaCl solution, the salt crystallizes on the cone's apex, which was collected simply by tilting the evaporator.

## **2.5. Condensation of the generated steam**

The last and most crucial step in ISSG is water collection through vapor condensation. Most related studies have focussed on enhancing energy efficiency and the ER only under an open atmosphere by designing highly efficient photothermal materials. The inefficient condensation of the generated steam in a single-stage ISSG device limits the CR of purified water. In general, there is a large discrepancy between the ER and the CR<sup>[91,105–107]</sup>, which arises from the fact that during evaporation, the steam mist condensed on the inner surface of the transparent cover of the ISSG blocks around 35% of the incident light. Also, in the closed system, the internal humidity is increased, which reduces the steam generation rate. Therefore, some strategies have been reported for efficient water CRs by developing novel designs. For instance, the CR was enhanced using different types of condenser materials of high solar transmittance, such as glass and plastic materials.<sup>[108,109]</sup> Mudde and coworkers<sup>[110]</sup> compared the two solar stills, one with glass and the other with polyethylene terephthalate (PET) as the condenser material. After the vapor condensation, the PET surface was shinier than the glass surface leading to energy loss and also blocking the incident light. Therefore, the solar still with glass as the condenser has a 30% enhanced CR. Another major limitation with these types of solar stills is the low-temperature difference between the condense and the inner steam, which results in a reduced overall CR. Some studies have shown that by cooling the condenser, water productivity can be enhanced significantly.<sup>[109]</sup> When the condenser temperature (glass cover) was decreased by

increasing air mass circulation in the range of 6-20 °C, the productivity was enhanced by 20%.<sup>[111]</sup> Another reliable approach to improve the CR is by enlarging the condensation area. The same group<sup>[112]</sup> also reported that by increasing the condensation area by 7.5 times, the freshwater production was increased by more than 65% under simulated solar light of the intensity of 652 W m<sup>-2</sup>. They also demonstrate the effect of cooling by attaining the enhancement of more than eight times by decreasing the condenser temperature to 0 °C.

As discussed above, in a closed system, the humidity increases, which leads to a decrease in the ER and, finally, the CR. In closed systems, the condensation rate controls the ER as it increases the vapor pressure. Therefore, to improve the condensation rate, it is necessary to decrease the internal humidity of the system. Zhang *et al.* integrated a solar-powered electric fan inside the condensation chamber to reduce the chamber's relative humidity.<sup>[113]</sup> Using such a design, they achieved a 15 times higher CR (0.15 kg m<sup>-2</sup> h<sup>-1</sup>) than natural evaporation. Guo *et al.* also used the same airflow strategy inside the chamber and achieved a CR of 1.3, 2.2, and 3 kg m<sup>-2</sup> h<sup>-1</sup> at the airflow speed of 0, 10, and 40 ml min<sup>-1</sup>, respectively, under 1 sun illumination.<sup>[72]</sup> Similarly, Li *et al.* reduced the humidity by reducing the pressure of the chamber using a hand-operated vacuum pump and reported an ER and CR of 1.72, 2.25 kg m<sup>-2</sup> h<sup>-1</sup> and 1.52, 2.11 kg m<sup>-2</sup> h<sup>-1</sup> at the pressure of 1, 0.17 atm respectively.<sup>[114]</sup>

The recovery of the latent heat produced during condensation and its utilization is a promising route to enhance the CR of ISSG significantly. Chia-vazzo *et al.* designed a multistage distiller to recover the latent heat and improve the freshwater CR.<sup>[115]</sup> Each stage comprises two hydrophilic layers (one for steam generation and the other for condensation) and an intermediate hydrophobic layer. The subsequent stage uses the latent heat of the condensed vapors in the preceding stage for evaporation. With this design, they achieved the highest CR of 3 L m<sup>-2</sup> h<sup>-1</sup> under the solar intensity of 1 sun for a 10-stage configuration device. Using almost the same design, Xu and coworkers efficiently recycle and reutilize the latent heat by adjusting the structural parameters.<sup>[116]</sup> The solar-to-vapor conversion efficiency increased from 81 % to 385 % when the number of stages increased from 1 to 10, and the CR increased from 1.21 to 5.78 L m<sup>-2</sup> h<sup>-1</sup>.

## 2.6. Applications of ISSG

Although ISSG has primarily been investigated for freshwater production, the rapid advancement of this technology has led to some additional applications. For example, desalination, sterilization, photocatalysis, wastewater purification, and energy generation have

been reported recently.<sup>[117][108][118]</sup> The following section contains a detailed discussion of the additional advantages of ISSG systems.

### **2.6.1. Desalination**

ISSG has recently been considered a better alternative for seawater desalination than existing technologies like reverse osmosis and distillation. Although reverse osmosis produces freshwater from seawater by removing around 99% of salt ions, the high energy consumption and the associated pollution hinder its further promotion. In ISSG, a condensing unit is used to collect the evaporated water from either the real seawater or simulated seawater, followed by detecting the concentrations of four primary ions  $\text{Na}^+$ ,  $\text{K}^+$ ,  $\text{Ca}^{2+}$ , and  $\text{Mg}^{2+}$  present in the seawater before and after evaporation. Their concentrations have been found to be far below the drinking water standards set by World Health Organization (WHO) and US Environmental Protection Agency (EPA). Some reports show that under a high concentration of  $100 \text{ mg mL}^{-1}$ , ISSG shows better desalination capacity than conventional technologies by removing up to 99.5% of salt. Hong *et al.*<sup>[76]</sup> desalinated the seawater collected from the Red Sea (Saudi Arabia) and found that after condensation, the concentration of  $\text{Na}^+$ ,  $\text{K}^+$ ,  $\text{Ca}^{2+}$ , and  $\text{Mg}^{2+}$  reduced significantly to 1.41, 0.76, 0.91, and 0.05 mg/L.

In addition to the freshwater production from seawater by removing the salt ions, collecting these precious mineral salts from the seawater has also gained tremendous interest. To this end, Xia *et al.* proposed a disk-shaped ISSG device with a vertical seawater uptake thread, in which the salt crystals fell under gravity because of edge-preferential crystallization.<sup>[102]</sup> The device produced freshwater from 10 wt% of saltwater and harvested salt at the rate of  $0.42 \text{ kg m}^{-2}$  per day. Similarly, Liu and coworkers reported a solar-thermo-radiative evaporator and harvested salt at the rate of  $36.25 \text{ g m}^{-2} \text{ h}^{-1}$  at 1 sun illumination under 3.5 wt% concentration of saltwater.<sup>[119]</sup>

### **2.6.2. Wastewater purification**

The purification of wastewater using ISSG is also an essential requirement for freshwater production. In addition to desalination, ISSG has also been used to remove different pollutants from other types of wastewater, such as heavy metal ions, organic dyes, and bacteria. Li *et al.*<sup>[82]</sup> used wastewater composed of heavy metals concentrations of 0.2, 0.5, and 0.2  $\text{mg L}^{-1}$  for  $\text{Cu}^{2+}$ ,  $\text{Cr}^{3+}$ , and  $\text{Pb}^{2+}$ , and found that reported the concentrations of  $\text{Cu}^{2+}$  ions as 0.066  $\text{mg L}^{-1}$  in the condensed water and the other two ions ( $\text{Cr}^{3+}$ ,  $\text{Pb}^{2+}$ ) were undetected (i.e., concentration  $<0.01 \text{ mg L}^{-1}$ ). Similarly, Lei *et al.*<sup>[120]</sup> tested their ISSG device for the

purification of wastewater containing heavy metal ions ( $\text{Cu}^{2+}$ ,  $\text{Ni}^{2+}$ ,  $\text{Zn}^{2+}$ ,  $\text{Co}^{2+}$ ,  $\text{Cr}^{6+}$ ) and found that after condensation of the steam, the concentration of these ions dropped significantly. Also, Fan and coworkers demonstrated for the first time the removal of  $\text{Hg}^{2+}$  ions using an ISSG system made of synthesized carbon-molybdenum-disulfide ( $\text{MoS}_2/\text{C}$ ) microbeads assembled on a 3D polyurethane sponge.<sup>[121]</sup> During the evaporation process, the sulfur atoms in  $\text{MoS}_2$  adsorb the  $\text{Hg}^{2+}$  ions and reduce their concentration from 200 ppb to 1 ppb, meeting the level set by EPA. The removal of the commonly used organic dyes such as methyl blue (MB), methyl orange (MO), and Rhodamine B is frequently reported in the ISSG technique with a removal efficiency close to 100%. Further, it was observed that the ISSG has excellent potential in purifying the wastewater sample contaminated with bacteria as un membrane technologies; the bacteria need to be removed before purification because the membrane pores get easily blocked, decreasing the purification performance.<sup>[122]</sup>

### 2.6.3. Energy generation

Energy generation simultaneously with steam generation is another exciting application of ISSG technology and has gained tremendous interest as it provides renewable and decentralized freshwater-energy solutions. The energy was generated directly or indirectly from the heat that is otherwise getting wasted through the environment. Different forms of energy were produced synergistically from ISSG systems, including electricity and chemical fuels, such as hydrogen, ethanol, methane, and various hydrocarbon fuels.

The fuels were produced through the process of photocatalysis using photothermal catalytic materials. In this regard, Ho's group reported a photothermal catalytic gel consisting of  $\text{TiO}_2/\text{Ag}$  nanofibers and water absorber chitosan polymer for the simultaneous generation of freshwater and hydrogen.<sup>[123]</sup>  $\text{TiO}_2$  nanofibers act as photoredox materials in the structure, and Ag NPs act as a catalyst and solar absorbers. The device produced hydrogen and freshwater at the rate of  $1.49 \text{ kg m}^{-2} \text{ h}^{-1}$  and  $3260 \mu\text{mol m}^{-2} \text{ h}^{-1}$ , respectively, under 1 sun illumination. Also, Halas and coworkers demonstrated solar-driven ethanol production from cellulosic feedstock.<sup>[124]</sup> In this system, on illumination, the light-absorbing NPs produce steam which is then used to degrade the cellulose chains of the feedstock into sugars. Finally, the obtained glucose is fermented and then distilled to get pure ethanol.

Using some energy harvesters, simultaneous electricity was generated from the waste thermal energy during the evaporation process. For example, Zhu's group introduces a thermoelectric generator (TEG) to recover the latent heat produced by the high-temperature steam during condensation.<sup>[125]</sup> Using such a design, they attained an ER of  $34.8 \text{ kg m}^{-2} \text{ h}^{-1}$

and an output power of 574 mW, enough to power an electric fan directly under the solar intensity of 30 sun. Further, the kinetic energy of the steam was also converted to electricity by Ho's group using a ferroelectric PVDF cantilever and achieved the highest power density of 0.24 mW cm<sup>-2</sup> under 1 sun of light illumination.<sup>[126]</sup> The temperature difference between the underlying water and the solar absorber was also harvested using TEG. The same group used a thermoelectric module to harvest the energy from the temperature gradient and achieved a power density of 0.4 W m<sup>-2</sup>.<sup>[127]</sup> Further, the energy contained in the salinity gradient of the solution between the evaporation interface and the underlying bulk water caused by the evaporation was utilized by Zhou's group through a Nafion membrane and achieved an open-circuit voltage ( $V_{oc}$ ) of 84 mV at a solar intensity of 2 sun.<sup>[128]</sup>

## 2.7. References

- [1] C. Chen, Y. Kuang, L. Hu, *Joule* **2019**, 3, 683.
- [2] H. Ghasemi, G. Ni, A. M. Marconnet, J. Loomis, S. Yerci, N. Miljkovic, G. Chen, *Nat. Commun.* **2014**, 5, 4449.
- [3] J. Zhou, Y. Gu, P. Liu, P. Wang, L. Miao, J. Liu, A. Wei, X. Mu, J. Li, J. Zhu, *Adv. Funct. Mater.* **2019**, 29, 1903255.
- [4] Y. Shi, R. Li, Y. Jin, S. Zhuo, L. Shi, J. Chang, S. Hong, K.-C. Ng, P. Wang, *Joule* **2018**, 2, 1171.
- [5] C. Chen, L. Zhou, J. Yu, Y. Wang, S. Nie, S. Zhu, J. Zhu, *Nano Energy* **2018**, 51, 451.
- [6] F. Tao, Y. Zhang, K. Yin, S. Cao, X. Chang, Y. Lei, D. Wang, R. Fan, L. Dong, Y. Yin, X. Chen, *Sustain. Energy Fuels* **2018**, 2, 2762.
- [7] M. Zhu, Y. Li, F. Chen, X. Zhu, J. Dai, Y. Li, Z. Yang, X. Yan, J. Song, Y. Wang, E. Hitz, W. Luo, M. Lu, B. Yang, L. Hu, *Adv. Energy Mater.* **2018**, 8, 1701028.
- [8] J. Yang, Y. Pang, W. Huang, S. K. Shaw, J. Schiffbauer, M. A. Pillers, X. Mu, S. Luo, T. Zhang, Y. Huang, G. Li, S. Ptasinska, M. Lieberman, T. Luo, *ACS Nano* **2017**, 11, 5510.
- [9] B. Hou, Z. Cui, X. Zhu, X. Liu, G. Wang, J. Wang, T. Mei, J. Li, X. Wang, *Mater. Chem. Phys.* **2019**, 222, 159.
- [10] H. Liu, C. Chen, H. Wen, R. Guo, N. A. Williams, B. Wang, F. Chen, L. Hu, *J. Mater. Chem. A* **2018**, 6, 18839.
- [11] I. Ibrahim, D. H. Seo, A. M. McDonagh, H. K. Shon, L. Tijning, *Desalination* **2021**, 500, 114853.

- [12] M. S. Irshad, X. Wang, M. S. Abbasi, N. Arshad, Z. Chen, Z. Guo, L. Yu, J. Qian, J. You, T. Mei, *ACS Sustain. Chem. Eng.* **2021**, *9*, 3887.
- [13] C. Li, D. Jiang, B. Huo, M. Ding, C. Huang, D. Jia, H. Li, C. Y. Liu, J. Liu, *Nano Energy* **2019**, *60*, 841.
- [14] P. Mu, W. Bai, Z. Zhang, J. He, H. Sun, Z. Zhu, W. Liang, A. Li, *J. Mater. Chem. A* **2018**, *6*, 18183.
- [15] Y. Xu, J. Xu, J. Zhang, X. Li, B. Fu, C. Song, W. Shang, P. Tao, T. Deng, *Nano Energy* **2022**, *93*, 106882.
- [16] L. Zhu, M. Gao, C. K. N. Peh, G. W. Ho, *Nano Energy* **2019**, *57*, 507.
- [17] Z. W. Seh, S. Liu, M. Low, S.-Y. Zhang, Z. Liu, A. Mlayah, M.-Y. Han, *Adv. Mater.* **2012**, *24*, 2310.
- [18] S. Linic, U. Aslam, C. Boerigter, M. Morabito, *Nat. Mater.* **2015**, *14*, 567.
- [19] M. Gao, P. K. N. Connor, G. W. Ho, *Energy Environ. Sci.* **2016**, *9*, 3151.
- [20] L. Zhou, Y. Tan, D. Ji, B. Zhu, P. Zhang, J. Xu, Q. Gan, Z. Yu, J. Zhu, *Sci. Adv.* **2016**, *2*, e1501227.
- [21] L. F. Greenlee, D. F. Lawler, B. D. Freeman, B. Marrot, P. Moulin, *Water Res.* **2009**, *43*, 2317.
- [22] G. P. Narayan, M. H. Sharqawy, E. K. Summers, J. H. Lienhard, S. M. Zubair, M. A. Antar, *Renew. Sustain. Energy Rev.* **2010**, *14*, 1187.
- [23] A. D. Rakić, A. B. Djurišić, J. M. Elazar, M. L. Majewski, *Appl. Opt.* **1998**, *37*, 5271.
- [24] A. Lalis, G. Tessier, J. Plain, G. Baffou, *J. Phys. Chem. C* **2015**, *119*, 25518.
- [25] P. Fan, H. Wu, M. Zhong, H. Zhang, B. Bai, G. Jin, *Nanoscale* **2016**, *8*, 14617.
- [26] L. Zhou, Y. Tan, J. Wang, W. Xu, Y. Yuan, W. Cai, S. Zhu, J. Zhu, *Nat. Photonics* **2016**, *10*, 393.
- [27] G. Kresse, J. Furthmüller, *Phys. Rev. B* **1996**, *54*, 11169.
- [28] M. Umlauff, J. Hoffmann, H. Kalt, W. Langbein, J. M. Hvam, M. Scholl, J. Söllner, M. Heuken, B. Jobst, D. Hommel, *Phys. Rev. B* **1998**, *57*, 1390.
- [29] J. Wang, Y. Li, L. Deng, N. Wei, Y. Weng, S. Dong, D. Qi, J. Qiu, X. Chen, T. Wu, *Adv. Mater.* **2017**, *29*, 1603730.
- [30] M. Ye, J. Jia, Z. Wu, C. Qian, R. Chen, P. G. O'Brien, W. Sun, Y. Dong, G. A. Ozin, *Adv. Energy Mater.* **2017**, *7*, 1601811.
- [31] D. Ding, W. Huang, C. Song, M. Yan, C. Guo, S. Liu, *Chem. Commun.* **2017**, *53*, 6744.
- [32] X. Wang, G. Ou, N. Wang, H. Wu, *ACS Appl. Mater. Interfaces* **2016**, *8*, 9194.

- [33] R. Chen, Z. Wu, T. Zhang, T. Yu, M. Ye, *RSC Adv.* **2017**, *7*, 19849.
- [34] C. Song, T. Li, W. Guo, Y. Gao, C. Yang, Q. Zhang, D. An, W. Huang, M. Yan, C. Guo, *New J. Chem.* **2018**, *42*, 3175.
- [35] Z. Hua, B. Li, L. Li, X. Yin, K. Chen, W. Wang, *J. Phys. Chem. C* **2017**, *121*, 60.
- [36] Y. Yang, H. Zhao, Z. Yin, J. Zhao, X. Yin, N. Li, D. Yin, Y. Li, B. Lei, Y. Du, W. Que, *Mater. Horizons* **2018**, *5*, 1143.
- [37] J. D. Yao, Z. Q. Zheng, G. W. Yang, *Nanoscale* **2017**, *9*, 16396.
- [38] J. Yao, Z. Zheng, G. Yang, *Nanoscale* **2018**, *10*, 2876.
- [39] L. Yi, S. Ci, S. Luo, P. Shao, Y. Hou, Z. Wen, *Nano Energy* **2017**, *41*, 600.
- [40] H. Liu, X. Zhang, Z. Hong, Z. Pu, Q. Yao, J. Shi, G. Yang, B. Mi, B. Yang, X. Liu, H. Jiang, X. Hu, *Nano Energy* **2017**, *42*, 115.
- [41] M. Gao, L. Zhu, C. K. Peh, G. W. Ho, *Energy Environ. Sci.* **2019**, *12*, 841.
- [42] Y. Liu, J. Chen, D. Guo, M. Cao, L. Jiang, *ACS Appl. Mater. Interfaces* **2015**, *7*, 13645.
- [43] P. Zhang, J. Li, L. Lv, Y. Zhao, L. Qu, *ACS Nano* **2017**, *11*, 5087.
- [44] K.-K. Liu, Q. Jiang, S. Tadepalli, R. Raliya, P. Biswas, R. R. Naik, S. Singamaneni, *ACS Appl. Mater. Interfaces* **2017**, *9*, 7675.
- [45] Q. Jiang, L. Tian, K. Liu, S. Tadepalli, R. Raliya, P. Biswas, R. R. Naik, S. Singamaneni, *Adv. Mater.* **2016**, *28*, 9400.
- [46] M. W. Higgins, A. Shakeel RAhmaan, R. R. Devarapalli, M. V. Shelke, N. Jha, *Sol. Energy* **2018**, *159*, 800.
- [47] X. Lin, J. Chen, Z. Yuan, M. Yang, G. Chen, D. Yu, M. Zhang, W. Hong, X. Chen, *J. Mater. Chem. A* **2018**, *6*, 4642.
- [48] Y. Bian, Q. Du, K. Tang, Y. Shen, L. Hao, D. Zhou, X. Wang, Z. Xu, H. Zhang, L. Zhao, S. Zhu, J. Ye, H. Lu, Y. Yang, R. Zhang, Y. Zheng, S. Gu, *Adv. Mater. Technol.* **2019**, *4*, 1800593.
- [49] Y. Sun, Z. Zhao, G. Zhao, L. Wang, D. Jia, Y. Yang, X. Liu, X. Wang, J. Qiu, *Carbon* **2021**, *179*, 337.
- [50] Z. Sun, W. Li, W. Song, L. Zhang, Z. Wang, *J. Mater. Chem. A* **2020**, *8*, 349.
- [51] Y. Long, S. Huang, H. Yi, J. Chen, J. Wu, Q. Liao, H. Liang, H. Cui, S. Ruan, Y.-J. Zeng, *J. Mater. Chem. A* **2019**, *7*, 26911.
- [52] Y. Zhang, S. K. Ravi, S. C. Tan, *Nano Energy* **2019**, *65*, 104006.
- [53] M. Maleki, F. Arabpour Roghabadi, S. M. Sadrameli, *ACS Omega* **2022**, *7*, 39895.
- [54] W. Yao, X. Zhu, Z. Xu, R. A. Davis, G. Liu, H. Zhong, X. Lin, P. Dong, M. Ye, J.

- Shen, *ACS Appl. Mater. Interfaces* **2022**, *14*, 4680.
- [55] Y. Bian, Y. Shen, K. Tang, Q. Du, L. Hao, D. Liu, J. Hao, D. Zhou, X. Wang, H. Zhang, P. Li, Y. Sang, X. Yuan, L. Zhao, J. Ye, B. Liu, H. Lu, Y. Yang, R. Zhang, Y. Zheng, X. Xiong, S. Gu, *Glob. Challenges* **2019**, *3*, 1900040.
- [56] Y. Liao, J. Chen, D. Zhang, X. Wang, B. Yuan, P. Deng, F. Li, H. Zhang, *Mater. Lett.* **2019**, *240*, 92.
- [57] J. Fang, J. Liu, J. Gu, Q. Liu, W. Zhang, H. Su, D. Zhang, *Chem. Mater.* **2018**, *30*, 6217.
- [58] C. Xiao, L. Chen, P. Mu, J. Jia, H. Sun, Z. Zhu, W. Liang, A. Li, *ChemistrySelect* **2019**, *4*, 7891.
- [59] P. Sun, W. Zhang, I. Zada, Y. Zhang, J. Gu, Q. Liu, H. Su, D. Pantelić, B. Jelenković, D. Zhang, *ACS Appl. Mater. Interfaces* **2020**, *12*, 2171.
- [60] X. Zhou, J. Li, C. Liu, F. Wang, H. Chen, C. Zhao, H. Sun, Z. Zhu, *Int. J. Energy Res.* **2020**, *44*, 9213.
- [61] F. He, M. Han, J. Zhang, Z. Wang, X. Wu, Y. Zhou, L. Jiang, S. Peng, Y. Li, *Nano Energy* **2020**, *71*, 104650.
- [62] X. Zhou, W. Zhang, C. Zhang, Y. Tan, J. Guo, Z. Sun, X. Deng, *ACS Appl. Mater. Interfaces* **2020**, *12*, 11232.
- [63] C. Jia, Y. Li, Z. Yang, G. Chen, Y. Yao, F. Jiang, Y. Kuang, G. Pastel, H. Xie, B. Yang, S. Das, L. Hu, *Joule* **2017**, *1*, 588.
- [64] Y. Wang, C. Wang, X. Song, S. K. Megarajan, H. Jiang, *J. Mater. Chem. A* **2018**, *6*, 963.
- [65] Z. Gan, Z. Chen, L. Liu, L. Zhang, W. Tu, Y. Liu, *Sol. RRL* **2017**, *1*, 1600032.
- [66] Y. Jin, J. Chang, Y. Shi, L. Shi, S. Hong, P. Wang, *J. Mater. Chem. A* **2018**, *6*, 7942.
- [67] Y. Shi, R. Li, L. Shi, E. Ahmed, Y. Jin, P. Wang, *Adv. Sustain. Syst.* **2018**, *2*, 1870026.
- [68] C. Tu, W. Cai, X. Chen, X. Ouyang, H. Zhang, Z. Zhang, *Small* **2019**, *15*, 1902070.
- [69] X. Wu, T. Gao, C. Han, J. Xu, G. Owens, H. Xu, *Sci. Bull.* **2019**, *64*, 1625.
- [70] X. Li, R. Lin, G. Ni, N. Xu, X. Hu, B. Zhu, G. Lv, J. Li, S. Zhu, J. Zhu, *Natl. Sci. Rev.* **2018**, *5*, 70.
- [71] F. Jiang, H. Liu, Y. Li, Y. Kuang, X. Xu, C. Chen, H. Huang, C. Jia, X. Zhao, E. Hitz, Y. Zhou, R. Yang, L. Cui, L. Hu, *ACS Appl. Mater. Interfaces* **2018**, *10*, 1104.
- [72] Y. Guo, X. Zhou, F. Zhao, J. Bae, B. Rosenberger, G. Yu, *ACS Nano* **2019**, *13*, 7913.
- [73] L. Zhou, X. Li, G. W. Ni, S. Zhu, J. Zhu, *Natl. Sci. Rev.* **2019**, *6*, 562.
- [74] X. Li, W. Xu, M. Tang, L. Zhou, B. Zhu, S. Zhu, J. Zhu, *Proc. Natl. Acad. Sci.* **2016**,

- 113, 13953.
- [75] Y. Wang, C. Wang, X. Song, M. Huang, S. K. Megarajan, S. F. Shaikat, H. Jiang, *J. Mater. Chem. A* **2018**, *6*, 9874.
- [76] S. Hong, Y. Shi, R. Li, C. Zhang, Y. Jin, P. Wang, *ACS Appl. Mater. Interfaces* **2018**, *10*, 28517.
- [77] G. Ni, G. Li, S. V. Boriskina, H. Li, W. Yang, T. Zhang, G. Chen, *Nat. Energy* **2016**, *1*, 16126.
- [78] N. Xu, X. Hu, W. Xu, X. Li, L. Zhou, S. Zhu, J. Zhu, *Adv. Mater.* **2017**, *29*, 1606762.
- [79] P. Zhang, Q. Liao, H. Yao, Y. Huang, H. Cheng, L. Qu, *Energy Storage Mater.* **2019**, *18*, 429.
- [80] H. Wang, C. Zhang, Z. Zhang, B. Zhou, J. Shen, A. Du, *Adv. Funct. Mater.* **2020**, *30*, 2005513.
- [81] H. Liang, Q. Liao, N. Chen, Y. Liang, G. Lv, P. Zhang, B. Lu, L. Qu, *Angew. Chemie Int. Ed.* **2019**, *58*, 19041.
- [82] X. Li, J. Li, J. Lu, N. Xu, C. Chen, X. Min, B. Zhu, H. Li, L. Zhou, S. Zhu, T. Zhang, J. Zhu, *Joule* **2018**, *2*, 1331.
- [83] Y. Wang, X. Wu, X. Yang, G. Owens, H. Xu, *Nano Energy* **2020**, *78*, 105269.
- [84] P. Tao, G. Ni, C. Song, W. Shang, J. Wu, J. Zhu, G. Chen, T. Deng, *Nat. Energy* **2018**, *3*, 1031.
- [85] M. Tan, J. Wang, W. Song, J. Fang, X. Zhang, *J. Mater. Chem. A* **2019**, *7*, 1244.
- [86] D. D. Qin, Y. J. Zhu, F. F. Chen, R. L. Yang, Z. C. Xiong, *Carbon* **2019**, *150*, 233.
- [87] Q. Yang, C. Xu, F. Wang, Z. Ling, Z. Zhang, X. Fang, *ACS Appl. Energy Mater.* **2019**, *2*, 7223.
- [88] Z. Zhang, P. Mu, J. He, Z. Zhu, H. Sun, H. Wei, W. Liang, A. Li, *ChemSusChem* **2019**, *12*, 426.
- [89] X. Zhou, Y. Guo, F. Zhao, G. Yu, *Acc. Chem. Res.* **2019**, *52*, 3244.
- [90] F. Zhao, Y. Guo, X. Zhou, W. Shi, G. Yu, *Nat. Rev. Mater.* **2020**, *5*, 388.
- [91] F. Zhao, X. Zhou, Y. Shi, X. Qian, M. Alexander, X. Zhao, S. Mendez, R. Yang, L. Qu, G. Yu, *Nat. Nanotechnol.* **2018**, *13*, 489.
- [92] X. Zhou, F. Zhao, Y. Guo, B. Rosenberger, G. Yu, *Sci. Adv.* **2019**, *5*, eaaw5484.
- [93] G. Liu, T. Chen, J. Xu, G. Yao, J. Xie, Y. Cheng, Z. Miao, K. Wang, *Cell Reports Phys. Sci.* **2021**, *2*, 100310.
- [94] F. Nawaz, Y. Yang, S. Zhao, M. Sheng, C. Pan, W. Que, *J. Mater. Chem. A* **2021**, *9*, 16233.

- [95] H. Ren, M. Tang, B. Guan, K. Wang, J. Yang, F. Wang, M. Wang, J. Shan, Z. Chen, D. Wei, H. Peng, Z. Liu, *Adv. Mater.* **2017**, *29*, 1702590.
- [96] Y. Kuang, C. Chen, S. He, E. M. Hitz, Y. Wang, W. Gan, R. Mi, L. Hu, *Adv. Mater.* **2019**, *31*, 1900498.
- [97] N. Xu, H. Zhang, Z. Lin, J. Li, G. Liu, X. Li, W. Zhao, X. Min, P. Yao, L. Zhou, Y. Song, B. Zhu, S. Zhu, J. Zhu, *Natl. Sci. Rev.* **2021**, *8*, nwab065.
- [98] W. Xu, X. Hu, S. Zhuang, Y. Wang, X. Li, L. Zhou, S. Zhu, J. Zhu, *Adv. Energy Mater.* **2018**, *8*, 1702884.
- [99] L. Zhu, L. Sun, H. Zhang, H. Aslan, Y. Sun, Y. Huang, F. Rosei, M. Yu, *Energy Environ. Sci.* **2021**, *14*, 2451.
- [100] J. Chen, J. L. Yin, B. Li, Z. Ye, D. Liu, D. Ding, F. Qian, N. V. Myung, Q. Zhang, Y. Yin, *ACS Nano* **2020**, *14*, 17419.
- [101] T. A. Cooper, S. H. Zandavi, G. W. Ni, Y. Tsurimaki, Y. Huang, S. V. Boriskina, G. Chen, *Nat. Commun.* **2018**, *9*, 5086.
- [102] Y. Xia, Q. Hou, H. Jubaer, Y. Li, Y. Kang, S. Yuan, H. Liu, M. W. Woo, L. Zhang, L. Gao, H. Wang, X. Zhang, *Energy Environ. Sci.* **2019**, *12*, 1840.
- [103] Y. Shi, C. Zhang, R. Li, S. Zhuo, Y. Jin, L. Shi, S. Hong, J. Chang, C. Ong, P. Wang, *Environ. Sci. Technol.* **2018**, *52*, 11822.
- [104] L. Wu, Z. Dong, Z. Cai, T. Ganapathy, N. X. Fang, C. Li, C. Yu, Y. Zhang, Y. Song, *Nat. Commun.* **2020**, *11*, 521.
- [105] L. Zhao, C. Du, C. Zhou, S. Sun, Y. Jia, J. Yuan, G. Song, X. Zhou, Q. Zhao, S. Yang, *ACS Sustain. Chem. Eng.* **2020**, *8*, 4362.
- [106] L. Noureen, Z. Xie, Y. Gao, M. Li, M. Hussain, K. Wang, L. Zhang, J. Zhu, *ACS Appl. Mater. Interfaces* **2020**, *12*, 6343.
- [107] Y. Zhang, T. Xiong, D. K. Nandakumar, S. C. Tan, *Adv. Sci.* **2020**, *7*, 1903478.
- [108] T. Ding, Y. Zhou, W. L. Ong, G. W. Ho, *Mater. Today* **2021**, *42*, 178.
- [109] Z. Xu, Z. Li, Y. Jiang, G. Xu, M. Zhu, W.-C. Law, K.-T. Yong, Y. Wang, C. Yang, B. Dong, F. Xing, *J. Mater. Chem. A* **2020**, *8*, 25571.
- [110] R. Bhardwaj, M. V. ten Kortenaar, R. F. Mudde, *Desalination* **2013**, *326*, 37.
- [111] Z. M. Omara, A. S. Abdullah, A. E. Kabeel, F. A. Essa, *Renew. Sustain. Energy Rev.* **2017**, *78*, 176.
- [112] R. Bhardwaj, M. V. ten Kortenaar, R. F. Mudde, *Appl. Energy* **2015**, *154*, 480.
- [113] L. Zhang, B. Tang, J. Wu, R. Li, P. Wang, *Adv. Mater.* **2015**, *27*, 4889.
- [114] W. Li, Z. Li, K. Bertelsmann, D. E. Fan, *Adv. Mater.* **2019**, *31*, 1900720.

- [115] E. Chiavazzo, M. Morciano, F. Viglino, M. Fasano, P. Asinari, *Nat. Sustain.* **2018**, *1*, 763.
- [116] Z. Xu, L. Zhang, L. Zhao, B. Li, B. Bhatia, C. Wang, K. L. Wilke, Y. Song, O. Labban, J. H. Lienhard, R. Wang, E. N. Wang, *Energy Environ. Sci.* **2020**, *13*, 830.
- [117] H. Chen, S.-L. Wu, H.-L. Wang, Q.-Y. Wu, H.-C. Yang, *Adv. Energy Sustain. Res.* **2021**, *2*, 2000056.
- [118] X. Zhou, F. Zhao, P. Zhang, G. Yu, *ACS Mater. Lett.* **2021**, *3*, 1112.
- [119] L. Wang, Y. Feng, Q. Liu, G. Liu, *Sol. Energy* **2023**, *250*, 347.
- [120] C. Lei, W. Guan, Y. Guo, W. Shi, Y. Wang, K. P. Johnston, G. Yu, *Angew. Chemie Int. Ed.* **2022**, *61*, e202208487.
- [121] W. Li, M. C. Tekell, Y. Huang, K. Bertelsmann, M. Lau, D. Fan, *Adv. Energy Mater.* **2018**, *8*, 1802108.
- [122] P. Zhang, Q. Liao, T. Zhang, H. Cheng, Y. Huang, C. Yang, C. Li, L. Jiang, L. Qu, *Nano Energy* **2018**, *46*, 415.
- [123] M. Gao, C. K. Peh, L. Zhu, G. Yilmaz, G. W. Ho, *Adv. Energy Mater.* **2020**, *10*, 2000925.
- [124] O. Neumann, A. D. Neumann, S. Tian, C. Thibodeaux, S. Shubhankar, J. Müller, E. Silva, A. Alabastri, S. W. Bishnoi, P. Nordlander, N. J. Halas, *ACS Energy Lett.* **2017**, *2*, 8.
- [125] X. Li, X. Min, J. Li, N. Xu, P. Zhu, B. Zhu, S. Zhu, J. Zhu, *Joule* **2018**, *2*, 2477.
- [126] L. Zhu, M. Gao, C. K. N. Peh, X. Wang, G. W. Ho, *Adv. Energy Mater.* **2018**, *8*, 1702149.
- [127] L. Zhu, T. Ding, M. Gao, C. K. N. Peh, G. W. Ho, *Adv. Energy Mater.* **2019**, *9*, 1900250.
- [128] P. Yang, K. Liu, Q. Chen, J. Li, J. Duan, G. Xue, Z. Xu, W. Xie, J. Zhou, *Energy Environ. Sci.* **2017**, *10*, 1923.

## **Chapter 3**

# **Synthesis and Characterization Techniques of Photothermal Materials**

Introduction

Synthesis of nanomaterials

Characterizations of photothermal materials

References

### 3.1. Introduction

The advances in nanotechnology have shown a fast growth of photothermal materials through new material development.<sup>[1]</sup> Compared to the bulk, NPs are small particles of size  $10^{-9}$  meters, with unique physical and chemical properties.<sup>[2,3]</sup> In photothermal nanomaterials, the light absorption ability and hence the evaporation performance is highly dependent on the nanoparticle's shape, size, and morphology. For example, Wang *et al.* reported the synthesis of  $\text{Ti}_2\text{O}_3$  NPs in which the light absorption was increased by reducing the nanoparticle size.<sup>[4]</sup> Also, Zhang *et al.* synthesized the  $\text{Cu}_7\text{S}_4$  nanocrystals of a disk-like and spherical shape and found higher evaporation performance for nanodisks than nanospheres which were because of the higher NIR absorption capability of nanodisks compared to nanospheres.<sup>[5]</sup> The precise control of the size and morphology of NPs is of great importance in preparing highly-ordered mesoscopic structures, which is considered a promising and inexpensive way to create devices with unique properties.<sup>[6]</sup> Determination of the nanoparticle structures and their chemical nature are crucial in understanding how the material properties are related to their physical properties towards photothermal applications.<sup>[7]</sup> These properties are measured by using various characterization techniques.

### 3.2. Synthesis of nanomaterials

Several methods have been used to synthesize nanomaterials and, in general, are broadly classified into two categories a) top-down and b) bottom-up techniques.<sup>[8]</sup> In top-down approaches, the bulk materials are mechanically machined and converted into fine particles in nano dimensions, and in bottom-up approaches, the atomic clusters are assembled to build the nanomaterials.<sup>[8]</sup> The top-down technique includes physical vapor deposition, lithography, and pyrolysis. The bottom-up approach includes methods like sol-gel, chemical vapor deposition, chemical co-precipitation, micro-emulsions, solvothermal, and microwave methods.<sup>[9]</sup>

Among the different methods of the bottom-up approach, solvothermal synthesis has become one of the most common over the last decade because of its advantages, like low process temperature, the performance of reactions in liquid environments, low energy consumption, and environmental friendliness.<sup>[9]</sup> This method is used to prepare nanomaterials of high crystallinity, desired morphology, and size control and involves the use of solvent under moderate to high pressure and temperature that facilitates the interaction of precursors during synthesis. Generally, the pressure in this method typically varies from 1 to 10,000 atm, and the temperature ranges from 100 and 1000 °C.<sup>[10]</sup> In a particular case, if water is used as the solvent,

the technique is often called hydrothermal, in which the synthesis is usually performed below the supercritical temperature of water (374 °C).<sup>[11]</sup> Nanomaterials of different sizes and shapes, including NPs, nanorods, nanotubes, hollow nanospheres, and graphene nanosheets, have been prepared using the hydrothermal method.<sup>[10]</sup> This method has some advantages over the other commonly used approaches of nanomaterial synthesis. First, this method can be used to prepare the NPs which are not stable at high temperatures. Second, with minimal loss of materials, this method can generate nanomaterials of high vapor pressures. Third, through a liquid phase or multiphase chemical reactions, the compositions of nanomaterials can be well controlled.<sup>[10]</sup>

The particle size, shape, or morphology of the final product in the hydrothermal method strongly depends on the processing parameters like temperature, pH, reactant concentrations, and additives.<sup>[9]</sup> The crystallization process in this method involves two steps i) crystal nucleation and ii) subsequent growth.<sup>[12]</sup> In hydrothermal synthesis, the solubility of the solute is essential for the growth of crystals out of the solution and is strongly dependent on the precipitation rate. The solution must be supersaturated for nanomaterials to form or for the nucleation process to occur. The supersaturation ( $S_s$ ) is defined as the ratio of the actual concentration ( $c_a$ ) to the saturation concentration ( $c_s$ ) of the species in the solution, given as<sup>[13]</sup>

$$S_s = \frac{c_a}{c_s} \quad (3.1)$$

For a supersaturated solution, the  $S_s$  is always greater than one. Therefore, the overall nucleation and growth rates which finally decide the size and morphology of the nanomaterials, depend on  $S_s$ .<sup>[14]</sup> The hydrothermal reactions generally proceed in a sealed reactor known as an autoclave made of stainless steel (SS) case with a Teflon tube.

Photothermal nanomaterials with different shapes, sizes, and morphologies have been synthesized by the hydrothermal method. The pore sizes of a photothermal material, which play an important part in dictating the light absorption ability of the material, can also be decided by the hydrothermal method. Hydrothermal time is another parameter on which the photothermal material's light absorption property and hence the evaporation performance depends. For example, Zhang *et al.* reported MoS<sub>2</sub>/bio-carbon foam composites prepared using the hydrothermal route,<sup>[15]</sup> and by changing the hydrothermal time from 0 to 20 h, they achieved a varying ER from 1.28 to 1.41 kg m<sup>-2</sup> h<sup>-1</sup>.

### **3.3. Characterizations of photothermal materials**

All modern-day materials must be characterized to understand the chemical compositions and structural properties and their relationships with their physical properties. In the present work,

various characterization techniques are used to study different properties of synthesized photothermal materials, including crystalline structure, morphology, surface properties, chemical composition, and optical absorptions. The techniques used for these investigations include Field Emission Scanning Electron Microscopy (FESEM), Energy Dispersive X-Ray Spectroscopy (EDX), UV-vis-NIR spectroscopy, Fourier-Transform Infrared Spectroscopy (FTIR), X-Ray diffraction (XRD) measurements, and X-Ray Photoelectron Spectroscopy (XPS). The following sections will discuss these techniques elaborately.

### 3.3.1. X-ray diffraction

X-rays, first discovered in 1895 by Wilhelm Conrad Roentgen, are electromagnetic radiations of wavelength ranging from 0.01 to 10 nm which is comparable to the atomic size. When the X-ray beam is incident on the atomic planes of a crystal, they interfere with one another after coming out of the crystal. This process is called X-ray diffraction. The technique of XRD is used to identify the phase and provides information about the unit cell dimensions of crystalline material.

Max von Laue discovered in 1912 that a crystalline material acts as a 3D grating for X-rays wavelength, similar to the spacing of planes in a crystal lattice. Therefore, the XRD technique can determine the crystal structure and atomic spacing. In a crystal, there are many families of sets of parallel planes with different interplanar spacing ( $d$ ) values and different orientations for each family. When a monochromatic beam of X-rays with wavelength  $\lambda$  is

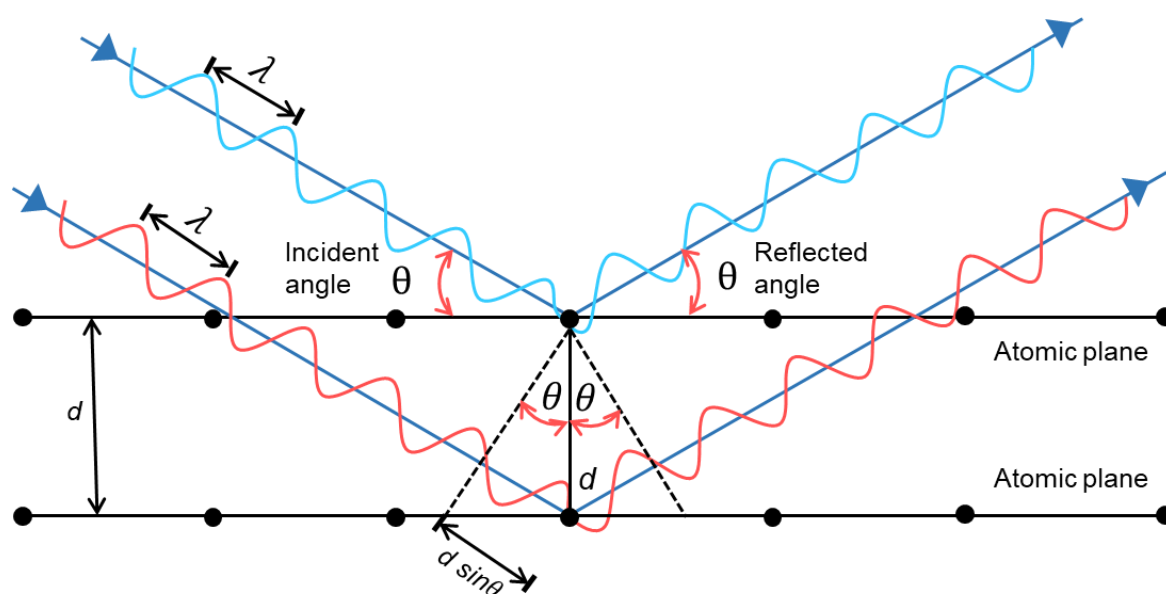


**Figure 3.1.** Reflection of X-rays from two planes of atoms in a solid.

incident on a crystal lattice on an angle  $\theta$  (Figure 3.1), the interaction of the incident rays with the sample produces constructive interference when conditions satisfy Bragg's Law:

$$n\lambda = 2d\sin\theta \quad (3.2)$$

where  $n$  is an integer 1, 2, 3... (usually equal to 1). The intensity of diffracted X-rays is then recorded by rotating both the sample and the detector through a range of  $2\theta$  angles. Constructive interference occurs when the X-rays impinging the sample satisfy the Bragg law, leading to peak formation in the intensity pattern. The identifications of the specified samples are made by converting the diffraction peaks to d-spacings because each material has a set of unique d-spacings. Typically, this is achieved by comparison of d-spacings with standard reference patterns.

### **3.3.2. Scanning electron microscopy**

The SEM technique reveals information including morphology (texture), particle size, particle shape, chemical composition, crystalline structure, and orientation of materials of which the sample is made. Unlike the conventional microscope, where visible lights are used for focussing, SEM uses a focused beam of high-energy electrons to generate signals at the surface of the sample. In conventional SEM techniques having magnification ranging from 20X to approximately 30,000X and spatial resolution of 50 to 100 nm, the areas ranging from 1 cm to 5  $\mu\text{m}$  in width can be imaged in a scanning mode.

In a typical FESEM, the electrons are produced by an electron gun with a field emission cathode (Figure 3.2). Under vacuum, electrons generated by a field emission source are accelerated with a field gradient. The beam passes through electromagnetic lenses, focusing on the specimen. The beam of electrons interacts with the sample to produce signals that give information about the surface topography and composition of the specimen. The kinetic energy of electrons is dissipated in different kinds of signals, including backscattered electrons, secondary electrons, X-rays, and diffracted electrons. To check the sample's morphology, the detector collects the secondary electrons and transforms these into an image, while the backscattered electrons determine the composition of the elements within the specimen. The SEM produces 2D images and reveals the sample's topographic features, allowing us to examine photothermal nanomaterials' diameter, length, shape, and density.

The X-rays emitted from the specimen after bombarding by the high energy electron beam consist of the compositional information about the sample. This is generally done with an EDX spectrometer attached to SEM. EDS X-ray data can be used to determine the elements

in the sample as X-rays are characteristic of the elements in the sample. The X-ray data mapped as a function of spatial position provides the distribution of the elements in the sample.

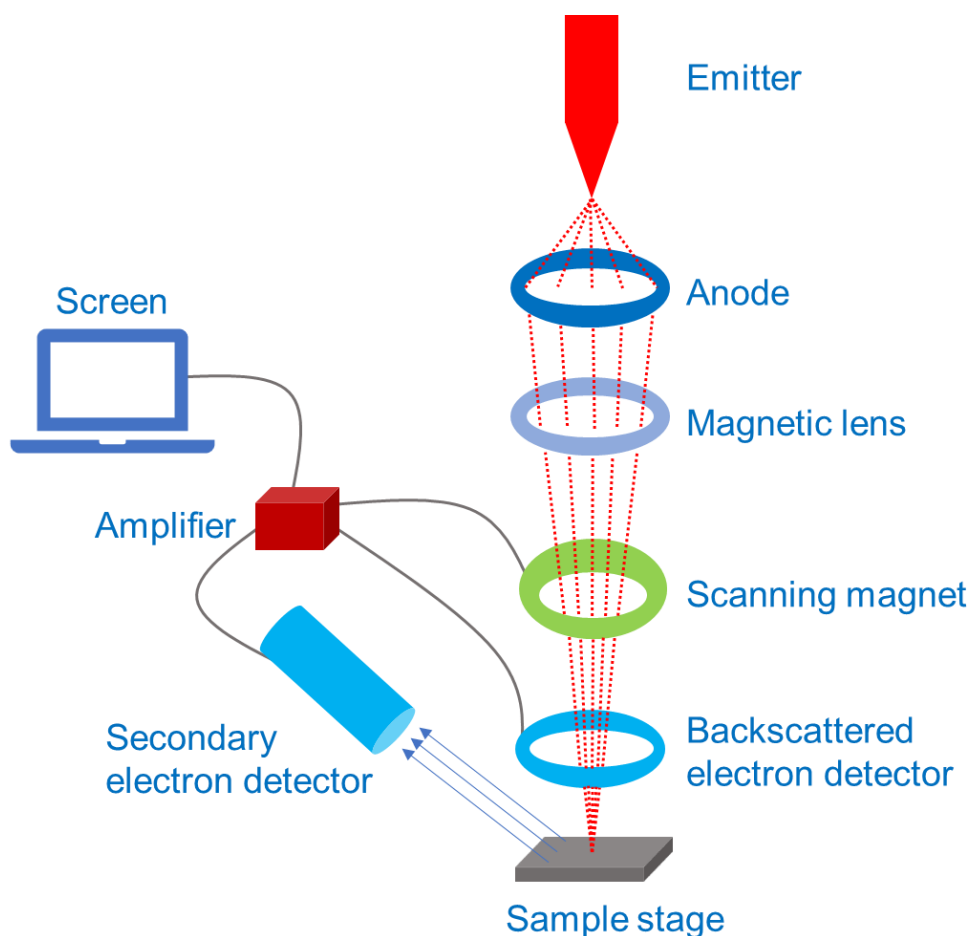


**Figure 3.2.** Schematic diagram of an FESEM.

### 3.3.3. UV-vis-NIR spectroscopy

UV-vis-NIR spectroscopy determines the interaction between materials and electromagnetic radiation in the wavelength range of around 200 - 3000 nm. UV-vis-NIR spectroscopy is used to determine the optical properties (transmittance, reflectance, and absorbance) of both liquids and solids by monitoring the specific wavelengths they absorb, scatter, and reflect. The principle of UV-vis-NIR spectroscopy is recording the intensity of the light that reaches a detector after the interaction with the sample. On the incidence of light of a specific wavelength on a material, the loss in the intensity of the incident light is recorded by the detector and compared with the intensity of the incident beam to find the absorption, reflection, and transmission ability of the sample. Based on the nature of the sample, the strategy to determine the intensity of the scattered light needs to be modified.

### 3.3.3.1. Analysis of liquid samples

UV-vis-NIR spectroscopy is used to determine the concentrations of any material in a solution. The technique measures the absorption of light in a desired wavelength range. In the actual experiment, two transparent cuvettes are parallelly placed in the path between the light source and a detector, one filled with the sample solution being analyzed (named C1) and the other with only the solvent (C2). A beam of light coming from the light source is split into two halves, with one half passing through C1 and the other half directed through C2 (Figure 3.3).

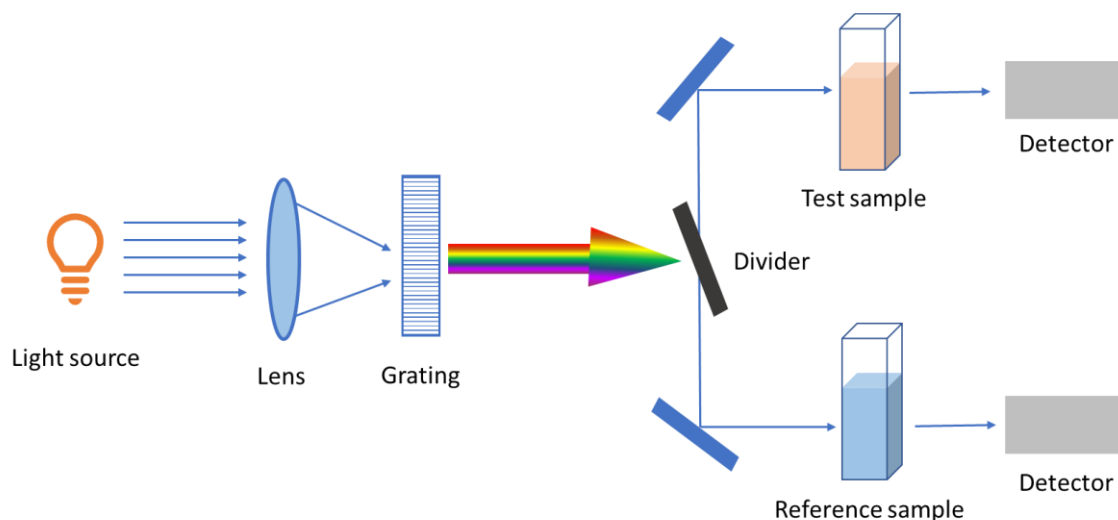


**Figure 3.2.** Block diagram of UV-vis-NIR spectrophotometer.

The instrument is designed so that it can compare the intensities of two beams as it scans over the preferred region of the wavelengths. If the compound absorbs the light at a particular wavelength, the intensity of the sample beam will be less than the reference beam. The radiation absorbed by a sample is measured at various wavelengths, and a plot of the wavelength versus the absorption ( $A$ ) of light provides the final spectrum. The concentration of a sample can be determined from the light absorbed at a wavelength using the Beer-Lambert law.

$$I = I_0 \exp(-c\gamma l) \quad (3.3)$$

where  $I$  is the intensity,  $I_0$  is the intensity of the incident beam,  $c$  is the concentration of the sample in the solution,  $\gamma$  is the molar extinction coefficient, and  $l$  is the path length.

### 3.3.3.2. Analysis of powder samples

Aside from transmission and absorption, UV-vis-NIR spectroscopy can also measure the diffuse reflectance of a powder sample by using an additional accessory called an integrating sphere. Unlike specular reflectance, in diffused reflectance, the incident light scatters in different directions. To measure the amount of diffuse reflected light, the sample is placed in

front of the incident light window of the integrating sphere (Figure 3.4a). Then the light reflected from the sample is made to concentrate on the detector using a sphere coated inside with barium sulfate or spectralon (the whitest known materials). The obtained values give the sample's reflectance (relative reflectance) in reference to the standard whiteboard of 100% reflectance. The measurements are done so that only diffuse reflected light is measured without the contribution of specular reflectance. The diffused reflectance of some 3D structures

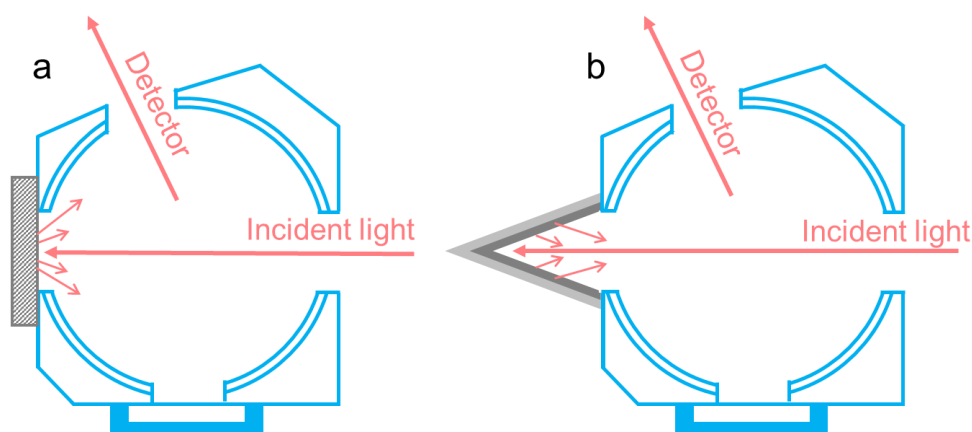


**Figure 3.4.** Schematic illustration of measurement of diffuse reflectance of a (a) 2D film sample and (b) cone-shaped sample using an integrating sphere.

(conical, cylindrical, *etc.*) can also be measured in the same way as that of powders by directly placing a 3D design in front of the window of the sphere, as shown in Figure 3.4b.

The absorbance in the photothermal materials is calculated by using the equation (3.4)

$$%A = 100 - \%R - \%T \quad (3.4)$$

For opaque samples, the transmittance is considered zero, and therefore the absorbance is given as

$$%A = 100 - \%R \quad (3.5)$$

### 3.3.3.3. Band gap energies analysis

An exciting application of the UV-vis-NIR spectroscopy technique is the calculations of the band gap of any semiconductor. A semiconductor absorbs the photons with energy higher than the band gap and shows no absorption for the photons with energies lower than its band gap. Therefore, in the spectrum, the band gap of any semiconductor corresponds to the point at which the absorption starts to increase. The band gap calculations involve the plotting and fitting of the collected data to the expected trend lines for direct and indirect band gap semiconductors. The first step is the calculation of the absorption coefficient using equation (3.6).

$$\beta(\text{cm}^{-1}) = \frac{\ln(10) \times A}{l(\text{cm})} \quad (3.6)$$

where  $l$  is the path length of the light through the material. The materials with  $\beta > 10^{-4} \text{ cm}^{-1}$  generally follow Tauc's relation given as

$$\beta h\nu \propto (h\nu - E_g)^\kappa \quad (3.7)$$

where  $\kappa = 2$  corresponds to the indirect band gap and  $\kappa = \frac{1}{2}$  corresponds to direct band gap semiconductors. The graphs between  $h\nu$  (on x-axis) and  $(\beta h\nu)^\kappa$  (on y-axis) are plotted, which are called Tauc plots. The point on the x-axis where the tangent of the Tauc plot (drawn at the region of the peak with constant positive slope) cuts yields the optical band gap in eV for that particular material.

### 3.3.4. Fourier transform infrared spectroscopy

FTIR Spectroscopy is an analytical technique that provides information about the chemical bonding or molecular structure in organic or inorganic materials. When the IR radiation absorbed by the sample interacts with a molecule, the vibrations in the sample are initiated. The sample will absorb the radiations of a specific energy that produces a change in the permanent electric dipole moment of the molecule. An individual functional group in a molecule is associated with a unique vibrational energy. Therefore, a specific band of the IR spectrum is used to detect a particular functional group of the sample.

Michelson interferometer is the key component in an FTIR instrument consisting of a source, beam splitter, two mirrors, and a detector (Figure 3.5). The source generates a beam of IR light that is made to strike the beam splitter. At the beam splitter, a part of the light is reflected toward the fixed mirror, and the remaining portion of the light is transmitted onto the

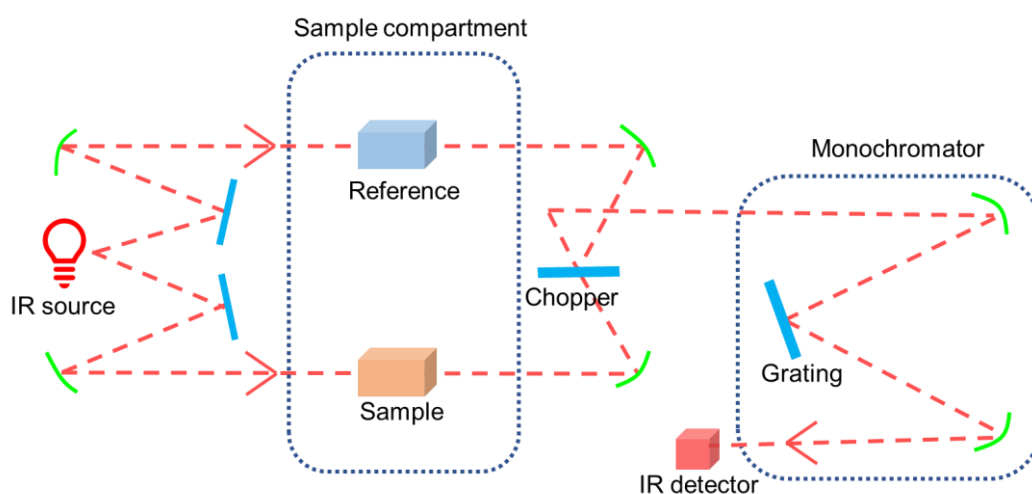


**Figure 3.5.** Schematic diagram of FTIR spectrometer.

moving mirror. After reflection from the mirrors, the two beams recombined back at the beam splitter and interfered constructively or destructively, resulting in an interference pattern. The interference pattern is then transmitted through the sample to the detector, where it is converted into an electrical signal. The signal is then subjected to Fourier Transformation to generate the spectrum. The amplitude of each component signal is calculated, giving the intensity at the corresponding wavelength of light.

### 3.3.5. X-ray photoelectron spectroscopy

XPS is considered the fingerprint of the chemical composition of samples as the characteristic X-ray has discrete nature for each element. XPS analyzes the outermost surface of material up to the depth of around 10 nm (~30 atomic layers) and helps to determine the elemental composition and the abundance of these components on material surfaces. The chemical state of polyvalent ions can also be measured by measuring the binding energies of elements related to the nature and strength of their chemical bonds. Different photothermal materials, such as inorganic and organic compounds and semiconductors, can be characterized using the XPS technique.

XPS works on the principle of the photoelectric effect, in which photoelectrons are released from or within a material after interaction with incident X-ray photons. The photoelectrons are emitted from a material when the energy of incident photons exceed the binding energy of electrons in that material. The kinetic energy of an emitted electron is related to the binding energy of each electron. Since the atoms have multiple orbitals at different energy states, the resulting response will be a range of emitted electrons of different binding or kinetic energies, producing an XPS spectrum. The equation (3.8) gives the mathematical relation for the photoelectric effect

$$E_{kinetic} = E_{photon} - E_{binding} - \varphi_{spec} \quad (3.8)$$

where  $E_{kinetic}$  is the kinetic energy of the photoelectron,  $E_{photon}$  is the energy of the incident photon,  $E_{binding}$  is the binding energy of a given electron, and  $\varphi_{spec}$  is the spectrometer work function.  $E_{photon}$  is the kinetic energy of the X-rays being used by the instrument, which is a fixed quantity.  $E_{photon}$  and  $\varphi_{spec}$  are known quantities and  $E_{kinetic}$  is measured by the detector, which leaves  $E_{binding}$  as the only unknown that can be determined from equation (3.9).

$$E_{binding} = E_{photon} - E_{kinetic} - \varphi_{spec} \quad (3.9)$$

Here  $E_{binding}$  is measured with respect to the sample fermi level (not the vacuum level), which is the reason that  $\varphi_{spec}$  is included (Figure 3.6).

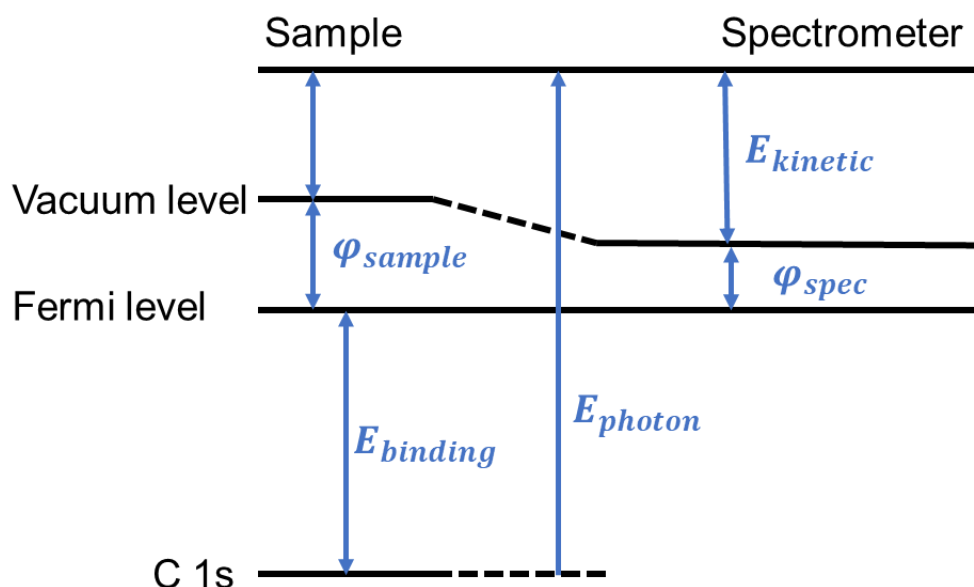


**Figure 3.6.** Energy level diagram illustrates the basic XPS equation.

The XPS instrument typically operates at high vacuum conditions of around  $< 10^{-9}$  Torr in order to prevent the photoelectrons having relatively small mean free path from absorbing by the ambient atmosphere. The X-rays of fixed energy are made to fall on the sample, which results in the ejection of the photoelectrons of certain kinetic energy. The binding energy of an electron, being a material property, is independent of the X-ray source used to eject it. During the experiments, by changing the different X-ray sources, the binding energy of photoelectrons will not change; however, the kinetic energy will vary. The ejected photoelectrons were analyzed using a plot of energy and a relative number of photoelectrons. The photoelectrons of different energies follow different paths to the detector, which helps the computer to differentiate the electrons to produce the final spectrum.

### 3.3.6. Brunauer-Emmett-Teller analysis

When the size of the particles of any bulk material is reduced to the nano level, the surface area to volume ratio increases many folds, and then different properties begin to arise. Various physical properties of the nanomaterial, including mechanical, electrical, optical, *etc.*, change significantly compared to their bulk. Many useful properties of photothermal nanomaterials are due to their small size, porosity, and high surface area. In SSG, the porous structure of a photothermal nanomaterial plays an important role in enhancing evaporation performance by increasing solar absorption, surface wettability, and evaporation area. Therefore, it becomes

essential to determine the surface area of any photothermal material. BET is an analytical technique for determining the surface areas and pore size distributions of a material.

In the BET analysis, the material is placed in a sample cell for degassing to remove water and other contaminants (Figure 3.7). An inert gas, commonly nitrogen, is made to adsorb on the surface of the sample. This adsorption occurs on the outer and inner surfaces of the pores (in the case of porous material). The amount of gas adsorbed on the material surface depends on many factors, including the exposed surface area, temperature, gas pressure, and strength of interaction between the nitrogen and sample. The specimen is kept at a low temperature for good adsorption using Dewars of liquid nitrogen and is made to adsorb the nitrogen gas stepwise by increasing the pressure of the gas (measured by highly precise and accurate pressure transducers) until the saturation point comes. After this, the sample is heated to release the adsorbed monolayer of nitrogen gas molecules from the surface and then quantified to

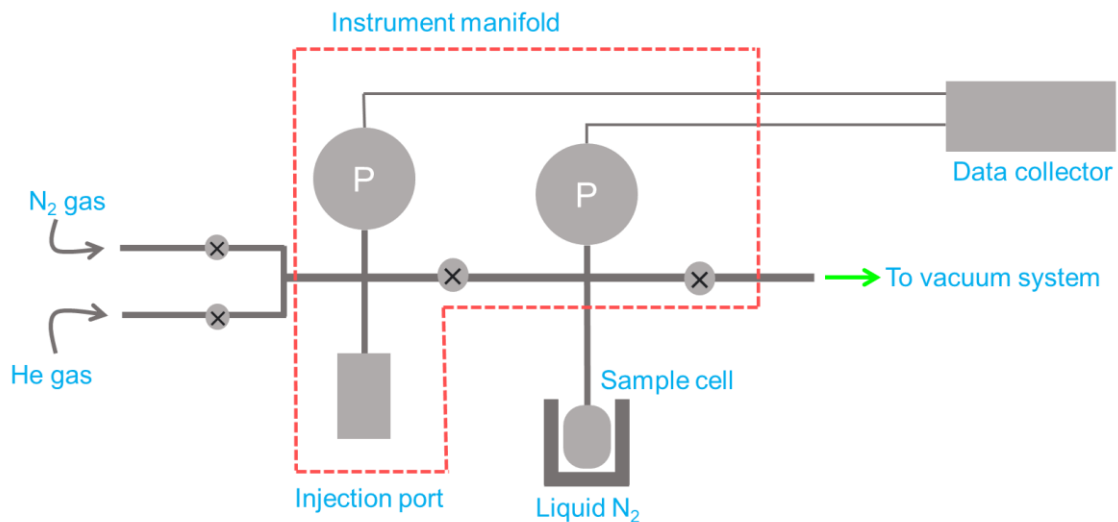


**Figure 3.7.** Block diagram of BET setup.

calculate the surface area and the porosity of the sample. The data is then plotted between the amount of gas adsorbed and relative pressure to produce a curve called a BET isotherm.

The equation (3.10) is used for the BET isotherm for the calculation of the surface area of the sample

$$\frac{1}{W[(\frac{P_0}{P})-1]} = \frac{1}{W_m K} + \frac{K-1}{W_m K} (\frac{P}{P_0}) \quad (3.10)$$

where  $W$  is the weight of nitrogen gas adsorbed at a given relative pressure ( $P/P_0$ ),  $W_m$  is monolayer capacity, which is the volume of gas adsorbed at STP, and  $K$  is BET constant.

A minimum of three data points in the  $\frac{P_0}{P}$  range of 0.025 to 0.30 are enough to determine the surface area using the equation (3.10). The equation gives a linear curve with

slope =  $\frac{K-1}{W_m K}$  and intercept =  $\frac{1}{W_m K}$ , from which both  $W_m$  and  $K$  are being calculated. After calculating  $W_m$  the total surface area  $S_t$  is determined using the equation (3.11)

$$S_t = \frac{W_m N s_g}{V_m} \quad (3.11)$$

where  $N$  is Avogadro's number,  $s_g$  is the cross-sectional area of the adsorbed gas molecules and equals  $0.162 \text{ nm}^2$  nitrogen gas, and  $V_m$  is the molar volume and equals  $22414 \text{ mL}$ . The specific surface area in  $\text{m}^2/\text{g}$  is determined by dividing  $S_t$  by the mass of the sample.

### 3.4. References

- [1] C. Chen, Y. Kuang, L. Hu, *Joule* **2019**, *3*, 683.
- [2] M. A. Hines, P. Guyot-Sionnest, *J. Phys. Chem.* **1996**, *100*, 468.
- [3] H. Goesmann, C. Feldmann, *Angew. Chemie Int. Ed.* **2010**, *49*, 1362.
- [4] J. Wang, Y. Li, L. Deng, N. Wei, Y. Weng, S. Dong, D. Qi, J. Qiu, X. Chen, T. Wu, *Adv. Mater.* **2017**, *29*, 1603730.
- [5] C. Zhang, C. Yan, Z. Xue, W. Yu, Y. Xie, T. Wang, *Small* **2016**, *12*, 5320.
- [6] Z. Nie, A. Petukhova, E. Kumacheva, *Nat. Nanotechnol.* **2010**, *5*, 15-25.
- [7] C. J. Gommers, G. Prieto, J. Zecevic, M. Vanhalle, B. Goderis, K. P. de Jong, P. E. de Jongh, *Angew. Chemie Int. Ed.* **2015**, *54*, 11804.
- [8] N. Abid, A. M. Khan, S. Shujait, K. Chaudhary, M. Ikram, M. Imran, J. Haider, M. Khan, Q. Khan, M. Maqbool, *Adv. Colloid Interface Sci.* **2022**, *300*, 102597.
- [9] G. Amin, M. H. Asif, A. Zainelabdin, S. Zaman, O. Nur, M. Willander, *J. Nanomater.* **2011**, *2011*, 269692.
- [10] S.-H. Feng, G.-H. Li, in *Mod. Inorg. Synth. Chem.* Elsevier, Amsterdam, **2017**, pp. 73–104.
- [11] H. Hayashi, Y. Hakuta, *Materials* **2010**, *3*, 3794.
- [12] C. Burda, X. Chen, R. Narayanan, M. A. El-Sayed, *Chem. Rev.* **2005**, *105*, 1025.
- [13] T. Andelman, M. C. Tan, R. E. Riman, *Mater. Res. Innov.* **2010**, *14*, 9.
- [14] K. Sue, M. Suzuki, K. Arai, T. Ohashi, H. Ura, K. Matsui, Y. Hakuta, H. Hayashi, M. Watanabe, T. Hiaki, *Green Chem.* **2006**, *8*, 634.
- [15] X. Zhang, G. Wu, X.-C. Yang, *ACS Appl. Nano Mater.* **2020**, *3*, 9706.

## **Chapter 4**

# **Coconut Husk as Photothermal Material for Highly Efficient Solar Steam Generation**

Introduction

Experimental section

Results and discussion

Conclusion

References

## 4.1. Introduction

As discussed earlier, the solar-driven water evaporation technique to produce clean water has shown enormous potential as an energy-efficient solution for global freshwater scarcity. Various novel materials with efficient sunlight absorption ability and photothermal properties have been adopted in the past decade.<sup>[1–3]</sup> Among these materials, the carbon-based absorber materials are of high stability and low cost, making them ideal contingents for ISSG applications. As a result, different carbon-based nanomaterials, such as CNTs, graphite, graphene, GO, rGO, and carbon hybrid composites, have been developed as solar absorbers for solar-driven water evaporation.<sup>[1]</sup>

Photothermal materials derived from natural products have recently gained much interest due to their various advantages, such as biodegradability, abundance, low thermal conductivity, low-cost, natural capillary mechanism, and hydrophilicity.<sup>[4–6]</sup> But the carbonization of plants requires high-temperature annealing under a controlled environment. High-temperature annealing destroys the mechanical strength and surface morphology of plants.<sup>[7]</sup> Uniform deposition of the carbonized species on a substrate or self-assembling them in the desired form creates difficulties in the large-scale design of ISSGs. The low efficiency of plant-based ISSGs is one of the significant challenges; for example, ISSGs made from mushrooms,<sup>[8]</sup> lotus seeds,<sup>[9]</sup> daikon,<sup>[9]</sup> potato,<sup>[10]</sup> rice husk,<sup>[11]</sup> sugarcane,<sup>[12]</sup> and banana peels<sup>[13]</sup> have an ER of less than  $1.5 \text{ kg m}^{-2} \text{ h}^{-1}$  under 1 sun illumination. Industry-scale availability of some of these plants might be a challenge as well. Although the ER of bamboo stem-based ISSGs has been reported to be  $3.1 \text{ kg m}^{-2} \text{ h}^{-1}$ , it requires multistage annealing of the bamboo stem at different temperatures as high as  $1200 \text{ }^\circ\text{C}$ , which restricts its feasibility for practical applications.<sup>[14]</sup> Finding a plant-based source material with large-scale availability, simple design techniques, and efficient ISSG performance can lead to an affordable solution for freshwater generation.

Coconut (*Cocos nucifera*) belongs to the Arecaceae family. Almost every part of the coconut plant has been used in diverse applications due to its advantages, such as availability in large quantities, low-cost, renewable, eco-friendly, and biodegradable nature.<sup>[15,16]</sup> Among all the coconut plant products, the coconut husk is reported as the most underutilized resource, and it causes environmental pollution.<sup>[17]</sup> Designing ISSGs using coconut husk will further improve ecological management. Coconut husk has very low thermal conductivity and potential applications in the thermal insulation layer.<sup>[18]</sup> Coconut plant-based materials are known to have high porosity, which helps water conduction by capillary action. Hence,

designing ISSGs using coconut husk is expected to have higher efficiency. The high mechanical strength of coconut coir<sup>[19]</sup> and the resiliency of coconut husk in water will also prolong the evaporator's durability.

In this chapter, a 3D cylindrical ISSG was prepared by flaming the surface of the coconut husk under environmental conditions using a liquefied petroleum gas (LPG) stove. Our flamed coconut husk (FCH)-based evaporators show a maximum ER of  $3.6 \text{ kg m}^{-2} \text{ h}^{-1}$  under 1 sun illumination and offer a thermal efficiency of 144%. Although the ER is comparable to that of other reported 3D ISSGs, the easy processability combined with negligible material cost and high stability of coconut husk in water establish the superiority of FCH for practical applications. The ER remains unaffected up to a measured time of 10 hours during continuous steam generation from seawater and has the capability of self-cleaning under dark conditions. The evaporation efficiency remains unchanged for higher intensities and multiple cycles as well. The efficient evaporation capacity of FCH evaporators can be attributed to the increased surface area, effective three-dimensional structure, and the capability of heat harvesting from the environment through their larger cylindrical facet.

## 4.2. Experimental section

### 4.2.1. Materials

MB, NaCl, and KOH were purchased from Sigma Aldrich and were used without further purification.

### 4.2.2. Fabrication of FCH evaporator

To prepare FCH evaporators, raw coconut husk (RCH) collected from the coconut was cut into pieces and washed thoroughly using KOH solution followed by DI water. Then the husk was compressed tightly by a rope into a cylindrical shape, followed by drying overnight at  $70 \text{ }^\circ\text{C}$  in an oven (Figure 4.1). Finally, the dried cylindrical coconut husk was unroped (cylindrical shape



**Figure 4.1.** Photographs showing stepwise fabrication of FCH-based evaporator.

was well maintained) and carbonized its cylindrical surfaces as well as the top surface using a household LPG stove in an environmental condition. To restrict the burning only to the surface of FCH, the flaming process was limited to a short period, followed by dipping in DI water that prevents the internal part from burning. The cross-section image of the FCH (extreme right) shows that only the surface has been burnt, and the bulk remains the same, which will help to maintain the mechanical strength of the coconut husk.

### **4.2.3. Material characterizations**

The cleaned coconut husk was cut into pieces, followed by grinding to get the virgin coconut husk for characterization. The sample was collected by scratching the flamed surfaces of the FCH evaporators. The sample's structure and morphology were characterized by FESEM (Jeol JSM 7900F). The porosity and the samples' surface area were measured using the BET (Autosorb -IQ-XR-XR-AG) adsorption method. The chemical compositions of the sample were estimated by XPS (Nexsa-ThermoFisher) and FTIR (Nicolet IS50 - Thermo scientific). The optical reflectance of the FCH was directly measured by a UV-vis-NIR spectrophotometer (Agilent-Cary series) attached to an integrated sphere.

### **4.2.4. SSG measurements**

The FCH steam generator was put on Polystyrene foam with a small hole in it through which water was supplied to the evaporator by using a cotton thread. Between the evaporator and the foam, an air-laid paper with the same area as that of the evaporator's bottom was placed to ensure a homogeneous water supply. Before starting the experiment, the ISSG was placed on the container with thread soaking in water and kept overnight for complete water filling of the coconut husk's pores till the top of the evaporator. The evaporator was placed under a Xenon light source (66921, Newport Corporation) which was turned on when the water reached its top. Once the light fell on the evaporator, the mass change profile was measured by an analytical balance (ME204, Mettler Toledo). The intensity of light was adjusted at 1 sun by calibrating with a thermopile sensor (919P-003-10, Newport Corporation) connected to a light meter (843-R, Newport Corporation). Due to the non-uniform distribution of light, the solar flux of different locations over the desired area was averaged to reduce the error. The infrared camera (FLIR E75) connected to a computer was used to record the temperature profile of the system. The area was measured at the maximum circumference of the cylindrical evaporator. All the experiments were conducted at an ambient temperature of  $\sim 23$  °C and relative humidity of  $\sim 48\%$ .

### 4.3. Results and discussion

The chemical composition and functional groups of the RCH and FCH were determined using FTIR spectroscopy, and the results are shown in Figure 4.2a. The peaks in RCH at  $3258\text{ cm}^{-1}$  (O-H stretching vibration) and  $1027\text{ cm}^{-1}$  (O-H bending vibration) are absent in the FCH, which confirms the degradation of the oxygen-containing groups coming from the hydroxyl groups.<sup>[20]</sup> The diminished peak at  $2897\text{ cm}^{-1}$  indicates the formation of unsaturated carbon-carbon bonding, which is one of the reasons for enhancing light absorption.<sup>[20]</sup> XPS analysis was performed to determine the type of chemical bonding present between the elements in FCH. An increase in the carbon concentration was estimated by the carbon to oxygen (C/O)

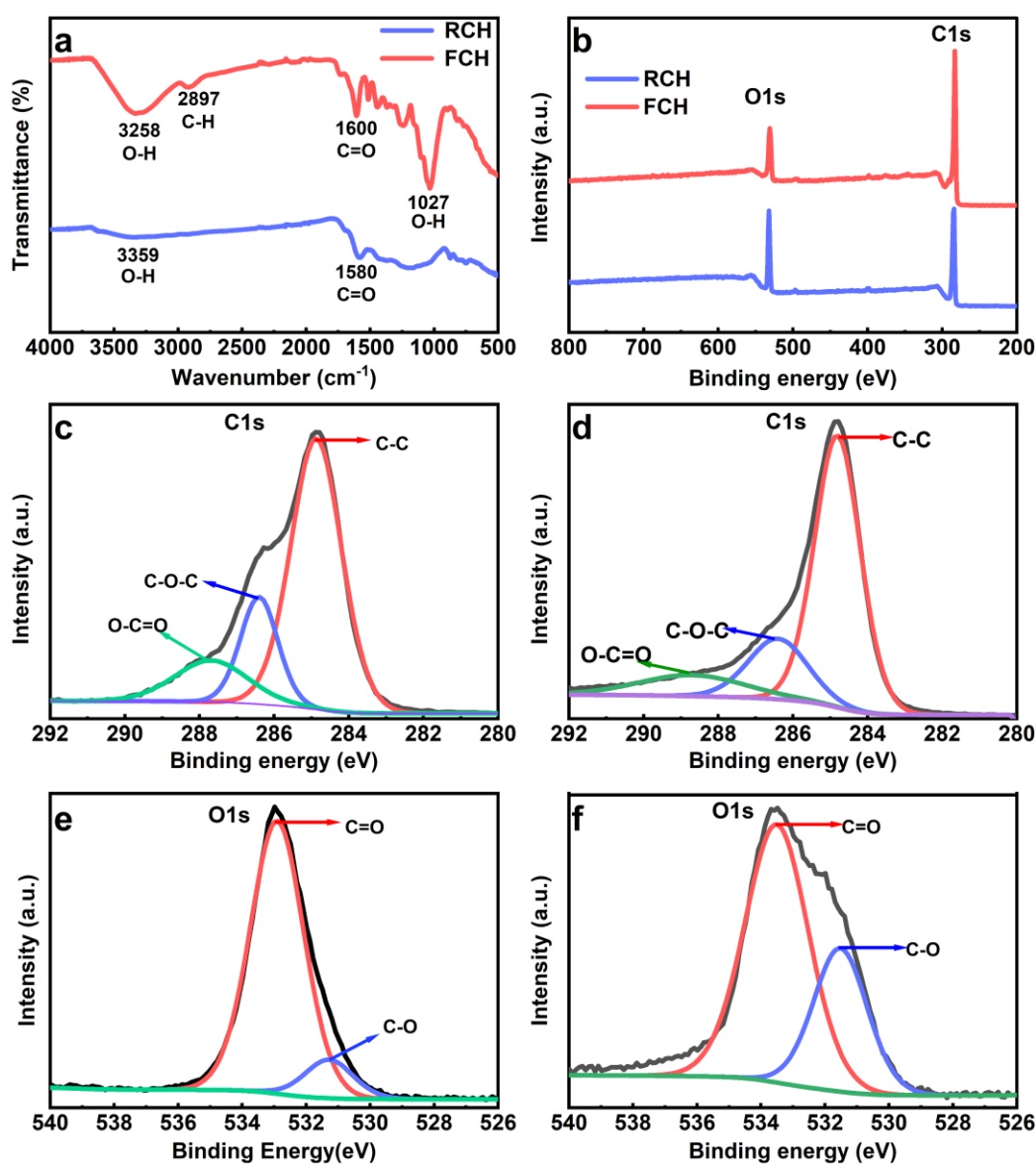


**Figure 4.2.** (a) FTIR and (b) XPS survey spectra of FCH and RCH. High-resolution XPS spectra of (c) C1s orbitals of RCH, (d) C1s orbitals of FCH, (e) O1s orbitals of RCH and (f) O1s orbitals of FCH

ratio from the XPS spectra given in Figure 4.2b. The measured element content of C and O in RCH is 73.27% and 21.11%, and in the FCH, the content of C and O is 82.27% and 14.71%, showing the C/O ratio was increased from 3.47 to 5.59 after flaming. Further, the fitted high-resolution C1s spectra of RCH (Figure 4.2c) and FCH (Figure 4.2d) show three standard peaks of C-C, C-O-C, and O-C=O located around the binding energies 284.8, 286, and 288.7eV and the deconvoluted O1s spectra of coconut husk (Figure 4.2e) and FCH (Figure 4.2f) consist of two distinct peaks of C=O and C-O at binding energies 533 and 531.5eV, respectively. The occurrence of the bonds between carbon and oxygen in the O1s and C1s spectra suggested the hydrophilic nature of the FCH.<sup>[21]</sup> Furthermore, the water droplets were immediately absorbed when added on top of the evaporator, confirming the hydrophilicity of the device.

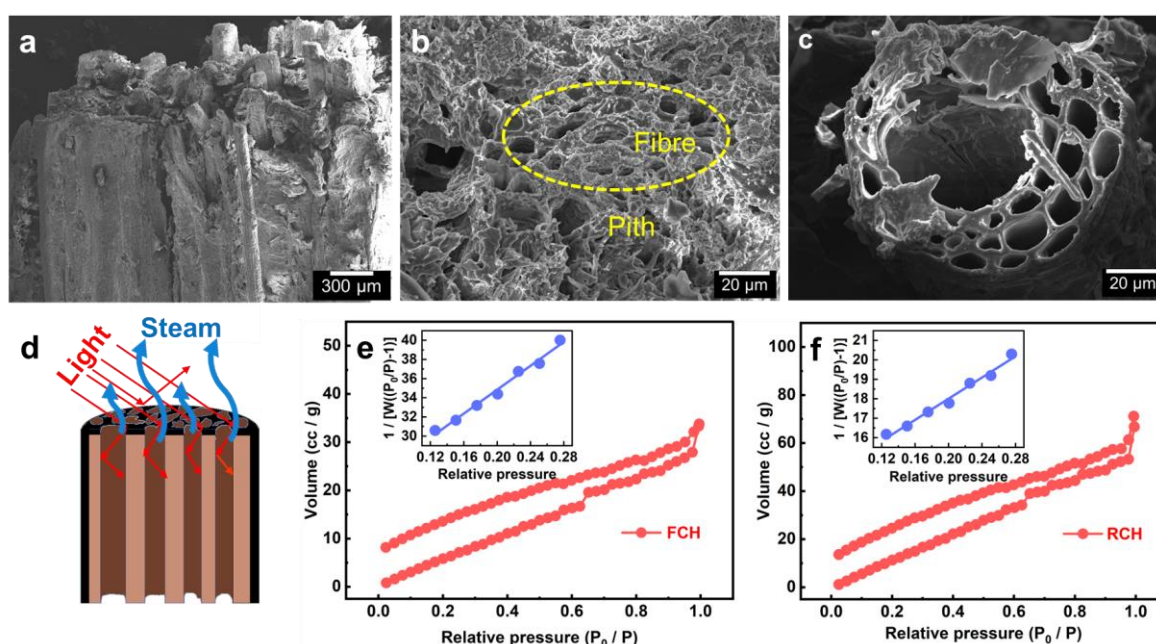


**Figure 4.3.** SEM images of the FCH evaporator (a) side view and (b) top view. (c) SEM image of the top of a single fibre. (d) Schematic diagram showing the advantage of coconut coir in light absorption and steam escape.  $N_2$ -adsorption/desorption isotherms of (e) RCH and (f) FCH. The insets show their respective multipoint BET curves.

The coconut husk consists of fibres bonded by spongy coconut pith. The same structure was maintained after flaming, as shown in the SEM images given in Figure 4.3a-b. The encircled region of Figure 4.3b displays a fibre surrounded by the coconut pith. Furthermore, the tubular fibres with long channels (Figure 4.3c) help in fast water transport. The porous structure of the FCH will enhance solar absorption by trapping the incident photons, increase the effective surface area of evaporation, and act as the escape path to the vapor from the evaporator, as shown in the model in Figure 4.3d. The porous nature of coconut husk was quantified by measuring the surface area before (Figure 4.3e) and after (Figure 4.3f) flaming

using the BET method, and the estimated surface area of RCH and FCH was 87.54 and 41.084  $\text{m}^2 \text{g}^{-1}$ , respectively. The shrinkage of coconut husk may cause a reduced surface area of FCH after flaming.<sup>[8,14]</sup>

The diffused reflectance of the cylindrical FCH evaporator was measured in both dry and wet states in the wavelength range of 300-2500 nm (Figure 4.4a) to estimate the light-absorbing capability. Since the transmittance is zero, the FCH exhibits an average absorption of about 96% and 97.5% (using equation (2.4)) in dry and wet states, respectively, indicating the superior light-absorbing ability of FCH after flaming. On the contrary, 52% of solar absorption of RCH in the dry state (inset of Figure 4.4a) shows its non-suitability for SSG. The high absorption is accredited to the inherent light-absorbing property and porous nature of FCH. The heat harvesting capability of the FCH evaporator from the surrounding was observed by the transient temperature response in the dark. Figure 4.4b shows the variation of temperature of the top of the cylindrical FCH evaporator and its surroundings after it was in

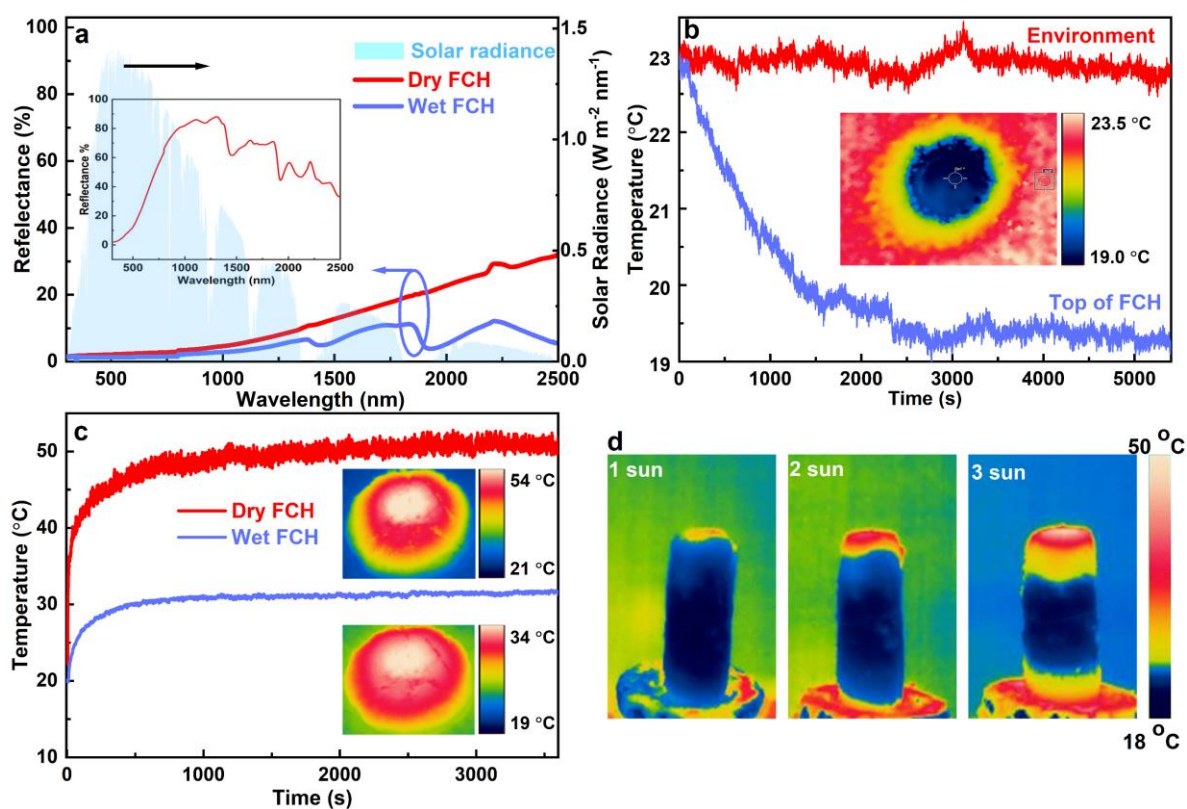


**Figure 4.4.** (a) Diffused reflectance spectra of dry and wet FCH. The solar irradiation spectrum is shown in a light blue area. The inset shows the diffused reflectance of the RCH. (b) Transient response of environmental temperature and top surface temperature after keeping the 2D evaporator in contact with water in the dark. The thermal image in the inset shows the spatial distribution of temperature after saturation. (c) Time course of the surface temperature of dry and wet FCH under 1 sun and insets are IR thermal images of FCH in dry and wet states after 1 h of illumination. (d) IR thermal images of 3D FCH evaporator after 1 h of light illumination under 1, 2 and 3 sun.

contact with water. The surrounding temperature away from the evaporator was approximately constant at  $\sim 23$  °C (neglecting the minimal fluctuations) throughout the measurement time. In contrast, the temperature of the surface of the evaporator slowly decreased to  $\sim 19$  °C after about 45 minutes, followed by saturation. The inset of Figure 4.4b shows the spatial distribution of temperature after saturation. The gradual decrease in the temperature towards the evaporator is due to the evaporative cooling,<sup>[22]</sup> indicating constant heat energy captured by FCH from the surroundings to vaporize water.

Furthermore, under the light illumination of 1 sun intensity, the temperature of the top surface of the evaporator was recorded using an infrared camera to investigate the photothermal effect. In the wet condition, the average temperature increased from  $\sim 19$  °C to  $\sim 31$  °C (Figure 4.4c and the insets), whereas, in the dry state, the temperature reaches from  $\sim 23$  °C to  $\sim 50$  °C, suggesting the efficient light to heat conversion of FCH-based evaporator. Under light illumination of higher intensities, the temperature of the top surface of the cylindrical evaporator increases without affecting the middle parts, where the temperature always remains lower than the ambient temperature (Figure 4.4d). The lower temperature of the lateral surfaces helps in heat harvesting from the environment, leading to an enhanced evaporation performance. These results also show the high thermal insulation property of the FCH-based evaporators, which is beneficial for controlling the conduction losses.

Motivated by these favorable characteristics, the FCH was employed to check its potential for SSG in ambient conditions for 2D and 3D shapes. First, the FCH evaporator's height was optimized by measuring the ER with varying heights under 1 sun illumination, and their performances are given in Figure 4.5a. FCH provides the best performance at the height of around 6 cm. This also shows the advantage of the porous nature of the coconut husk that maintains controlled water flow up to a vertical height of over 6 cm with the help of capillary action. The evaporation performances of the 2D ( $\sim 1$  cm height) and 3D FCH (6 cm height) evaporators under dark and 1 sun illumination conditions are plotted in Figure 4.5b. Under dark, it shows an ER of 0.4 and 1.3  $\text{kg m}^{-2} \text{h}^{-1}$  for 2D and 3D configurations, respectively, which are much faster than pure water (0.09  $\text{kg m}^{-2} \text{h}^{-1}$ ). Under 1 sun illumination, the ER of the 2D evaporator was 2.2  $\text{kg m}^{-2} \text{h}^{-1}$ , and the 3D evaporator showed an average ER of  $3.5 \pm 0.15$   $\text{kg m}^{-2} \text{h}^{-1}$  with a maximum value of 3.6  $\text{kg m}^{-2} \text{h}^{-1}$ , which is comparable to the recently reported other 3D ISSGs (Table 4.1). The 3D ER under 2 and 3 sun was 5.6  $\text{kg m}^{-2} \text{h}^{-1}$  and 7.7  $\text{kg m}^{-2} \text{h}^{-1}$ , respectively, indicating the ER increases linearly with intensity (Figure 4.5c). Under higher solar irradiance power densities, the durability of FCH-based ISSG was estimated. The 3D FCH-based evaporator shows stable performance for more than 15 cycles,

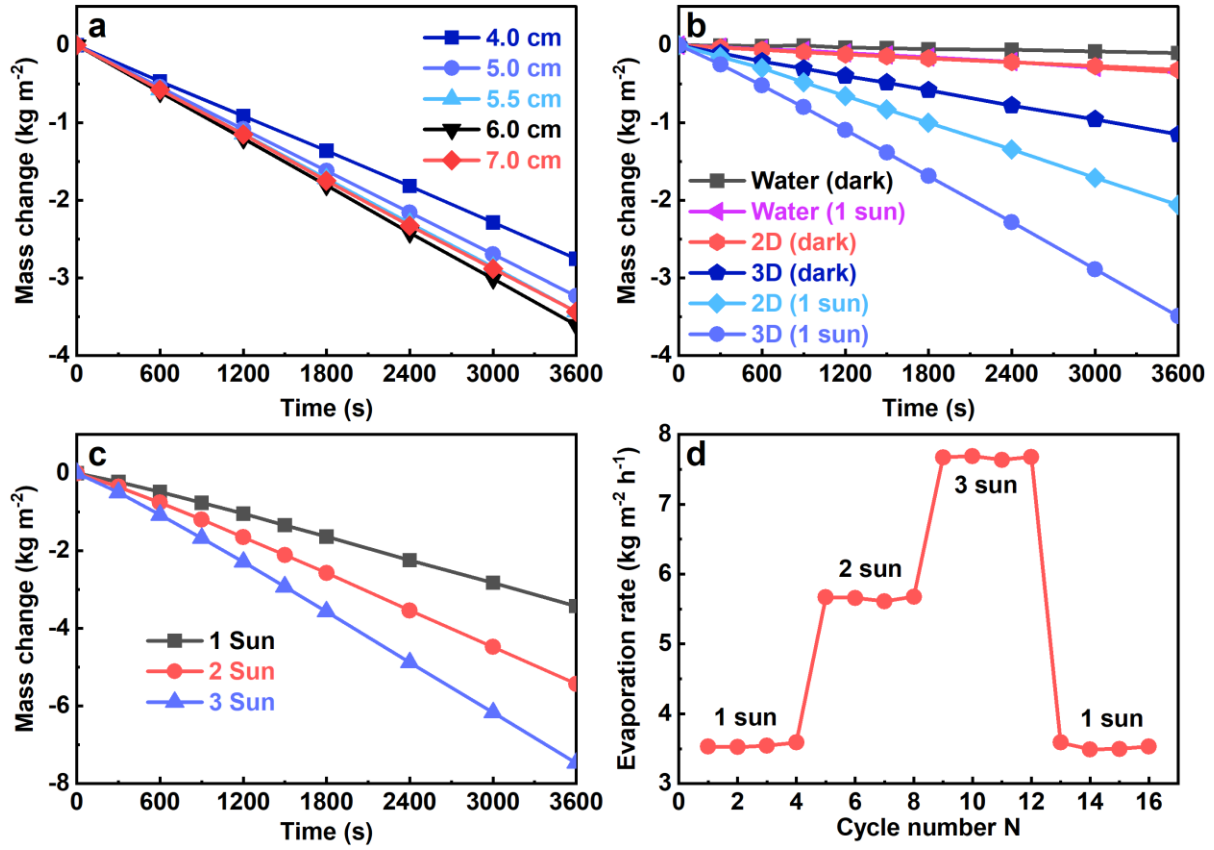


**Figure 4.5.** Mass change of (a) FCH evaporator with different heights under 1 sun illumination and (b) 2D and 3D FCH evaporators in the dark and 1 sun illumination. (c) Mass change of 3D FCH evaporator at higher intensities. (d) ER versus cycle number at a series of solar power intensities.

each cycle of 2 h, confirming its good recycling stability (Figure 4.5d). The estimated evaporation efficiency for 3D FCH using equation (2.1) was 144.4% under 1 sun illumination.

The efficiency of more than 100% was due to the energy gained by the evaporator that was not incorporated into the equation. The heat exchange with the environment was estimated under 1 sun illumination to determine the total energy gained and lost by the 3D evaporator (height = 6 cm and radius = 1 cm) to the environment, and the evaporation efficiency ( $\eta$ ) was calculated by following equation<sup>[23,24]</sup>

$$\eta = \frac{Q_{solar} + Q_{gain} - Q_{loss}}{Q_{solar} + Q_{gain}} \quad (4.1)$$

where,  $Q_{solar}$ ,  $Q_{gain}$ , and  $Q_{loss}$  are the energy of solar flux of 1 sun, energy gained from the environment by the evaporator, and energy loss by the evaporator to the environment, respectively, and are given as follows:

$$Q_{solar} = S_{top} q_{solar} \quad (4.2)$$

$$Q_{gain} = S_{cur} \epsilon \sigma (T_{amb}^4 - T_1^4) + S_{cur} h (T_{amb} - T_1) \quad (4.3)$$

$$Q_{loss} = S_{top}Rq_{solar} + S_{top}\epsilon\sigma(T_2^4 - T_{amb}^4) + S_{top}h(T_2 - T_{amb}) \quad (4.4)$$

where  $S_{top}$  is the projection area of the evaporator,  $q_{solar}$  is the solar flux ( $1000 \text{ W m}^{-2}$ ),  $S_{cur}$  is the curved surface area of the evaporator,  $\epsilon$  is the emittance of the surface,  $\sigma$  is the Stefan-Boltzmann constant,  $T_{amb}$  is the temperature of the environment,  $T_1$  is the temperature of the

**Table 4.1.** Comparison of ER of the 3D-FCH evaporator with recently reported 3D evaporators at 1 sun solar intensity.

| Materials/evaporator   | ER<br>( $\text{kg m}^{-2} \text{ h}^{-1}$ ) | Ref.             |
|--|---|------------------|
| <b>3D cylindrical FCH</b>  | <b>3.6</b>                                  | <b>This work</b> |
| Cup structure using semiconductor NPs                                | 2.04  | [25]             |
| Tree-shaped PPy coated paper (leaf-shaped)                           | 2.3   | [26]             |
| PPy-coated setaria viridis spike composites                          | 3.72  | [27]             |
| Nickle-cobalt@ polydopamine sponges                                  | 2.42  | [28]             |
| Vertically aligned activated carbon Juncus effusus                   | 2.23  | [29]             |
| Activated carbon-cotton fabric                                       | 1.95  | [30]             |
| Nanodiamonds paint filter paper                                      | 1.32  | [31]             |
| Ten-stage thermally-localized multistage solar still prototype       | 5.78  | [32]             |
| PPy decorated maize straws   | 3.0   | [33]             |
| rGO-bamboo paper   | 2.94  | [34]             |
| Carbonized carrot  | 2.04  | [5]              |
| Carbon dot @cellulose paper  | 2.93  | [35]             |
| Ag-polydopamine core-shell structured NPs decorated on wooden flower | 2.08  | [36]             |
| rGO-agrose-cotton aerogel  | 4.0   | [37]             |
| Black nylon fibers @ planar polyvinyl chloride                       | 2.09  | [38]             |
| Carbonized sunflower heads   | 1.51  | [39]             |
| Carbonized bamboo  | 3.13  | [14]             |
| 3D printed cone based on carbon nanotube                             | 2.63  | [40]             |
| 3D spiral structure  | 4.35  | [41]             |
| Carbonized mushroom  | 1.48  | [8]              |

top surface of the evaporator,  $h$  is the heat transfer coefficient ( $10 \text{ W m}^{-2} \text{ K}^{-1}$ ),  $R$  is the reflectivity of the evaporator, and  $T_2$  is the temperature of the curved surface of the evaporator.

The illuminated area of the evaporator was  $3.14 \text{ cm}^2$ , so the total input energy from 1 sun ( $1000 \text{ kW m}^{-2}$ ) is  $0.314 \text{ W}$ . The three terms in equation (4.4) correspond to the reflective, radiative, and convective heat losses. Under light illumination, the top surface's average temperature ( $T_2$ ) was  $\sim 31 \text{ }^\circ\text{C}$  compared with the  $\sim 23 \text{ }^\circ\text{C}$  ( $T_{\text{amb}}$ ) of the surrounding atmosphere; hence, the convective and the radiative heat losses to the environment by FCH were  $0.0266 \text{ W}$  and  $0.0149 \text{ W}$ , respectively. The reflective loss was calculated as  $0.0075 \text{ W}$  (2.4% of  $0.3141 \text{ W}$ , estimated from Figure 4.4a). The heat loss to the underlying water was neglected as the height of the FCH is too high for heat conduction. Therefore, the total energy loss to the

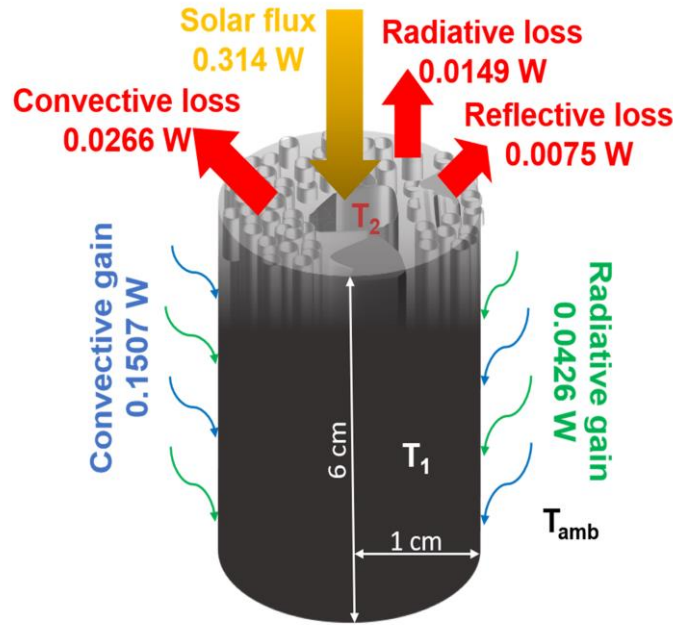


**Figure 4.6.** Schematic diagram of the 3D FCH evaporator with radius 1 cm and length 6 cm showing the heat exchange with the environment.

environment was  $0.0490 \text{ W}$ . Similarly, the convective and radiative energy gain by cold cylindrical surfaces (with temperature  $T_1$ ) of 3D FCH from the ambient environment was calculated as  $0.1507$  and  $0.0426 \text{ W}$ , respectively.

Therefore, under the illumination of 1 sun, for an FCH-based evaporator, the total effective energy input = solar flux + convective gain + radiative gain =  $0.5073 \text{ W}$  ( $\sim 1.6 \text{ kW/m}^2$ ), which is 1.6 times the solar radiation reaching earth's surface (Figure 4.6). Since the input energy supplied to the FCH evaporator was only  $Q_{\text{solar}}$ , the effective energy efficiency goes to 145.9% ( $\{0.314 + 0.1933 - 0.0490\} / 0.314$ ), by considering only  $Q_{\text{solar}}$  in the denominator of the above equation (4.1), which was close to the value calculated above. When

the total energy ( $0.314 + 0.1933$ ) is used in the denominator, the evaporation efficiency reaches down to 90.3%, which was also same as the value of 90.2% calculated from equation (2.1) considering effective  $P_{in}$  as 1.6 sun.

To demonstrate the practical water purification, MB solution, soap water, and detergent water were selected to simulate wastewater using a handmade prototype purification setup (Figure 4.7a). The absorption spectrum was used to examine the concentration of the pollutants. The purification of MB solution is evident from the complete disappearance of the intense characteristic absorption peak in the absorption spectra after purification (Figure 4.7b). The FCH evaporators also efficiently rejected the contaminants in soap and detergent water after the purification, as confirmed by the zero-light absorption shown in Figure 4.7c. The color

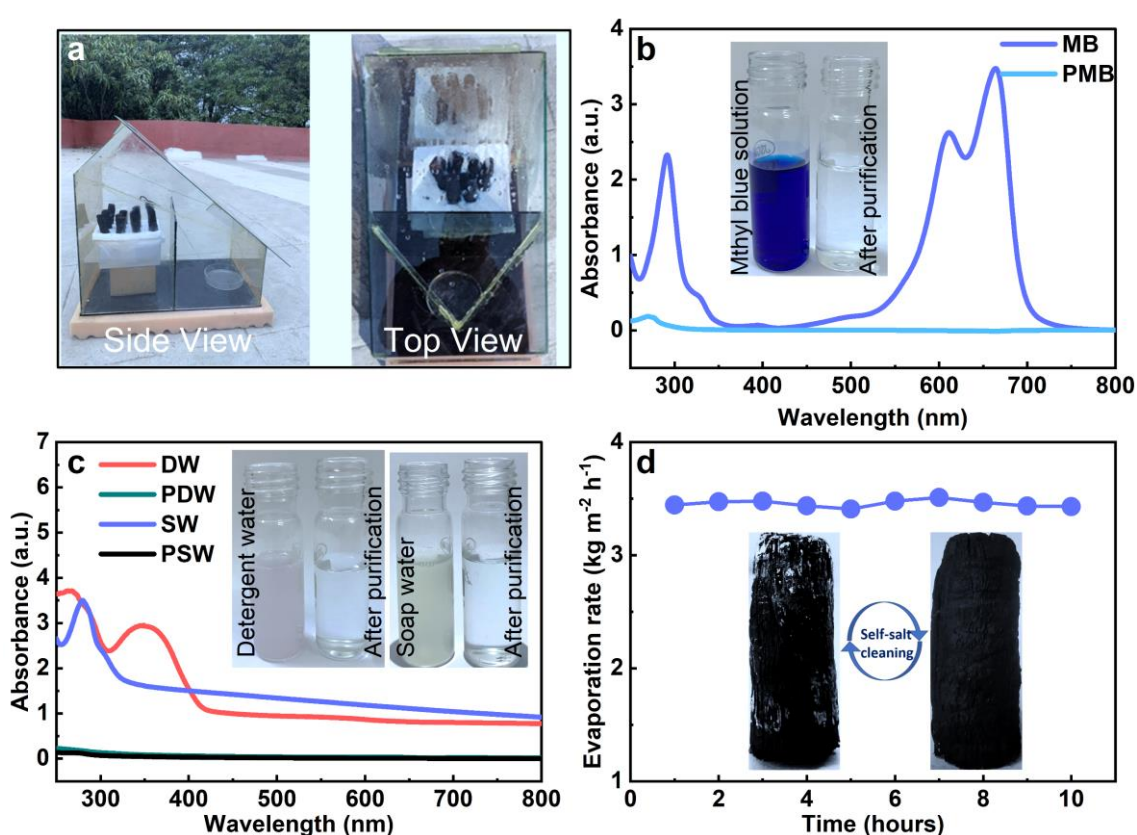


**Figure 4.7.** (a) Photograph for the side view (left) and top view (right) of the prototype of FCH based SSG system. UV-vis spectrum of (b) MB solution, (c) detergent and soap water before and after purification. The respective insets show the photographs of the solutions before and after purification. (d) Retention of 3D FCH evaporator for saltwater for a duration of 10 h. The insets are the optical image of accumulated salt on 3D FCH evaporator's surface after 10 h under high solar intensity (left) and self-cleaned FCH under dark for another 10 h (right).

changes shown in the insets Figure 4.7b, c also demonstrates the FCH evaporator's purification ability. To further evaluate the desalination effect, artificial seawater was prepared by

dissolving 3.5 wt% NaCl in water. The stability of seawater purification was measured by continuously measuring the ER for 10 hours under 1 sun illumination. A nearly uniform ER in Figure 4.7d shows the retention ability of the FCH evaporator without any salt accumulation on the evaporator surface. The qualities of the purified water from all these solutions were further tested by measuring the pH and conductivity. The pH and conductivity values of water after purification from different contaminated solutions were found to be comparable with that of RO and DI water (Table 4.2), indicating that FCH evaporators can effectively decontaminate sewage. It is noteworthy that during high-intensity illumination (more than 3 sun), the salt crystals slowly accumulate on the evaporator's surface after 10 hours of continuous operation. However, in the dark, these accumulated salt crystals dissolve back into the bulk water (inset of Figure 4.7d), ensuring the endurance of the FCH evaporator in seawater desalination.

**Table 4.2.** Conductivity and pH values of different contaminated solutions before and after purification compared with that of DI and RO water.

| S.No. | Type of solution   | Conductivity (mS/cm) |        | pH value |       |
|-------|--------------------|----------------------|--------|----------|-------|
|       |                    | Before               | After  | Before   | After |
| 1     | Saltwater          | 197.20               | 0.079  | 8.881    | 7.563 |
| 2     | MB                 | 21.30                | 0.0071 | 1.575    | 7.399 |
| 3     | Soap solution      | 1.80                 | 0.107  | 12.00    | 7.749 |
| 4     | Detergent solution | 69.00                | 0.2110 | 10.405   | 7.903 |
| 5     | DI water           | 0.00155              |        | 7.23     |       |
| 6     | RO water           | 0.132                |        | 7.69     |       |

## 4.4. Conclusion

In summary, we have demonstrated that coconut husk can be used as an efficient 3D solar vapor generator only by carbonizing its surfaces. 3D structures with increased effective surface area promote energy harvesting from the environment leading to an ER of  $3.6 \text{ kg m}^{-2} \text{ h}^{-1}$  with effective efficiency of 90.2%. The FCH evaporator shows good sustainability towards seawater desalination and sewage purification. Large-scale availability and negligible materials cost combined with simple design techniques of coconut husk-based SSG made it an attractive alternative for freshwater production. Even though the FCH shows efficient evaporation performance in an open atmosphere, there was a remarkable decrease in the actual water CR when used in the closed chamber for practical application. In addition to the low CR, during

seawater desalination, the FCH-based evaporator produces brine by dissolving the salt crystals back into the bulk water, which has detrimental consequences on aquatic ecosystems. Hence, further modifications in terms of materials and design structures are essential to use ISSG at its full potential.

## 4.5. References

- [1] T. Yang, H. Lin, K.-T. Lin, B. Jia, *Sustain. Mater. Technol.* **2020**, *25*, e00182.
- [2] F. Zhao, Y. Guo, X. Zhou, W. Shi, G. Yu, *Nat. Rev. Mater.* **2020**, *5*, 388.
- [3] I. Ibrahim, D. H. Seo, A. M. McDonagh, H. K. Shon, L. Tijning, *Desalination* **2021**, *500*, 114853.
- [4] R. Fillet, V. Nicolas, V. Fierro, A. Celzard, *Sol. Energy Mater. Sol. Cells* **2021**, *219*, 110814.
- [5] Y. Long, S. Huang, H. Yi, J. Chen, J. Wu, Q. Liao, H. Liang, H. Cui, S. Ruan, Y.-J. Zeng, *J. Mater. Chem. A* **2019**, *7*, 26911.
- [6] L. Yang, G. Chen, N. Zhang, Y. Xu, X. Xu, *ACS Sustain. Chem. Eng.* **2019**, *7*, 19311.
- [7] X. Shan, A. Zhao, Y. Lin, Y. Hu, Y. Di, C. Liu, Z. Gan, *Adv. Sustain. Syst.* **2020**, *4*, 1900153.
- [8] N. Xu, X. Hu, W. Xu, X. Li, L. Zhou, S. Zhu, J. Zhu, *Adv. Mater.* **2017**, *29*, 1606762.
- [9] J. Fang, J. Liu, J. Gu, Q. Liu, W. Zhang, H. Su, D. Zhang, *Chem. Mater.* **2018**, *30*, 6217.
- [10] C. Wang, J. Wang, Z. Li, K. Xu, T. Lei, W. Wang, *J. Mater. Chem. A* **2020**, *8*, 9528.
- [11] W. Fang, L. Zhao, X. He, H. Chen, W. Li, X. Zeng, X. Chen, Y. Shen, W. Zhang, *Renew. Energy* **2020**, *151*, 1067.
- [12] C. Xiao, L. Chen, P. Mu, J. Jia, H. Sun, Z. Zhu, W. Liang, A. Li, *ChemistrySelect* **2019**, *4*, 7891.
- [13] J. Li, M. Du, G. Lv, L. Zhou, X. Li, L. Bertoluzzi, C. Liu, S. Zhu, J. Zhu, *Adv. Mater.* **2018**, *30*, 1805159.
- [14] Y. Bian, Q. Du, K. Tang, Y. Shen, L. Hao, D. Zhou, X. Wang, Z. Xu, H. Zhang, L. Zhao, S. Zhu, J. Ye, H. Lu, Y. Yang, R. Zhang, Y. Zheng, S. Gu, *Adv. Mater. Technol.* **2019**, *4*, 1800593.
- [15] E. Taer, *Int. J. Electrochem. Sci.* **2018**, *13*, 12072.
- [16] D. A., S. A. B. A. Manaf, Y. S., C. K., K. N., G. Hegde, *J. Energy Chem.* **2016**, *25*, 880.
- [17] O. O. Olatunde, S. Benjakul, K. Vongkamjan, *Int. J. Food Sci. Technol.* **2019**, *54*, 810.
- [18] S. Panyakaew, S. Fotios, *Energy Build.* **2011**, *43*, 1732.

- [19] R. D. Tolêdo Filho, K. Scrivener, G. L. England, K. Ghavami, *Cem. Concr. Compos.* **2000**, *22*, 127.
- [20] Y. Kuang, C. Chen, S. He, E. M. Hitz, Y. Wang, W. Gan, R. Mi, L. Hu, *Adv. Mater.* **2019**, *31*, 1900498.
- [21] W. Feng, P. He, S. Ding, G. Zhang, M. He, F. Dong, J. Wen, L. Du, M. Liu, *RSC Adv.* **2016**, *6*, 5949.
- [22] X. Li, J. Li, J. Lu, N. Xu, C. Chen, X. Min, B. Zhu, H. Li, L. Zhou, S. Zhu, T. Zhang, J. Zhu, *Joule* **2018**, *2*, 1331.
- [23] Y.-S. Jun, X. Wu, D. Ghim, Q. Jiang, S. Cao, S. Singamaneni, *Acc. Chem. Res.* **2019**, *52*, 1215.
- [24] W. Huang, G. Hu, C. Tian, X. Wang, J. Tu, Y. Cao, K. Zhang, *Sustain. Energy Fuels* **2019**, *3*, 3000.
- [25] Y. Shi, R. Li, Y. Jin, S. Zhuo, L. Shi, J. Chang, S. Hong, K.-C. Ng, P. Wang, *Joule* **2018**, *2*, 1171.
- [26] H. Wang, C. Zhang, Z. Zhang, B. Zhou, J. Shen, A. Du, *Adv. Funct. Mater.* **2020**, *30*, 2005513.
- [27] Z. Xie, J. Zhu, L. Zhang, *ACS Appl. Mater. Interfaces* **2021**, *13*, 9027.
- [28] B. Shao, Y. Wang, X. Wu, Y. Lu, X. Yang, G. Y. Chen, G. Owens, H. Xu, *J. Mater. Chem. A* **2020**, *8*, 11665.
- [29] Q. Zhang, L. Ren, X. Xiao, Y. Chen, L. Xia, G. Zhao, H. Yang, X. Wang, W. Xu, *Carbon N. Y.* **2020**, *156*, 225.
- [30] Q. Zhang, R. Hu, Y. Chen, X. Xiao, G. Zhao, H. Yang, J. Li, W. Xu, X. Wang, *Appl. Energy* **2020**, *276*, 115545.
- [31] L. Zhang, B. Bai, N. Hu, H. Wang, *Appl. Therm. Eng.* **2020**, *171*, 115059.
- [32] Z. Xu, L. Zhang, L. Zhao, B. Li, B. Bhatia, C. Wang, K. L. Wilke, Y. Song, O. Labban, J. H. Lienhard, R. Wang, E. N. Wang, *Energy Environ. Sci.* **2020**, *13*, 830.
- [33] Y. Xu, C. Tang, J. Ma, D. Liu, D. Qi, S. You, F. Cui, Y. Wei, W. Wang, *Environ. Sci. Technol.* **2020**, *54*, 5150.
- [34] Y. Wang, X. Wu, B. Shao, X. Yang, G. Owens, H. Xu, *Sci. Bull.* **2020**, *65*, 1380.
- [35] Z. Wang, W. Tu, Y. Zhao, H. Wang, H. Huang, Y. Liu, M. Shao, B. Yao, Z. Kang, *J. Mater. Chem. A* **2020**, *8*, 14566.
- [36] S. Chen, Z. Sun, W. Xiang, C. Shen, Z. Wang, X. Jia, J. Sun, C.-J. Liu, *Nano Energy* **2020**, *76*, 104998.
- [37] X. Wu, T. Gao, C. Han, J. Xu, G. Owens, H. Xu, *Sci. Bull.* **2019**, *64*, 1625.

- [38] C. Tu, W. Cai, X. Chen, X. Ouyang, H. Zhang, Z. Zhang, *Small* **2019**, *15*, 1902070.
- [39] P. Sun, W. Zhang, I. Zada, Y. Zhang, J. Gu, Q. Liu, H. Su, D. Pantelić, B. Jelenković, D. Zhang, *ACS Appl. Mater. Interfaces* **2020**, *12*, 2171.
- [40] L. Wu, Z. Dong, Z. Cai, T. Ganapathy, N. X. Fang, C. Li, C. Yu, Y. Zhang, Y. Song, *Nat. Commun.* **2020**, *11*, 521.
- [41] Y. Wang, X. Wu, T. Gao, Y. Lu, X. Yang, G. Y. Chen, G. Owens, H. Xu, *Nano Energy* **2021**, *79*, 105477.

# **Chapter 5**

## **Materials and Designs Structures for Efficient Salt Rejection**

Introduction

Experimental section

Results and discussion

Conclusion

References

## 5.1. Introduction

In the previous chapter, we observed that the FCH-based ISSG device shows excellent evaporation performance. But the lack of proper salt separation capacity and steam condensation ability were the major disadvantages. In this chapter, the problem of salt rejection has been addressed through the complete discharge of the salt crystals from the absorber surface using a cone-shaped evaporator and metal oxide as the absorber material.

Metal oxides are promising solar absorber materials for ISSG systems due to their unique features, including environmental stability, bandgap tunability, non-toxicity, and facile low-cost synthesis.<sup>[1,2]</sup> High stability under strong sunlight and elevated temperatures are the primary advantages of oxides over other materials for long-term applications of ISSG. Transition metal oxides are omnipresent in nature and exhibit exotic physical properties and essential applications. Among notable ones, perovskite-structured lanthanum-based complex oxides  $\text{LaMO}_3$  ( $M = \text{Ti, V, Cr, Mn, Fe, Co, and Ni}$ ) are known to have properties like metal-insulator transition, superconductivity, and ferromagnetism.<sup>[3-6]</sup> These materials have recently been used in solid oxide fuel cells, supercapacitors, rechargeable metal-air batteries, solar cells, *etc.*<sup>[7-10]</sup> It has been reported that some of these  $\text{LaMO}_3$  have a narrow bandgap of  $< 0.2$  eV with high absorption coefficient<sup>[11,12]</sup> and hence can be used as a solar absorber in an SSG system that enhances the multifunctionality of lanthanum-based perovskites oxides.

Here, we have prepared a conventional 2D evaporator using Millipore filter paper coated with semiconducting  $\text{LaCoO}_3$  (LCO) and metallic  $\text{LaNiO}_3$  (LNO) nanomaterials as the absorber materials. The narrow bandgap of these materials, combined with high optical absorbance, endows them to absorb solar light over the entire wavelength range of 300–2500 nm. By exploiting this functionality, we achieved a maximum ER of 1.45 and  $1.38 \text{ kg m}^{-2} \text{ h}^{-1}$  in the 2D configuration using LNO and LCO, respectively, corresponding to solar vapor efficiencies of over 80%. To improve the ER further, we have converted our LNO absorber-based 2D evaporator into a cone-shaped 3D structure that shows a water ER of  $2.4 \text{ kg m}^{-2} \text{ h}^{-1}$  under 1 sun illumination leading to solar vapor generation efficiency of 96%. To the best of our knowledge, this ER is the highest of all-metal oxides-based ISSG in such a configuration. The enhancement of the ER in the 3D evaporator is accredited to the lower diffused reflectance, increased surface area, and the additional heat capture from the ambient environment.

Further, for real-world situations, such as high salt concentrations or high solar intensities, we replace the filter paper with a SS sheet to physically separate the evaporation and the light-absorbing surfaces. With such a structure, we achieved long-term evaporation

stability of the device under a salt concentration of 20 wt%. The device also efficiently withstands higher solar intensities, unlike the device using filter paper. These results demonstrate the potential of our device for seawater desalination irrespective of the illumination or the salt concentration conditions, with the additional advantage of salt harvesting.

## 5.2. Experimental section

### 5.2.1. Materials

Lanthanum nitrate hexahydrate (purity 99.9%), nickel nitrate hexahydrate (purity 99.999%), cobalt nitrate hexahydrate (purity  $\geq 98\%$ ), ammonium hydroxide, potassium hydroxide was purchased from Sigma-Aldrich and cellulose filter paper with different pore sizes from Merck Millipore Company. All the chemicals were used without further purification.

### 5.2.2. Preparation of LCO and LNO NPs

The NPs of LCO and LNO were prepared by a simple hydrothermal route following Tepech-Carrillo *et al.*<sup>[13]</sup> and Dong *et al.*,<sup>[14]</sup> respectively, illustrated in Figure 5.1 for LNO NPs. In brief, an alkaline solution was prepared by mixing ammonium hydroxide and DI water, followed by the addition of lanthanum nitrate hexahydrate and cobalt nitrate hexahydrate under continuous stirring. The molar ratio of nitrates was kept at 1:1. Sodium hydroxide as a precipitating agent was dissolved in the mixture to raise the pH to more than 12. Then the solution was placed in a Teflon-lined SS autoclave, sealed, and heated at 220 °C for 48 h. Then the resulting product was washed several times with DI water and ethanol and collected by filtration, followed by drying at 60 °C overnight. The precursor powder was ground and calcinated at 950 °C in the air for 3 h. Finally, the product was ground again to obtain LCO NPs. For LNO, nickel nitrate hexahydrate was the precursor material for Ni, and the pH was



**Figure 5.1.** Schematic illustration of the hydrothermal synthesis of LNO NPs.

maintained using potassium hydroxide. Finally, the product was calcined at 800 °C in the air for 4 h to obtain the NPs of LNO.

### 5.2.3. Preparation of LNO/LCO-based 2D and conical 3D devices

10 mg of LNO/LCO NPs were well dispersed in 20 ml DI water using an ultrasonic bath. The dispersed mixture was deposited on the cellulose filter paper of diameter 4.2 cm by vacuum filtration setup. The coated film was dried at 60 °C in a hot air oven for 20 minutes to get the 2D device. The LNO-coated film was cut and then folded into a 3D conical shape with a diameter of 1.5 cm and an apex angle of 50°, as illustrated in Figure 5.2.

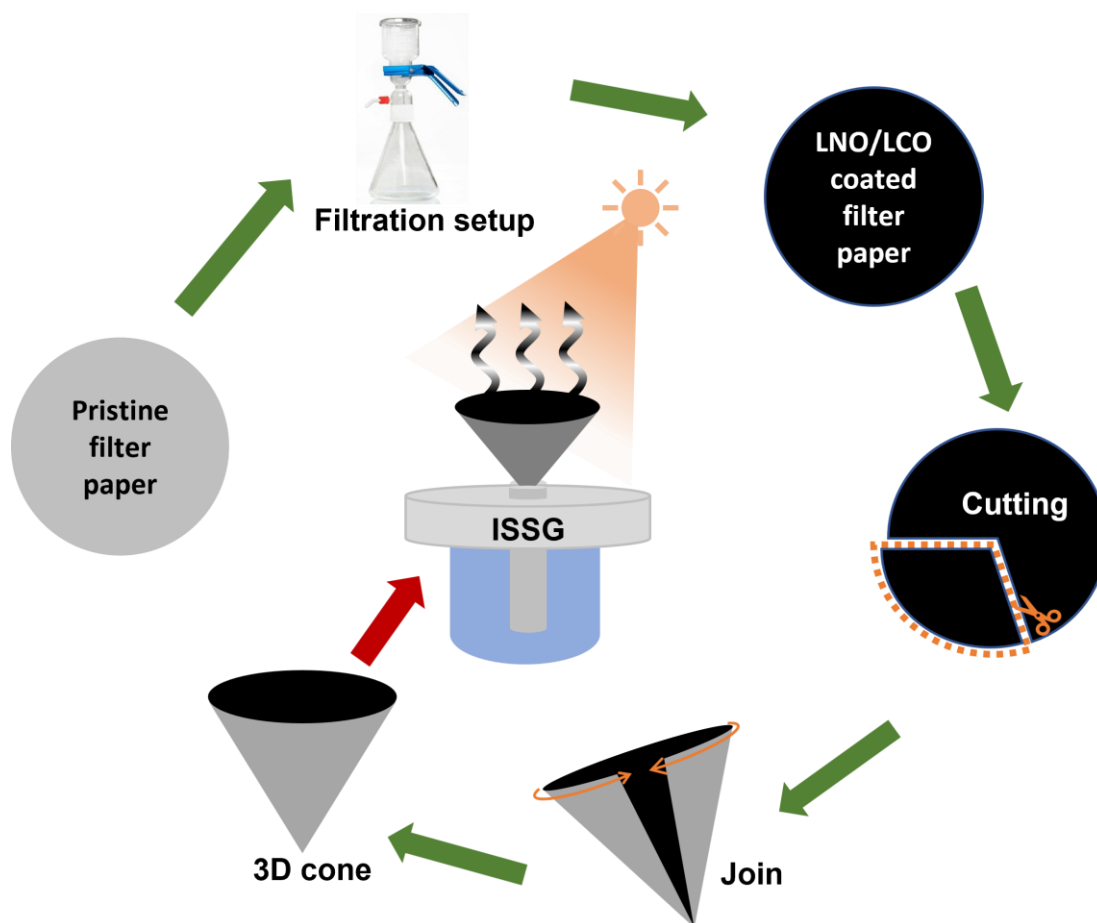


**Figure 5.2.** Schematic illustration of the preparation of 2D and conical 3D devices.

### 5.2.4. Material characterizations

The morphology of the sample was observed by the FESEM (JEOL JSM 7900F) images, and element distribution was detected using EDX spectroscopy (ULTIM MAX- Oxford). The crystalline structure of the samples was characterized using powder XRD (Panalytical Empyrean, Cu K $\alpha$ ,  $\lambda = 1.5406 \text{ \AA}$ ). XPS spectra were obtained using a ThermoFisher Scientific

(Nexsa) instrument with an Al K $\alpha$  X-ray source. The diffused reflectance spectra were measured in the 300-2500 nm range using a UV-vis-NIR spectrophotometer (Cary 5000) with an integrating sphere unit, and the measurements were corrected by baseline/blank correction.

### **5.2.5. SSG measurements**

The SSG performance experiments were conducted using a xenon light source (Newport Corporation, 66921). The intensity of light was adjusted at 1 sun using a thermopile sensor (Newport Corporation, 919P-003-10) connected to a light meter (Newport Corporation, 843-R). The solar flux over the desired area at different locations was averaged to reduce the error caused by the uneven distribution of light. The mass change profile of the steam generator was measured by an analytical balance (Mettler Toledo, ME204) with an accuracy of 0.1 mg. The thermal images and the temperature distribution of the steam generator were obtained by using an infrared camera (FLIR, E75) connected to a computer. All the data were acquired at an ambient temperature of 25 °C and relative humidity of 55%.

## **5.3. Results and discussion**

LCO and LNO belong to the space group of  $R\bar{3}c$ , and their respective perovskite structures are illustrated in Figure 5.3a, b. The crystal structure of our synthesized nanomaterials was characterized using X-ray diffraction spectra and is given in Figure 5.3c. A perfect match with the Joint Committee on Powder Diffraction Standards (JCPDS) data with card numbers JCPDS-00-034-1181 and JCPDS-01-078-3230 confirms the rhombohedral structure of LNO and LCO, respectively. The FESEM images of LCO (Figure 5.3d) and LNO (Figure 5.3e) show a rodlike morphology for both the samples with an average diameter of the order of 55 and 43 nm and an average length of 222 and 150 nm, respectively. EDX spectroscopy and corresponding elemental mapping results (Figure 5.4) reveal that the La, Co, O and La, Ni, O elements are uniformly distributed in the LCO and LNO, respectively.

XPS measurements were performed to probe the surface elements compositions of both LCO and LNO. The presence of only La, Co, Ni, O, and C in the survey spectra of LCO in Figure 5.5a and LNO in Figure 5.5b indicates the high purity of the products. The high-resolution La 3d XPS spectrum for LCO (Figure 5.5c) shows two prominent peaks at 851.28 and 834.4 eV for La 3d<sub>3/2</sub> and La 3d<sub>5/2</sub>, respectively, with the shake-up peaks located at 854.8 and 838.1 eV. Similarly, in the case of LNO, the peaks are at 850.28 and 833.68 eV for 3d<sub>3/2</sub> and La 3d<sub>5/2</sub>, with their corresponding satellite peaks at 854.58 and 837.58 eV in the La 3d XPS spectrum (Figure 5.5d) ensure +3 valence state of La in LCO and LNO.<sup>[15]</sup> The Co 2p XPS

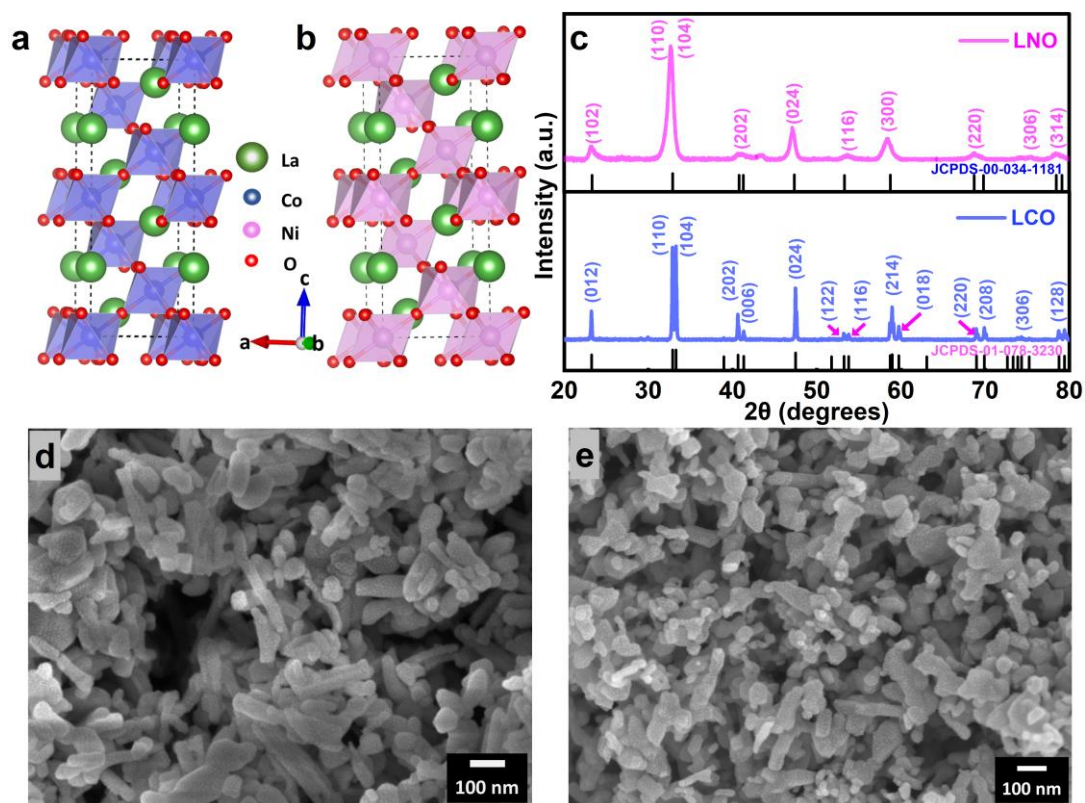


**Figure 5.3.** Crystal structure of rhombohedral (a) LCO and (b) LNO. (c) X-ray diffraction pattern LCO and LNO NPs. FESEM images of (d) LCO and (e) LNO.

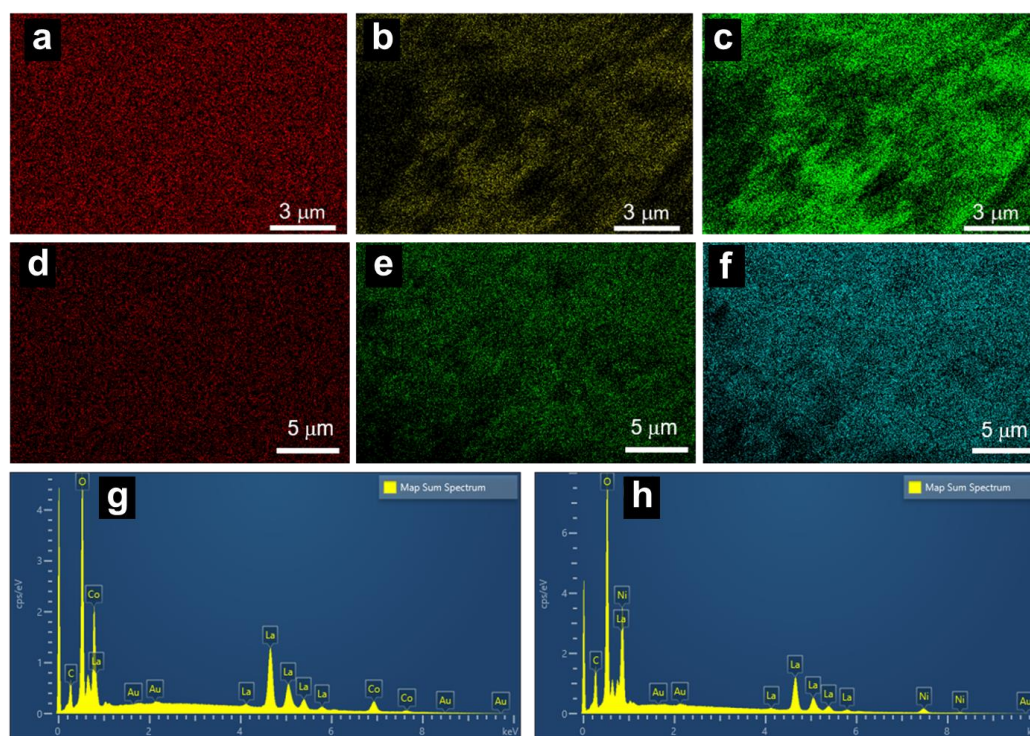


**Figure 5.4.** EDS elemental mapping graphs of (a) La (b) Co (c) O of LCO and (d) La (e) Ni (f) O of LNO. EDS spectrum of (g) LCO and (h) LNO.

spectrum for LCO (Figure 5.5e), shows two prominent peaks corresponding to the Co  $2p_{1/2}$  and Co  $2p_{3/2}$  at 794.78 and 779.58 eV, respectively, which are close to the value reported in the literature.<sup>[16]</sup> These peaks are close to that of  $\text{Co}_2\text{O}_3$  (779.2 eV), confirming the existence of the

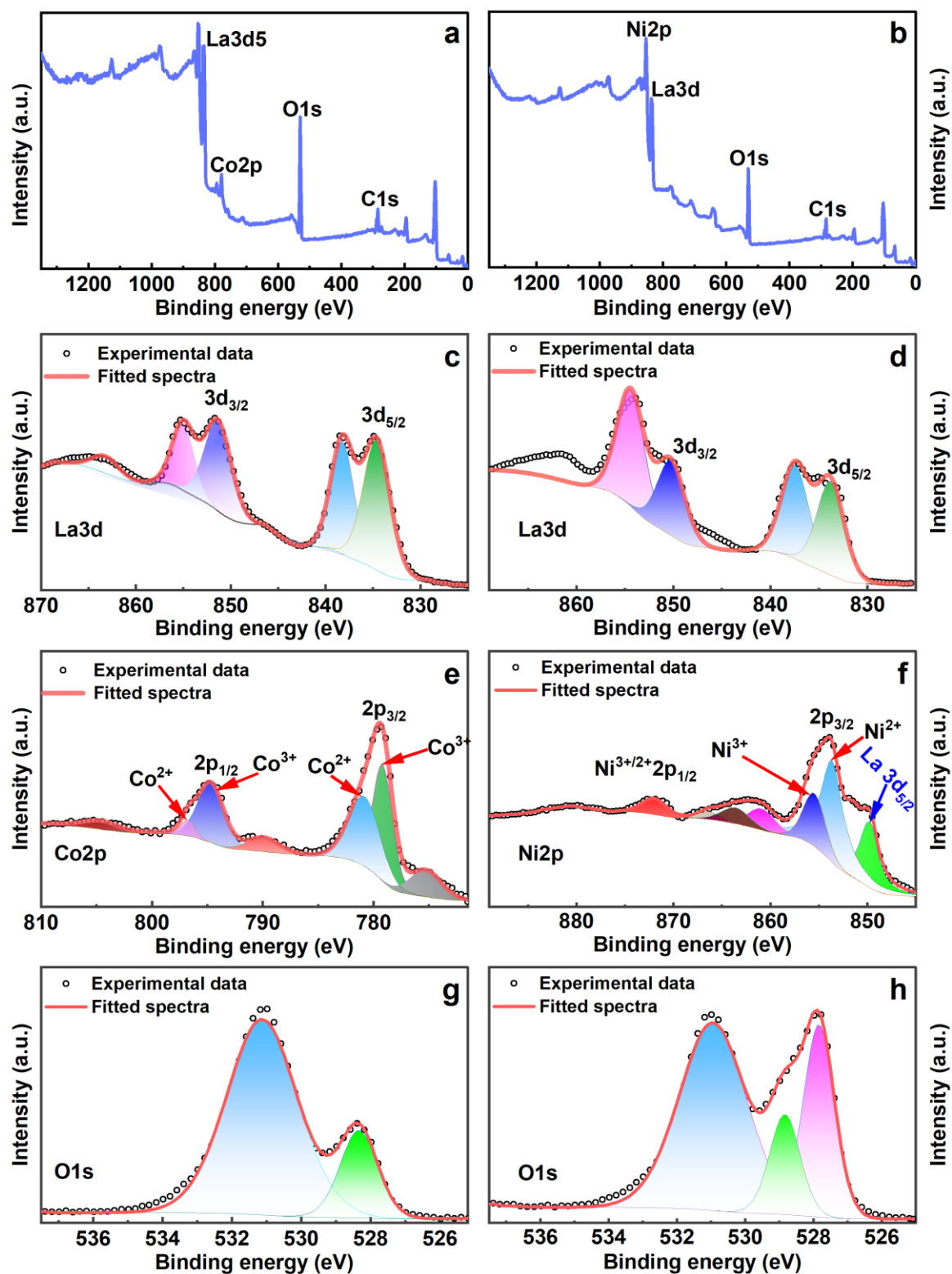


**Figure 5.5.** XPS survey spectra of (a) LCO and (b) LNO. High resolution XPS spectrum of (c) La 3d, (d) Co 2p, (e) O 1s for LCO and (f) La 3d, (g) Ni 2p, (h) O 1s for LNO NPs.

Co<sup>3+</sup> valence state.<sup>[17]</sup> The peaks at BE 872.18 and 855.68 eV in Figure 5.5f are indexed to Ni 2p<sub>1/2</sub>, and Ni 2p<sub>3/2</sub> are characteristic of the Ni<sup>3+</sup> cation.<sup>[18]</sup> The O1s XPS spectra for LCO and LNO show (Figure 5.5g, h) two features at about 531.18 and 530.98 eV corresponding to absorbed oxygen and 528.38 and 528.78 eV to lattice oxygen (oxygen–metal bonds), respectively.<sup>[17]</sup>

Structural relaxation and electronic properties of LMO<sub>3</sub> are investigated by the Vienna ab initio simulation package<sup>[19]</sup> implemented density functional theory (DFT) with plane-wave basis set and projector-augmented wave-type frozen core all-electron potentials.<sup>[20]</sup> The exchange-correlation energy is approximated using the generalized gradient approximation (GGA).<sup>[21]</sup> An equivalent cut-off energy of 400 eV is used for a finite number of plane waves, which gives a nearly accurate equilibrium state of the system. Considering the strong correlation effects in transition metals, the structural relaxations and electronic structure calculations are performed with spin-polarized GGA+U<sup>[22]</sup> calculations throughout the study. The on-site Coulomb term U for Co and Ni was chosen to be 6 eV.<sup>[23]</sup> The k-points are sampled by a 7 × 7 × 7 Monkhorst-Pack k-grid in the first Brillouin zone. Electronic relaxation is maintained up to 10<sup>-6</sup> eV, and the atoms are allowed to relax until the force is less than 0.01 eV/Å. Our DFT+U calculated band structure shows that LCO has a bandgap of 0.47 eV at the Gamma point, and the estimated band gap value is consistent with previous reports.<sup>[24][25]</sup> In the partial density of states (PDOS) plot of LCO, the states near valence band maxima (VBM) and conduction band minima (CBM) are dominated by Co-3d and O-2p (Figure 5.6a), which indicates a strong hybridization between Co-3d and O-2p.

On the other hand, a metal-like behavior was observed for LNO, as given in Figure 5.6b, which is consistent with the previous reports.<sup>[25][26]</sup> Also, the optical absorption in LNO is mainly due to the intra-band and inter-band electron transition,<sup>[27][28]</sup> elaborated in the following discussion. The DFT+U calculated results show LNO behaves like a half-metal with a minority spin bandgap of 2.45 eV. Here optical transitions are possible for both majority and minority spins. In the band structure plot, the majority and minority spins show metallic and semiconducting behavior. First, we discuss the majority of spin optical transitions. The materials are often termed as strongly correlated systems, having transition metal and lanthanides or actinide elements with partially filled d or f-shells. Also, the electrons occupying the open d- or f-shells are highly localized spatially and therefore maintain atomic-like behaviors to a significant extent. So LNO is a strongly correlated metal. Due to the strong Coulomb repulsion and localization of Ni 3d-orbital electrons (conduction electrons), the electrons' effective mass is much higher than in the normal metallic system. According to the

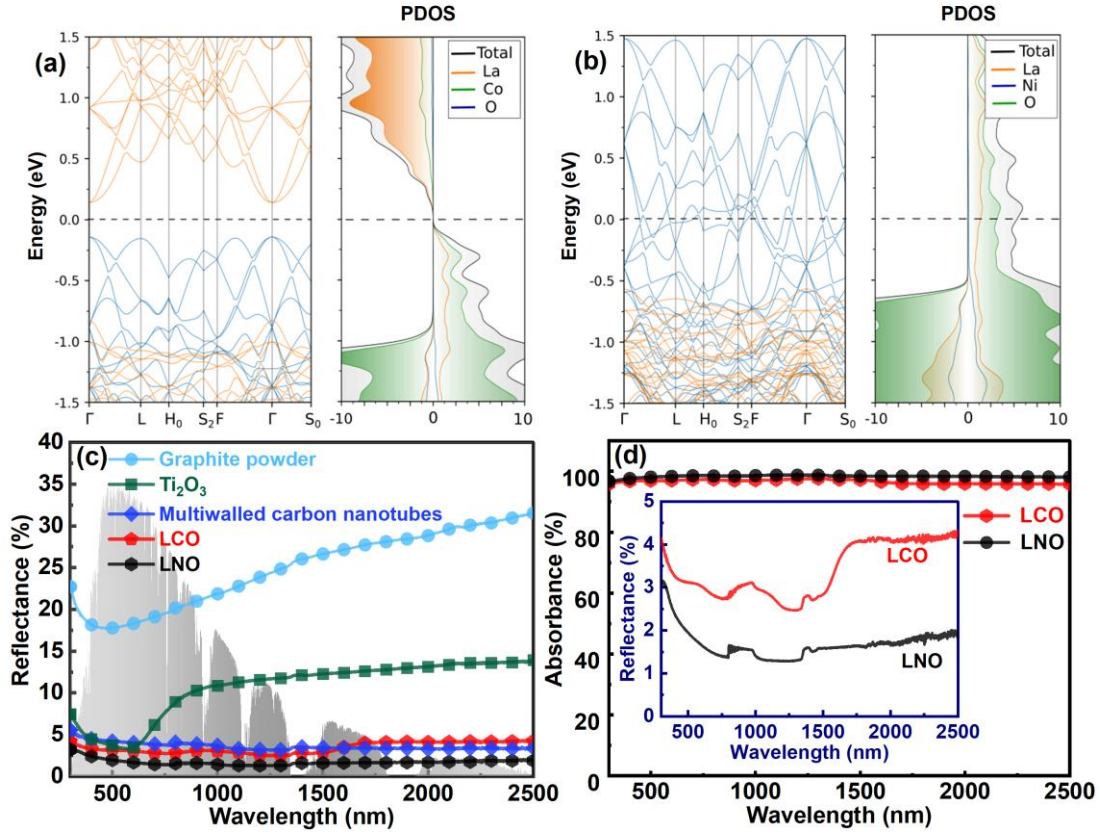


**Figure 5.6.** Band structure and PDOS plot of (a) LCO and (b) LNO, where the Fermi level is set at zero. In the band structure plot, the blue and yellow lines represent the spin-up and spin-down states. (c) Comparison of diffused reflectance spectra of commonly used photothermal materials with LNO and LCO. (d) Absorption spectra of the LCO and LNO. Inset shows the enlarged view of the diffused reflectance spectra for LCO and LNO.

Drude theory, the expression of frequency-dependent optical conductivity is:

$$\sigma(\omega) = \frac{\sigma_0}{1+\omega^2\tau^2} + \frac{i\sigma_0\omega\tau}{1+\omega^2\tau^2} \quad (5.1)$$

where  $\sigma_0 = \frac{ne^2\tau}{m^*}$  is Drude dc conductivity.

In the above expression,  $\omega$  is frequency,  $m^*$  is the effective mass of the charge carriers, and  $\tau$  is the relaxation time of the charge carriers. Here both intraband and interband transitions are possible. For LNO, the well-defined Drude peak at zero shows metallic behavior and originates from electrons' intra-band transitions. Furthermore, the strong correlation effect of La-4f and Ni-3d electrons produces some inter-band transitions in the optical absorption spectra. In the visible range spectrum, the inter-band transitions happen due to two types the electronic excitations, such as: from O-2p to Ni-3d- $e_g^*$ , and Ni-3d- $t_{2g}^*$  to Ni-3d- $e_g^*$ . So, both the interband and intraband transitions increase the optical absorption coefficient of LNO. The optical transitions are very simple for minority spin states in LNO due to a semiconducting

bandgap. The optical band gap of minority spin is 2.45 eV, which is in the visible range spectrum. Here the VBM and CBM minority spin states are dominated by the O 2p- and Ni 3d-orbitals, the same as LCO.

The low bandgap makes  $\text{LaMO}_3$  capable of absorbing solar energy over the full range of the solar spectrum. Standard solar illumination of AM 1.5 contains photons with an average energy of 1.6 eV, which is much higher than the bandgap of  $\text{LaMO}_3$ , leading to the overwhelming generation of above bandgap electron-hole pairs in  $\text{LaMO}_3$  under illumination. The above bandgap electrons and holes then relax to the band edges, converting the extra energy into heat through the thermalization process.<sup>[19,29]</sup> In general, the relaxation dynamics of the above-bandgap electrons and holes are quite complicated, but an acoustic-phonon scattering mechanism may dominate it.<sup>[29]</sup>

The light absorption performance was experimentally evaluated by the UV-vis-NIR diffuse reflectance spectra in the wavelength range of 300 to 2500 nm. The diffuse reflectance of commercial  $\text{Ti}_2\text{O}_3$  powder and some carbon materials were measured for comparison (Figure 5.6c). Since the transmittance was close to zero (because of the high thickness), the only energy

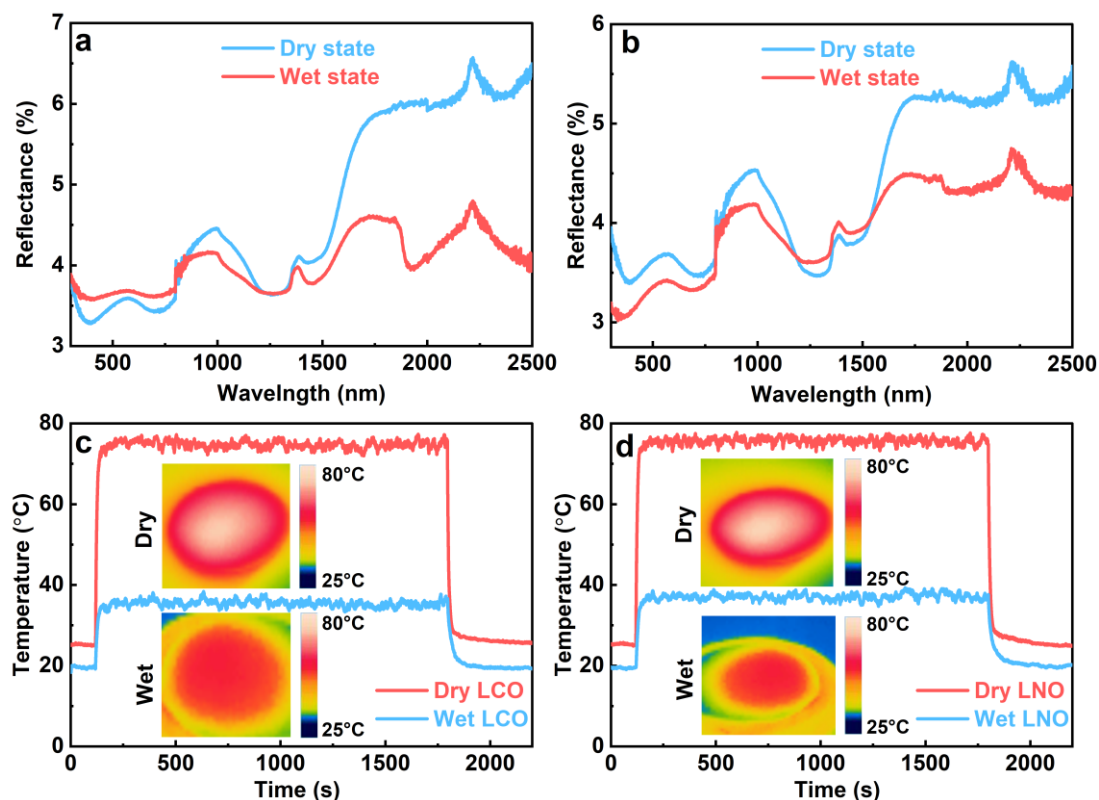


**Figure 5.7.** Diffused reflectance of 2D film shaped sample of (a) LCO and (b) LNO in both dry and wet conditions. Transient surface temperature response of the 2D (c) LNO and (d) LCO in dry and wet states under 1 sun illumination. The insets show the thermal images of the sample after saturation.

loss was due to reflection from the surface of the samples. The percentage of solar absorption calculated using equation (3.4) for graphite powder,  $\text{Ti}_2\text{O}_3$ , and MWCNTs were 77%, 92%, and 96%, respectively, close to the values reported in the literature.<sup>[30][31]</sup> On the other hand, LCO and LNO NPs show solar absorption (Figure 5.6d) of about 97% and 98.5%, respectively, implying a better light absorption capability which is beneficial for solar-thermal applications.

Furthermore, the diffused reflectance spectra of the LCO and LNO-coated on filter paper (commonly called 2D ISSG) were measured in both dry and wet states (Figure 5.7a, b). The diffused reflectance of 2D samples was similar to that of their corresponding powder samples calculated above. To investigate the photothermal effect, the surface temperature of the 2D devices of both LCO and LNO was recorded under 1 sun illumination using an infrared camera. Figure 5.7c, d shows the transient temperature response, and their insets show the thermal images of the 2D evaporators under 1 sun illumination. After illumination, the surface temperatures of dry samples of LCO and LNO increased rapidly and saturated over 75 °C and 76 °C, respectively. While at the wet condition, the saturation temperatures for LCO and LNO were 36 °C and 37 °C, respectively, suggesting a high heat-to-vapor conversion capability.

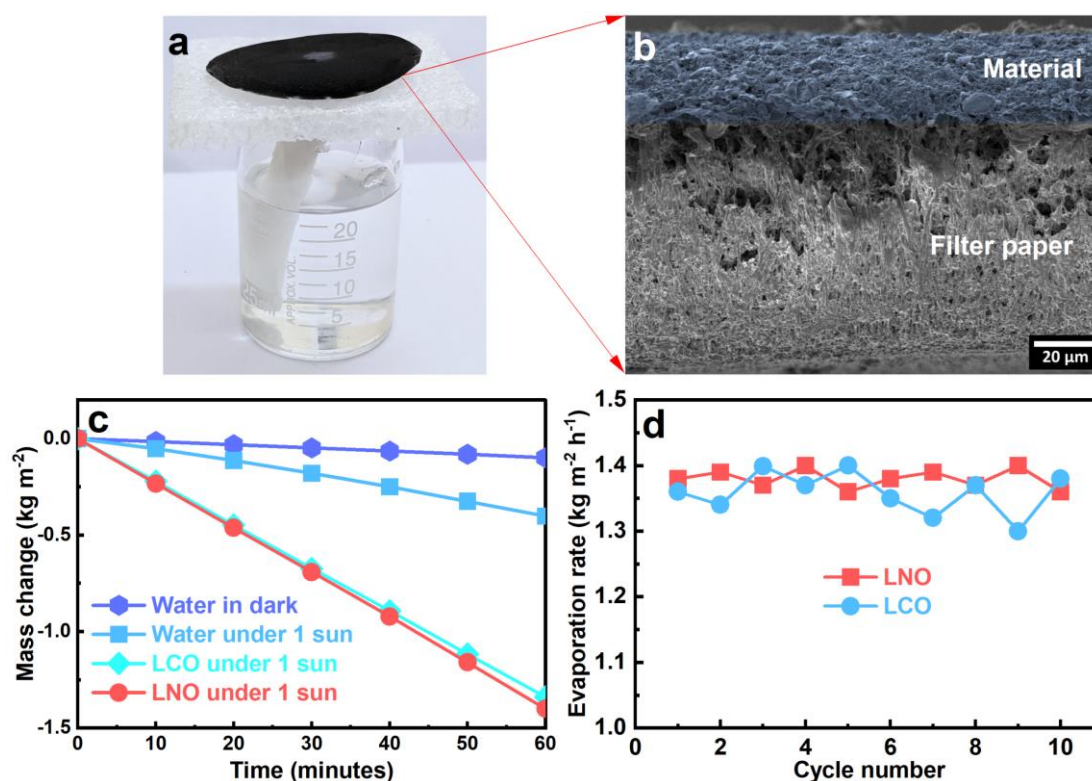


**Figure 5.8.** (a) The conventional setup for 2D ISSG. (b) Cross-sectional FESEM image of absorber-coated filter paper. (c) Mass change of water using LCO and LNO-based evaporators and compared with that of water in the dark and under 1 sun illumination. (d) ER for two evaporators for continuous 10 cycles.

Figure 5.8a shows the conventional setup for ISSG in which a 2D device of 2 cm diameter is placed on the insulating polystyrene foam, and the water is supplied via the tissue paper. The optimized absorber material thickness on the filter paper was around 30  $\mu\text{m}$  as measured by the cross-sectional FESEM image (Figure 5.8b). Subsequently, we estimated their steam generation performance, as shown in Figure 5.8c. Under the dark, a similar ER of  $0.1 \text{ kg m}^{-2} \text{ h}^{-1}$  was calculated for both LCO and LNO-based 2D ISSG. The average ER was  $1.42 \pm 0.2$  and  $1.37 \pm 0.1 \text{ kg m}^{-2} \text{ h}^{-1}$  for LNO and LCO. The maximum ERs of 1.38 and  $1.45 \text{ kg m}^{-2} \text{ h}^{-1}$  were achieved under 1 sun illumination using the LCO and LNO absorbers, respectively, which are much higher than pure water under similar conditions. The ER of both LCO and LNO remains constant during ten experimental cycles, and each cycle of 1 h, shows good recycling stability (Figure 5.8d). The evaporation efficiency of the LCO and LNO was calculated to evaluate their performance as a photothermal material using equation (3.1). The estimated maximum evaporation efficiencies of 2D LCO and LNO were 80% and 85%, respectively, which are comparable to the previously reported complex oxide absorbers.<sup>[32][33]</sup>

In general, for 2D ISSG, some part of the incident energy is missed to the environment through the thermal (including radiation, convection, and conduction losses) and optical losses (including reflection and transmission of light). The conduction loss is negligible as the bulk water temperature remains almost the same throughout the experiment due to a thermal insulation layer. Since the average temperature of both LCO and LNO was almost the same, the radiation and convection losses for both samples were about 6.7% and 5.5%. The reflection loss was estimated from the absorption spectra, and values were 3.6% and 5% for LNO and LCO absorbers, respectively. Therefore, total heat loss was around 16% and 17% leading to an efficiency of over 83%, consistent with the efficiency values calculated above.

To further improve the ER by limiting the losses, we converted the LNO absorber-based 2D ISSG into a conical 3D structure with an apex angle of  $50^\circ$ . As shown in Figure 5.9a, the diffused reflectance of the modified 3D conical structure of LNO in the dry and wet states is significantly lower throughout the entire solar spectrum than that of the 2D devices of LNO and LCO discussed above. A photograph of the typical arrangement for the 3D ISSG is given in the left inset of Figure 5.9a, and the ray diagram in the right inset shows the advantage of a conical structure in achieving nearly 100% light absorption. Using the 3D conical ISSG, the average ER of  $2.3 \pm 0.2 \text{ kg m}^{-2} \text{ h}^{-1}$  under 1 sun illumination was achieved using eight different conical devices, as plotted in Figure 5.9b. The ER is 3.8 times higher than the rate under dark ( $0.6 \text{ kg m}^{-2} \text{ h}^{-1}$ ) and 2.5 times higher than pristine filter paper (without absorber material) ( $0.9 \text{ kg m}^{-2} \text{ h}^{-1}$ ) under 1 sun illumination (Figure 5.9c). To the best of our knowledge, this ER is

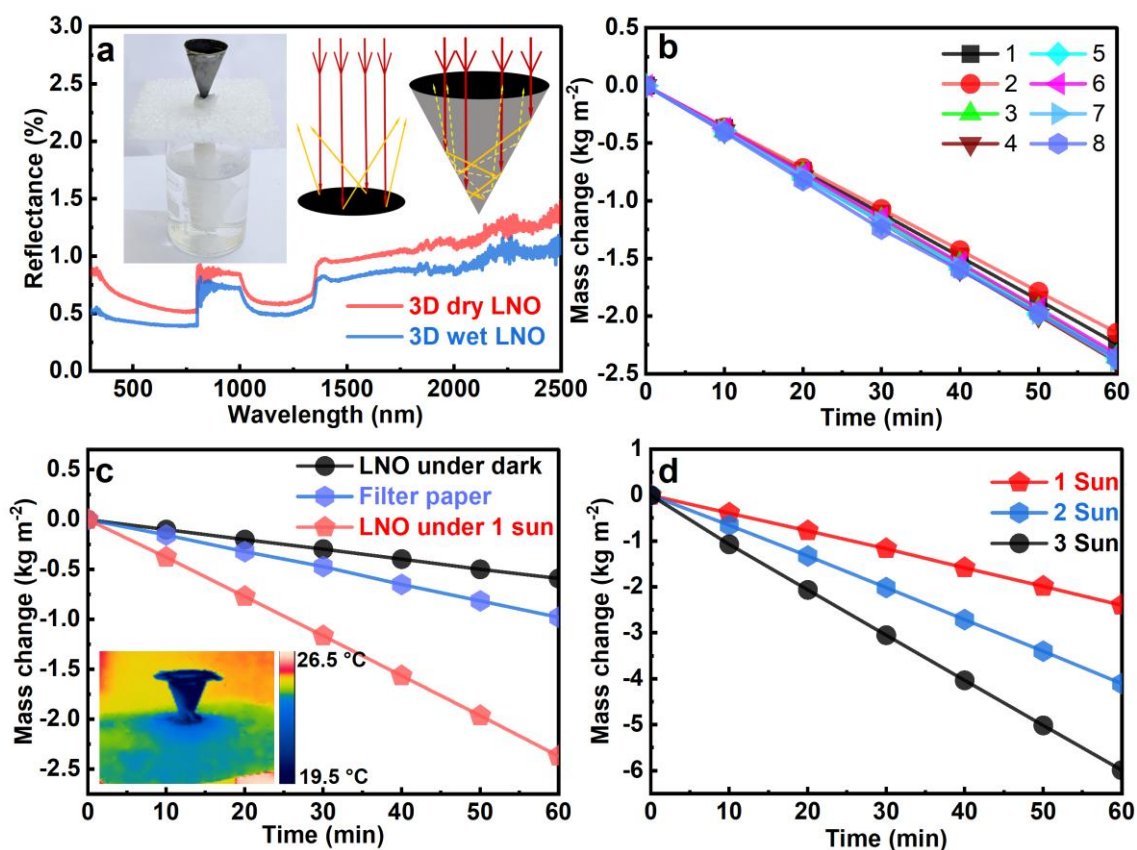


**Figure 5.9.** (a) Diffuse reflectance spectra of dry and wet 3D cone-shaped LNO evaporator. The left inset shows the digital photograph of a typical arrangement for the 3D ISSG. Schematic of 2D (middle) and 3D (right) showing the advantage of 3D conical over 2D ISSG. (b) Mass change profile of eight different 3D ISSG devices using LNO absorber layer to calculate the average ER. (c) Mass change of water using 3D cone-shaped LNO-based evaporators and compared with that of conical pristine filter paper under 1 sun illumination. The insets show the IR thermal images of the cone after saturation. (d) Mass change of water using 3D cone-shaped LNO-based evaporators at different illumination intensities.

the highest of all-metal oxides-based ISSGs in such configuration and is compared with some recent reports in Table 5.1.<sup>[1,2,30,32–42]</sup> The ER of 2.3 kg m<sup>-2</sup> h<sup>-1</sup> corresponds to an evaporation efficiency of 106% using equation (3.1). The efficiency of over 100 % can be explained by the heat energy gain from the environment caused by the lower outer surface temperature of the conical evaporator. The outer surface temperature (insets of Figure 5.9c) was about 4 °C lower than the surrounding at all conditions, leading to the energy gain from the environment. This energy gain in the form of convection and radiation was calculated using equations (3.7) and (3.9). Here we use the cone with a diameter  $\cong 1.6$  cm and a slant height  $\cong 2$  cm, so the illuminated area  $\cong 2$  cm<sup>2</sup>, the curved surface area  $\cong 5$  cm<sup>2</sup>, and the total input energy from 1 sun (1000 W m<sup>-2</sup>)  $\cong 0.2$  W. Under light illumination, the temperature of the outside curved surface of the cone was  $\cong 21$  °C, and the ambient temperature was  $\cong 25$  °C. Therefore, the 4 °C temperature difference gives rise to the convective heat gain of 0.00100 W (= 5% of input

energy) and radiative heat gain of 0.00106 W (5.8% of input energy) from the environment. The total heat gain is 10.8%. The temperature difference of 4°C between the outer surface and the environment gives rise to a heat gain of about 10% from the environment leading to a solar vapor generation efficiency of 96 %. Moreover, the ER of 3D LNO was estimated at higher solar intensities, and the values were 4.2 and 6.1 kg m<sup>-2</sup> h<sup>-1</sup> at 2 and 3 sun illumination, respectively (Figure 5.9d).

**Table 5.1.** Comparison of ERs of LNO and LCO absorber-based evaporators with recently reported metal oxides.

| Material   | Solar conc.<br>(kW m <sup>-2</sup> ) | ER (kg m <sup>-2</sup> h <sup>-1</sup> ) |            | References                          |
|--|--------------------------------------|--|------------|-------------------------------------|
|  |                                      | 2D                                       | 3D         |                                     |
| MoO <sub>x</sub>   | 1                                    | 1.255                                    | ---        | Lu <i>et al.</i> <sup>[32]</sup>    |
| WO <sub>2.72</sub> /PLA  | 2.94                                 | 3.81                                     | ---        | Chala <i>et al.</i> <sup>[38]</sup> |
| 2D WO <sub>x</sub> nanosheets  | 1                                    | 1.1017                                   | ---        | Ming <i>et al.</i> <sup>[2]</sup>   |
| Quasi-Metallic WO <sub>2.9</sub> Nanorods  | 1                                    | 1.28                                     | ---        | Sun <i>et al.</i> <sup>[33]</sup>   |
| Ti <sub>2</sub> O <sub>3</sub> NPs   | 1                                    | 1.32                                     | ---        | Wang <i>et al.</i> <sup>[30]</sup>  |
| <b>LCO</b>   | <b>1</b>                             | <b>1.38</b>                              |            | <b>This work</b>                    |
| <b>LNO</b>   | <b>1</b>                             | <b>1.45</b>                              | <b>2.4</b> | <b>This work</b>                    |
| CuFeMnO <sub>4</sub>   | 1                                    | 1.21                                     | 2.04       | Shi <i>et al.</i> <sup>[11]</sup>   |
| CuCr <sub>2</sub> O <sub>4</sub> , CoFe <sub>2</sub> O <sub>4</sub> , NiFe <sub>2</sub> O <sub>4</sub> ,<br>Fe <sub>2</sub> O <sub>4</sub> , MnCo <sub>2</sub> O <sub>4</sub> , CoMn <sub>2</sub> O <sub>4</sub> ,<br>FeMnO <sub>3</sub> , NiMnO <sub>3</sub> , CuCoMnO <sub>4</sub> | 1                                    | 1.01-<br>1.22                            | ---        |                                     |
| 3D WO <sub>3-x</sub> /Ni foam  | 1                                    | ---                                      | 1.50       | Wang <i>et al.</i> <sup>[39]</sup>  |
| MoO <sub>3-x</sub> quantum dots  | 5                                    | 4.95                                     | ---        | Ding <i>et al.</i> <sup>[40]</sup>  |
| La <sub>0.7</sub> Sr <sub>0.3</sub> CoO <sub>3</sub>   | 1                                    | ---                                      | 1.67       | Wang <i>et al.</i> <sup>[41]</sup>  |
| Black Titania Nanocages  | 1                                    | ---                                      | 1.13       | Zhu <i>et al.</i> <sup>[42]</sup>   |
| CuCr <sub>2</sub> O <sub>4</sub> /SiO <sub>2</sub>   | 1                                    | 1.32                                     | ---        | Shi <i>et al.</i> <sup>[34]</sup>   |
| TiO <sub>x</sub> (x < 2) NPs   | 1                                    | 0.8012                                   | ---        | Ye <i>et al.</i> <sup>[35]</sup>    |
| Fe <sub>3</sub> O <sub>4</sub> @C core-shell nanostructures  | 1                                    | 1.07                                     | ---        | Chen <i>et al.</i> <sup>[36]</sup>  |
| W <sub>18</sub> O <sub>49</sub> mesocrystals   | 1                                    | 1.15                                     | ---        | Chang <i>et al.</i> <sup>[37]</sup> |

Desalination is a major and widely studied application of ISSG. However, efficient desalination requires a high ER, durability, and, most importantly, the anti-clogging ability for long-term operation.<sup>[43,44]</sup> The ER was measured using 3.5 wt % of NaCl solution (average

salinity of seawater) to analyze the desalination effect of our 3D ISSG. The device was prewetted overnight in saltwater to increase the water content at the interface. After 12 h of constant illumination at 1 sun, we observed that the ER constantly decreased from the maximum value of 2.3 to 1.9 kg m<sup>-2</sup> h<sup>-1</sup> (red line of Figure 5.10a). The decrease in the ER was most likely due to insufficient water supply to the top of the cone, which caused the clogging of salt crystals on the inner (Figure 5.10c) and outer surfaces (Figure 5.10d). Also, the salt clogging on the absorber surface may reduce light absorption. No significant change in the clogged salt was found after keeping the evaporator in the dark overnight, as shown in Figure

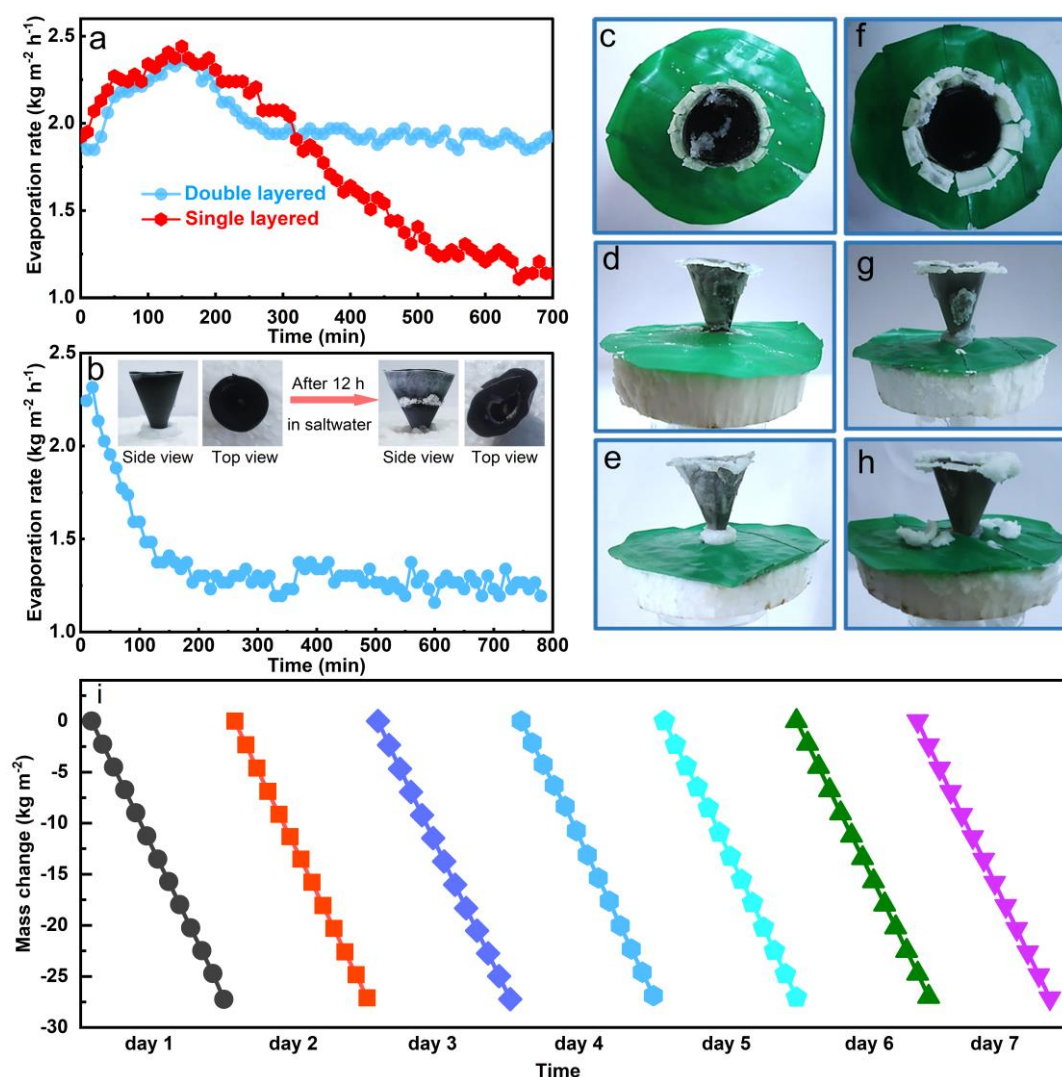


**Figure 5.10.** (a) ER of single-layered and double-layered 3D cone-shaped LNO evaporator under saltwater. (b) ER of the device made of filter paper with a lower water flow rate. Inset shows the digital photographs of the top and side view of the device before and after 12 h of continuous operation under saltwater. Digital photographs of single-layered 3D cone-shaped LNO evaporator (c) top view (d) side view after 12 h and (e) after putting overnight in the dark and double layered 3D cone shaped LNO evaporator (e) top view (f) side view after 12 h and (g) after putting overnight in the dark. (i) Mass change profile of LNO-cone for continuous 1-week operation.

5.10e. To further study the role of water supply on salt clogging, we have used a membrane filter with a pore size of  $0.22\ \mu\text{m}$ , which has a lower water flow rate of  $>1\ \text{mL min}^{-1}\ \text{cm}^{-2}$  compared to  $>2.6\ \text{mL min}^{-1}\ \text{cm}^{-2}$  for the filter paper with a pore diameter of  $0.45\ \mu\text{m}$ . As shown in Figure 10b, the ER dropped to  $1.2\ \text{kg m}^{-2}\ \text{h}^{-1}$  within the first two hours with enhanced salt clogging on the evaporator surface, confirming that the decrease in ER is due to the insufficient water supply. The problem of salt clogging was resolved by increasing the water supply using an extra layer of pristine filter paper (both the filter papers were of pore size  $0.45\ \mu\text{m}$ ) to the outer surface of the cone. The ER in the double-layered device remains almost constant from the 2<sup>nd</sup> hour for the continuous operation of 12 h (blue line in Figure 5.10a). For the double-layered device, we noticed that the salt crystallizes only at the top edge (Figure 5.10f) and on some portions of the cone's outer surface (Figure 5.10g). No salt clogging was observed in the inner light-absorbing surface. Unlike the single-layered device, the remaining clogged salt on the outer surface fell under gravity when the device was kept in the dark for over 14 hours (Figure 5.10h), and the ER on the subsequent measurement was unaffected. We have also studied the long-term usability of the double-layered evaporator by illuminating it for 12 h and

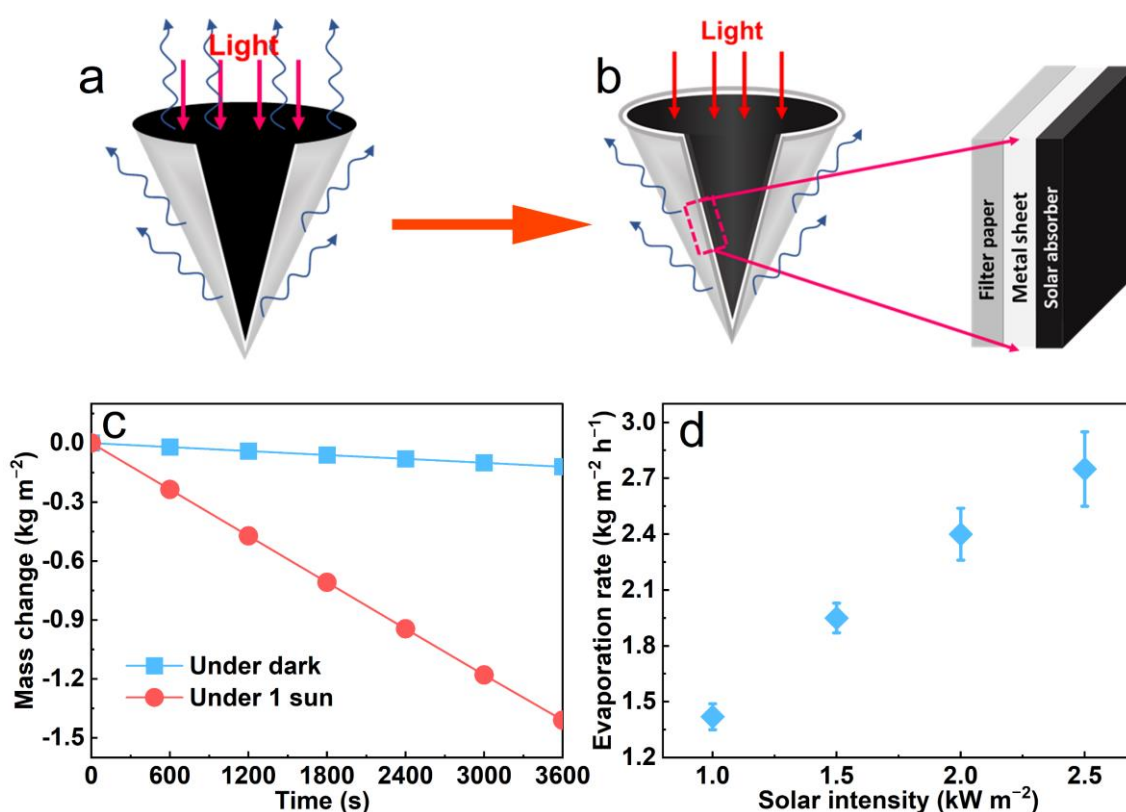


**Figure 5.11.** (a) Conventional conical evaporator with absorbing surface acting as evaporation surface. (b) Impermeable conical evaporator with separated absorbing and evaporation surfaces. (c) Mass change profile of 3D impermeable cone for 1h under dark and 1 sun illumination. (d) ER of the 3D impermeable cone with varying solar intensity.

then storing it in the dark for another 12 h per day. No significant changes in the ER were observed even after a week (Figure 5.10i).

So far, we have observed that the device always requires proper water supply management to compensate between salt rejection ability and evaporation efficiency. But the appropriate water supply management according to the illumination intensity and salt concentration conditions will become a challenge for practical application. The problem arises due to the inner surface acting both as the light-absorbing and evaporation surface (Figure 5.11a), leading to salt clogging on the absorber layer. Therefore, designing a device where the two surfaces are physically separated will efficiently deal with saltwater regardless of the solar intensity or salt concentration. Accordingly, an LNO-coated SS sheet was molded into a conical structure with LNO coating on the inner surface and filter paper wrapped on the outer surface. The thermally conductive and impermeable SS-sheet acts as a separator for the inner light-absorbing surface and the outer evaporation surface (Figure 5.11b). On solar illumination of the intensity 1 sun, the evaporator shows the highest ER of  $1.45 \text{ kg m}^{-2} \text{ h}^{-1}$ , as shown in Figure 6.11c. Further, the ER was estimated at higher solar intensities to check the stability of the device with varying illumination conditions. As shown in Figure 6.11d, it is observed that the device offers a linear increase in the ER values on increasing the solar intensities linearly.

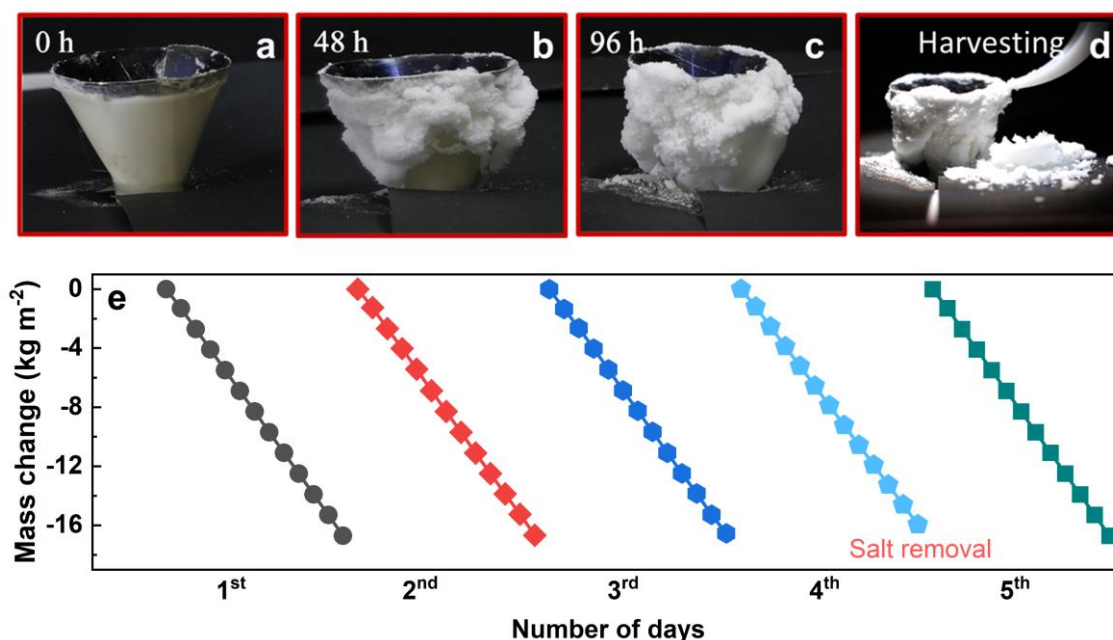


**Figure 5.12.** Digital photographs of (a-c) the accumulated salt on the evaporator for four days of continuous operation under 20 wt% salt concentration and (d) mechanical salt removal. (e) Mass change profile water using a 3D impermeable cone for continuous 5 days.

The evaporation performance of the device was also determined for saltwater of high salt concentrations (20 wt% of NaCl) by repeating the experiment for five continuous days

with 12 h in light and 12 h in the dark. As the two surfaces were separated, the salt was agglomerated only on the outer evaporation surface of the evaporator without affecting the inner absorbing surface, as shown in Figure 6.12a-c. Due to the salt accumulation, the ER decreased slightly after 4<sup>th</sup> day (Figure 6.12e), which retained its original value after removing the salt from the evaporator surface. The accumulated salt crystals were removed by applying a slight force (Figure 6.12d), which endowed with an additional application of salt harvesting with a  $0.33 \text{ kg m}^{-2} \text{ h}^{-1}$  rate.

## 5.4. Conclusion

In summary, we successfully synthesized LCO and LNO NPs and used them as absorber materials in designing 2D and 3D ISSG. The narrow bandgap with high optical absorbance helps these materials absorb light over the full range of the solar spectrum, leading to an overall efficiency of over 80% for both samples and establishing them as efficient photothermal materials. Properly utilizing the solar absorption capacity of the LNO absorber with the use of the conical 3D structure of the steam generator, we achieved a water ER of  $2.3 \text{ kg m}^{-2} \text{ h}^{-1}$ . The ER achieved by our LNO-based 3D ISSG is higher than the previously reported oxide-based ISSG. Further, the steam generators were proven effective in desalinating the seawater without compromising the ER. Also, under 1 sun illumination and a low salt concentration of 3.5 wt%, with proper water management, the salt, instead of depositing on the absorber surface, was rejected from the evaporator showing an extra advantage of salt collection.

## 5.5. References

- [1] Y. Shi, R. Li, Y. Jin, S. Zhuo, L. Shi, J. Chang, S. Hong, K.-C. Ng, P. Wang, *Joule* **2018**, 2, 1171.
- [2] I. Ibrahim, D. H. Seo, A. M. McDonagh, H. K. Shon, L. Tijing, *Desalination* **2021**, 500, 114853.
- [3] M. Golalikhani, Q. Lei, R. U. Chandrasena, L. Kasaei, H. Park, J. Bai, P. Orgiani, J. Ciston, G. E. Sterbinsky, D. A. Arena, P. Shafer, E. Arenholz, B. A. Davidson, A. J. Millis, A. X. Gray, X. X. Xi, *Nat. Commun.* **2018**, 9, 2206.
- [4] Y. Li, J. Zhou, D. Wu, *ACS Appl. Mater. Interfaces* **2019**, 11, 3565.
- [5] J. Biscaras, N. Bergeal, A. Kushwaha, T. Wolf, A. Rastogi, R. C. Budhani, J. Lesueur, *Nat. Commun.* **2010**, 1, 89.
- [6] A. Gozar, G. Logvenov, L. F. Kourkoutis, A. T. Bollinger, L. A. Giannuzzi, D. A.

- Muller, I. Bozovic, *Nature* **2008**, 455, 782.
- [7] J. S. A. Carneiro, R. A. Brocca, M. L. R. S. Lucena, E. Nikolla, *Appl. Catal. B Environ.* **2017**, 200, 106.
- [8] P. M. Shafi, V. Ganesh, A. C. Bose, *ACS Appl. Energy Mater.* **2018**, 1, 2802.
- [9] M. Prabu, P. Ramakrishnan, P. Ganesan, A. Manthiram, S. Shanmugam, *Nano Energy* **2015**, 15, 92.
- [10] Q. Shang, J. Yu, R. Hu, Z. Liu, J. Cheng, Y. Li, X. Shai, M. Huo, X. Yang, L. Li, *ACS Appl. Mater. Interfaces* **2020**, 12, 13051.
- [11] T. Arima, Y. Tokura, J. B. Torrance, *Phys. Rev. B* **1993**, 48, 17006.
- [12] W. Seok Choi, H. Nyung Lee, *Appl. Phys. Lett.* **2012**, 100, 132903.
- [13] L. Tepech-Carrillo, A. Escobedo-Morales, A. Pérez-Centeno, E. Chigo-Anota, J. F. Sánchez-Ramírez, E. López-Apreza, J. Gutiérrez-Gutiérrez, *J. Nanomater.* **2016**, 2016, 1-7.
- [14] D. U. Lee, H. W. Park, M. G. Park, V. Ismayilov, Z. Chen, *ACS Appl. Mater. Interfaces* **2015**, 7, 902.
- [15] C. Lv, H. Chen, M. Hu, T. Ai, H. Fu, *Environ. Sci. Pollut. Res.* **2021**, 28, 37142.
- [16] Y. Wen, C. Zhang, H. He, Y. Yu, Y. Teraoka, *Catal. Today* **2007**, 126, 400.
- [17] Y. Wang, J. Ren, Y. Wang, F. Zhang, X. Liu, Y. Guo, G. Lu, *J. Phys. Chem. C* **2008**, 112, 15293.
- [18] H. H. Sønsteby, E. Skaar, Ø. S. Fjellvåg, J. E. Bratvold, H. Fjellvåg, O. Nilsen, *Nat. Commun.* **2020**, 11, 2872.
- [19] G. Kresse, J. Furthmüller, *Phys. Rev. B* **1996**, 54, 11169.
- [20] P. E. Blöchl, *Phys. Rev. B* **1994**, 50, 17953.
- [21] J. P. Perdew, K. Burke, M. Ernzerhof, *Phys. Rev. Lett.* **1996**, 77, 3865.
- [22] S. L. Dudarev, G. A. Botton, S. Y. Savrasov, C. J. Humphreys, A. P. Sutton, *Phys. Rev. B* **1998**, 57, 1505.
- [23] A. M. Ritzmann, M. Pavone, A. B. Muñoz-García, J. A. Keith, E. A. Carter, *J. Mater. Chem. A* **2014**, 2, 8060.
- [24] A. Chainani, M. Mathew, D. D. Sarma, *Phys. Rev. B* **1992**, 46, 9976.
- [25] T. G. Yun, Y. Heo, H. Bin Bae, S.-Y. Chung, *Nat. Commun.* **2021**, 12, 824.
- [26] G. Gou, I. Grinberg, A. M. Rappe, J. M. Rondinelli, *Phys. Rev. B* **2011**, 84, 144101.
- [27] L. Guan, B. Liu, L. Jin, J. Guo, Q. Zhao, Y. Wang, G. Fu, *Solid State Commun.* **2010**, 150, 2011.
- [28] M. K. Stewart, J. Liu, R. K. Smith, B. C. Chapler, C.-H. Yee, R. E. Baumbach, M. B.

- Maple, K. Haule, J. Chakhalian, D. N. Basov, *J. Appl. Phys.* **2011**, *110*, 033514.
- [29] M. Umlauff, J. Hoffmann, H. Kalt, W. Langbein, J. M. Hvam, M. Scholl, J. Söllner, M. Heuken, B. Jobst, D. Hommel, *Phys. Rev. B* **1998**, *57*, 1390.
- [30] J. Wang, Y. Li, L. Deng, N. Wei, Y. Weng, S. Dong, D. Qi, J. Qiu, X. Chen, T. Wu, *Adv. Mater.* **2017**, *29*, 1603730.
- [31] Y. Wang, H. Liu, C. Chen, Y. Kuang, J. Song, H. Xie, C. Jia, S. Kronthal, X. Xu, S. He, L. Hu, *Adv. Sustain. Syst.* **2019**, *3*, 1800055.
- [32] Q. Lu, Y. Yang, J. Feng, X. Wang, *Sol. RRL* **2019**, *3*, 1800277.
- [33] L. Sun, Z. Li, R. Su, Y. Wang, Z. Li, B. Du, Y. Sun, P. Guan, F. Besenbacher, M. Yu, *Angew. Chemie Int. Ed.* **2018**, *57*, 10666.
- [34] Y. Shi, R. Li, L. Shi, E. Ahmed, Y. Jin, P. Wang, *Adv. Sustain. Syst.* **2018**, *2*, 1870026.
- [35] M. Ye, J. Jia, Z. Wu, C. Qian, R. Chen, P. G. O'Brien, W. Sun, Y. Dong, G. A. Ozin, *Adv. Energy Mater.* **2017**, *7*, 1601811.
- [36] R. Chen, K. Zhu, Q. Gan, Y. Yu, T. Zhang, X. Liu, M. Ye, Y. Yin, *Mater. Chem. Front.* **2017**, *1*, 2620.
- [37] Y. Chang, Z. Wang, Y. Shi, X. Ma, L. Ma, Y. Zhang, J. Zhan, *J. Mater. Chem. A* **2018**, *6*, 10939.
- [38] T. F. Chala, C.-M. Wu, M.-H. Chou, Z.-L. Guo, *ACS Appl. Mater. Interfaces* **2018**, *10*, 28955.
- [39] T. Wang, S. Gao, G. Wang, H. Wang, J. Bai, S. Ma, B. Wang, *J. Colloid Interface Sci.* **2021**, *602*, 767.
- [40] D. Ding, W. Huang, C. Song, M. Yan, C. Guo, S. Liu, *Chem. Commun.* **2017**, *53*, 6744.
- [41] Y. Wang, C. Wang, W. Liang, X. Song, Y. Zhang, M. Huang, H. Jiang, *Nano Energy* **2020**, *70*, 104538.
- [42] G. Zhu, J. Xu, W. Zhao, F. Huang, *ACS Appl. Mater. Interfaces* **2016**, *8*, 31716.
- [43] Y. Shao, J. Tang, N. Li, T. Sun, L. Yang, D. Chen, H. Zhi, D. Wang, H. Liu, G. Xue, *EcoMat* **2020**, *2*, e12018.
- [44] Y. Zhang, T. Xiong, D. K. Nandakumar, S. C. Tan, *Adv. Sci.* **2020**, *7*, 1903478.

## **Chapter 6**

# **In-Situ Latent Heat Transfer for Nearly 100% Condensation in Single-Stage Interfacial Solar Steam Generation**

Introduction

Experimental section

Results and discussion

Conclusion

References

## 6.1. Introduction

Considering freshwater production as the ultimate goal of SSG, water collection is the last but most crucial step. With the advancement in photothermal materials and structural design techniques, the ISSG has shown significant progress in achieving a high ER in the open atmosphere.<sup>[1-4]</sup> However, due to inefficient condensation, there is a considerable discrepancy between the ER and the actual water CR when the active photothermal material is used in a closed condensation chamber. This discrepancy is mainly attributed to the i) blockage of sunlight by the condensed mist on the condenser surface, ii) absorption of the portion of sunlight by the inner steam layer, and iii) increased humidity inside the closed chamber of the evaporator.<sup>[5-8]</sup> Therefore, developing an innovative design with an efficient water CR is essential to utilize the full potential of ISSG.

In a typical ISSG system, the condensation of the generated steam occurs from a tilted transparent cover placed on the top of the evaporator, generally made of plastic or glass.<sup>[9,10]</sup> Conventionally, the generated steam mist resides on the inner surface of the transparent condenser and blocks around 35% of the incident light, leading to a limited CR of about 0.3 to 0.5 kg m<sup>-2</sup> h<sup>-1</sup>.<sup>[11,12]</sup> Also, the increase in the condenser temperature during evaporation hampers the condensation process, leading to a decrease in the water collection.<sup>[13]</sup> External air/water flows using electricity-driven pumps were used to increase condensation by reducing the condenser temperature,<sup>[14,15]</sup> which adds to their cost and limits their practicability.<sup>[10]</sup> Another factor is the increasing internal vapor pressure/humidity during the evaporation process, which reduces the probability of collisions between the water vapor molecules and the transparent cover, reducing condensation.<sup>[9]</sup> The decrease in the internal vapor pressure/humidity using mechanical pumps in these systems has significantly enhanced the CR,<sup>[16,17]</sup> but the application of external energy sources makes it costlier for practical purposes. Further, the CR was considerably improved by designing multistage devices in which the enthalpy released in one stage during the condensation was recycled in the preceding stage.<sup>[18,19]</sup> Complicated design techniques of the multistage devices compelled to enhance the efficiency of a single-stage ISSG device for personalized water solutions. Therefore, fabricating a low-cost solar water purifier with a simple design technique and high solar-to-water collection efficiency can lead to an affordable solution for portable freshwater production.

This chapter demonstrates a simple solar water purifier with a cone-shaped evaporator placed with a tip downwards inside a cylindrical condenser made of copper of the same

diameter as the cone. The evaporator was made of a solar absorber-coated SS sheet, acting as a light-absorbing surface, and filter paper wrapped on the outer surface as the evaporation surface. A nearly 100% CR-to-ER ratio was achieved by conducting the wastewater from the reservoir to the evaporator through a cotton cloth wrapped on the condenser surfaces. Using MnO<sub>2</sub>, carbon black, and commercial acrylic paint as the absorber material, the device was able to produce freshwater at a rate of  $1.4 \pm 0.05 \text{ kg m}^{-2} \text{ h}^{-1}$  under 1 sun illumination corresponding to solar-to-water collection efficiency of over 88%, showing the versatility of the device towards the material choices. The efficient water CR is ascribed to the high thermal conductivity of the condenser, which allows latent heat to transfer from steam to the reservoir via external water flow. The device also shows a stable evaporation performance for a week of continuous operation under 3.5 wt% of saltwater. Considering cost-effectiveness, simple preparation, and higher water CR, our device strengthens the practicality of solar-driven freshwater generation.

## **6.2. Experimental section**

### **6.2.1. Materials**

MnO<sub>2</sub>, carbon black, sodium chloride, MB, and MO were purchased from Sigma-Aldrich. The acrylic paint, SS sheet, and varnish were purchased from the local market. All the chemicals were used without further purification.

### **6.2.2. Fabrication of solar water purifier**

The powders of the photothermal materials (MnO<sub>2</sub> and carbon black) were mixed with a small amount of varnish to make a paint-like slurry. Then the slurry of different photothermal materials was painted on a SS sheet, which was then kept in the oven and dried at 60 °C. The sheet was then cut and molded into a cone of diameter 5 cm and slant height 4 cm. A filter paper of pore size 0.45 μm was wrapped on the other side of the cone. A copper cylinder with a diameter equivalent to a cone was used as a condenser and was wrapped tightly with a cotton cloth for water supply. The conical evaporator was placed with the tip facing downwards on the condenser. The whole setup was covered with aluminum foil to prevent additional light from reaching the evaporator.

### 6.2.3. Material characterizations

Absorption spectra of the cone-shaped samples were recorded in the range of 300–2500 nm by a UV–vis–NIR spectrometer (Cary-5000) attached to an integrated sphere. The atomic absorption spectroscopy (AAS) (Shimadzu AA-6880 series) was used to track the concentration of different ions in seawater before and after condensation.

### 6.2.4. SSG measurements

For SSG, the evaporator was placed under AAA solar simulator (ABET 110005), and the desired light intensities were adjusted by a light meter (843 R, Newport Corporation) using a thermopile sensor (Newport Corporation, 919P-003–10). It was placed on an analytical balance (Mettler Toledo, ME204) with a precision of 100  $\mu\text{g}$  to measure the real-time mass change used to calculate the evaporation. The temperature profile was measured by a J-type thermocouple connected to a data acquisition system (Keysight DAQ970A). All the experiments were performed at ambient temperature  $\sim 23 \pm 1$   $^{\circ}\text{C}$  and relative humidity  $\sim 50 \pm 5\%$ .

## 6.3. Results and discussion

The schematic of the proposed solar water purifier is given in Figure 6.1, in which the conical photothermal evaporator consists of an absorber surface and an evaporation surface separated by an impermeable SS layer. On illumination, the photothermal layer generates heat by absorbing solar light, which then will transfer to the evaporator surface for steam generation.

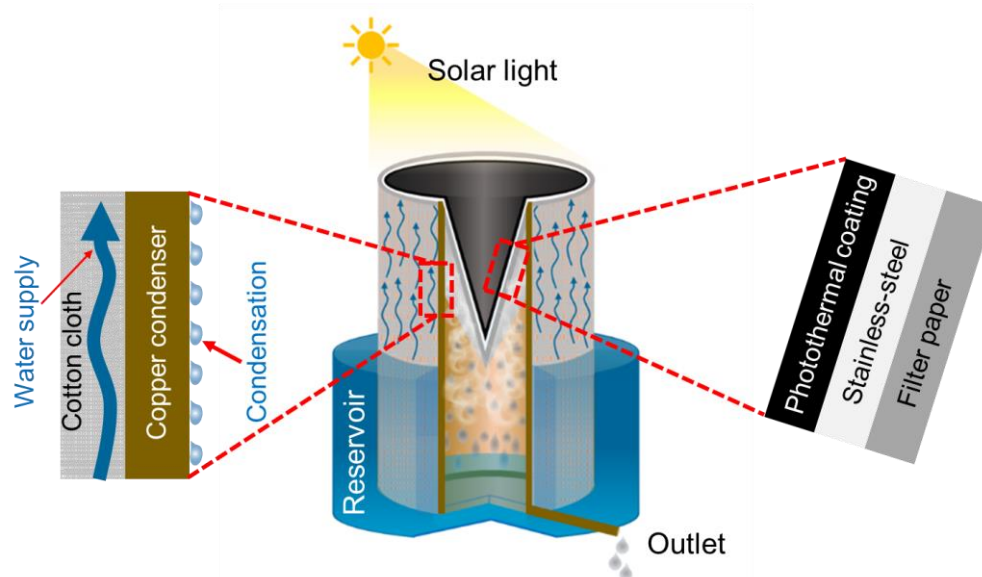


**Figure 6.1.** Schematic diagram of the solar water purifier.

The generated steam will be condensed at the inner surface of the cylindrical condenser by transferring the latent heat, which then gets transferred by convection and radiation to the atmosphere but primarily to the reservoir via water flowing through the cotton cloth wrapped outside. The high thermal conductivity of copper promotes effective heat transfer and maintains the condenser at a lower temperature, continuously producing a uniform water condensation rate for long-term operation. On the other hand, the impermeable SS layer eliminates the formation of steam mist over the evaporation surface, which hinders light absorption in conventional solar stills.

We used carbon black, MnO<sub>2</sub>, and acrylic paint as the absorber layer to study the device's versatility towards different photothermal materials. To check the evaporation performance of the device in an open atmosphere (without any condenser), the conical evaporator was placed on the insulating polystyrene foam, and the water was supplied from the reservoir to the lower tip via tissue paper. On solar illumination of the intensity 1 sun, the conical evaporator with a diameter of 5 cm shows the highest ER of 1.45 kg m<sup>-2</sup> h<sup>-1</sup> (Figure 6.2a). No significant changes in the ER were observed in the devices of different absorber materials, which can be explained due to their nearly identical absorption spectra in the conical designs, as plotted in Figure 6.2b and inset of Figure 6.2b. The high ER can be accredited to

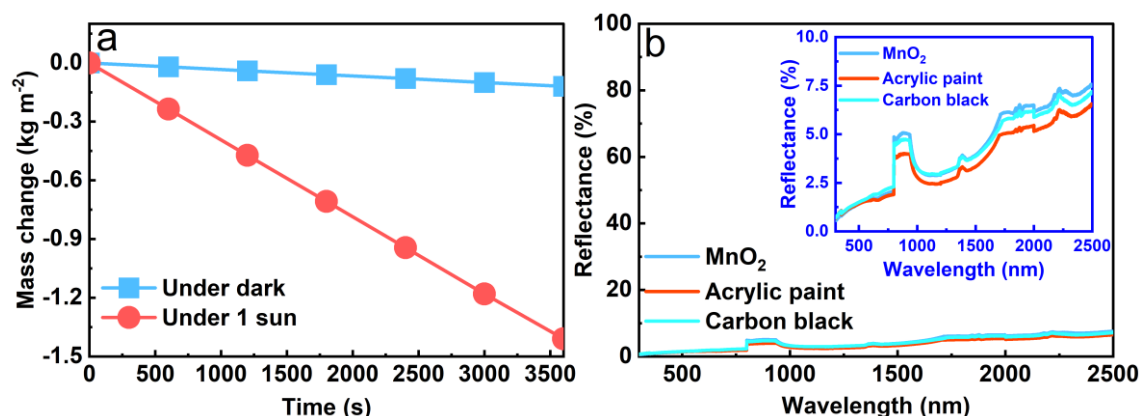


**Figure 6.2.** (a) Mass change profile of 3D impermeable cone for 1 h under dark and 1 sun illumination. (b) UV-vis-NIR spectra of cone-shaped structure coated with different photothermal materials.

the increased solar absorptance of around 96% (using equation 3.4) and the large effective evaporation area of the cone-shaped evaporator. Adding a cylindrical copper condenser with the same inner diameter as the evaporator, as shown in Figure 6.3a, we collected freshwater at a rate of around 0.6 L m<sup>-2</sup> h<sup>-1</sup>, irrespective of the absorber layer, which was much lower than the ER in the open air (Figure 6.3b). Although the condensation was not occurring over the absorber layer as in conventional solar stills, the lower water CR can be explained due to the

increased condenser's temperature nearly the same as the steam temperature (Figure 6.3c), leading to an in-efficient condensation and other related problems. A similar phenomenon has been reported by Wang *et al.*, where an additional heat sink was added to reduce the condenser temperature.<sup>[20]</sup>

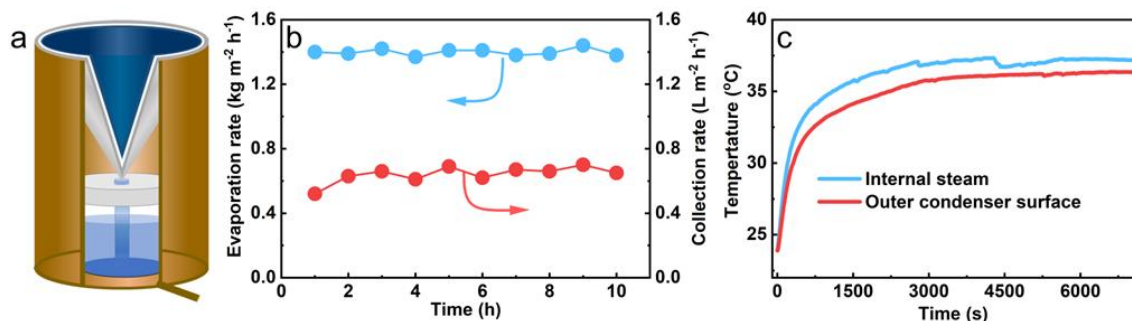


**Figure 6.3.** Schematic of the solar water purifier when water is supplied from inside the condenser. (b) ER and CR of the purifier for 10 h of continuous operation under 1 sun illumination. (c) The temperature profile of the condenser surface and the generated steam under 1 sun illumination with inside water supply.

In the actual experiment, the water was transported from the reservoir to the evaporator surface through a cotton cloth wrapped on the outer surface of the condenser, as shown in the top view and side view photographs of the evaporator (Figure 6.4a, b). Under the 1 sun illumination, the purifier continuously produced freshwater at a rate of  $1.40 \pm 0.05 \text{ L m}^{-2} \text{ h}^{-1}$  for 10 hours (Figure 6.4c), which is 2.8 times higher than the conventional solar stills.<sup>[11,12]</sup> Changing materials in the absorption layers (carbon/oxide-based materials or commercially available black paints) showed no significant change in the water CR (Figure 6.4d), demonstrating the versatility of our device towards the choice of photothermal material. The CR increased by about 133% compared to the earlier one and became almost the same as the ER of the evaporator under an open atmosphere resulting in a nearly 100% CR-to-ER ratio, which is the highest value reported so far to the best of our knowledge (Figure 6.4e).<sup>[16–18,21–29]</sup> The CR was also evaluated at higher solar intensities to check the condensation performance at higher steam generation. Increasing the illumination intensity from 1 to 2.5 sun gradually at the increment of 0.5 sun, CR was also increased linearly from 1.4 to around  $3.5 \text{ L m}^{-2} \text{ h}^{-1}$  (Figure 6.4f), confirming the nearly 100% condensation of our solar water purifier. The water collection efficiency was estimated to be about 88% by using equation (3.1) by considering  $\dot{m}$  as the CR.<sup>[22]</sup> Further, to verify the long-term desalination capacity of the purifier, the experiment was repeated for continuous operation for a week with 8 h of illumination each day, using 3.5 wt% NaCl solution. The data for water collection was recorded every hour (Figure

6.4g), and it was observed that the CR did not change significantly, and the salt crystals accumulated on the bottom portion of the evaporator (inset of Figure 6.4f) were repeatedly removed mechanically.

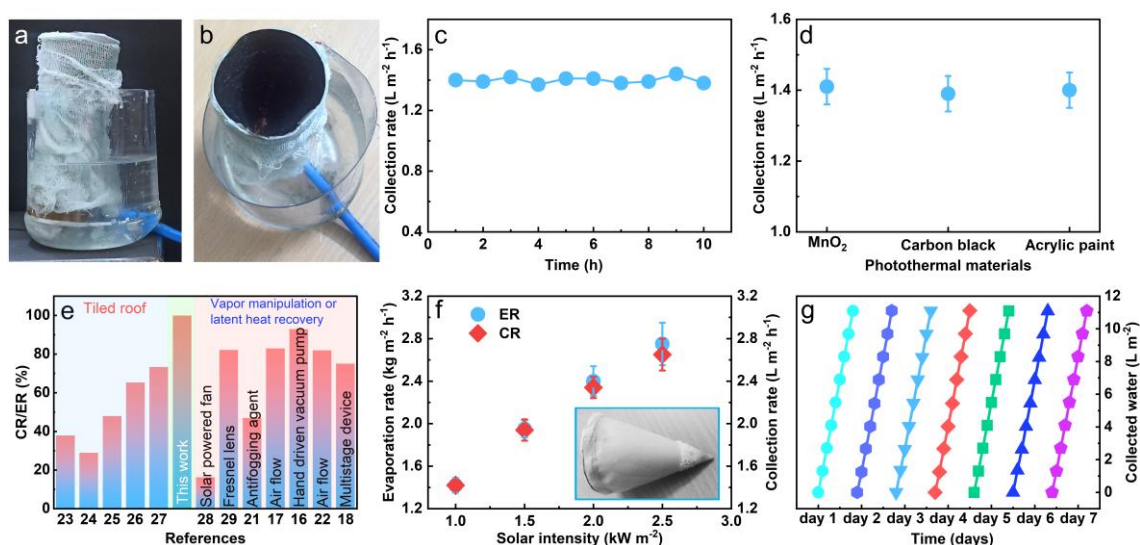


**Figure 6.4.** Digital photographs of the (a) side and (b) top view of the actual purifier. (c) CR of the purifier with water supplied through the outer surface of the condenser under 1 sun illumination. (d) CR of the purifier with different photothermal materials. (e) Comparison of CR of the purifier with recent reports. (f) Comparison of ER and CR of the device under high solar intensities. Inset shows the salt precipitation on the tip. (g) Continuous operation of the device for a week using simulated seawater of 3.5 wt% NaCl concentration.

The real-time temperature of the steam and condenser surface (both inner and outer) was recorded under dark and illumination to understand the heat-transfer process and the possible reason for nearly 100% condensation. Figure 6.5a shows that the steam temperature increased to a maximum of 32 °C, and the inner surface temperature of the condenser was 24 °C. The higher temperature gap between the hot steam and the condenser walls leads to quick condensation, resulting in enhanced CR. The latent heat produced during condensation transfers to the reservoir through the conduction process via the highly thermal-conductive

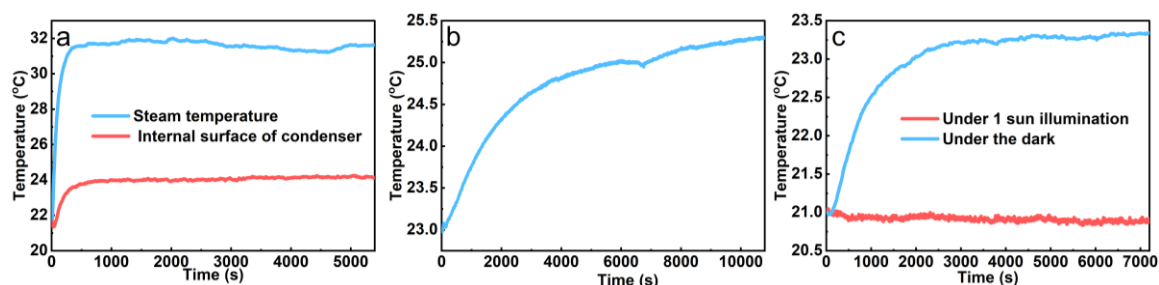


**Figure 6.5.** Temperature profile of (a) the inside surface of the condenser, the generated steam, (b) the sink under 1 sun illumination, and (c) the outer condenser surface under dark and 1 sun illumination with water supply from outside.

copper condenser, which helps maintain the condenser at a lower temperature. The same was confirmed by the gradual increase in the reservoir temperature (Figure 6.5b) when only 100 ml of wastewater was used in the reservoir. Since the wastewater is transferred from the reservoir to the evaporator through the condenser surface via capillary action, the incoming water spends sufficient time on the condenser surface to collect the latent heat transferred from steam resulting in a preheating treatment of the incoming water. The preheating of the incoming water can be observed by the increased temperature of the water flowing through the condenser surface under illumination compared to that of the dark, as given in Figure 6.5c. The preheating of incoming wastewater reduces the total heat required to convert it into steam, resulting in an overall higher ER.

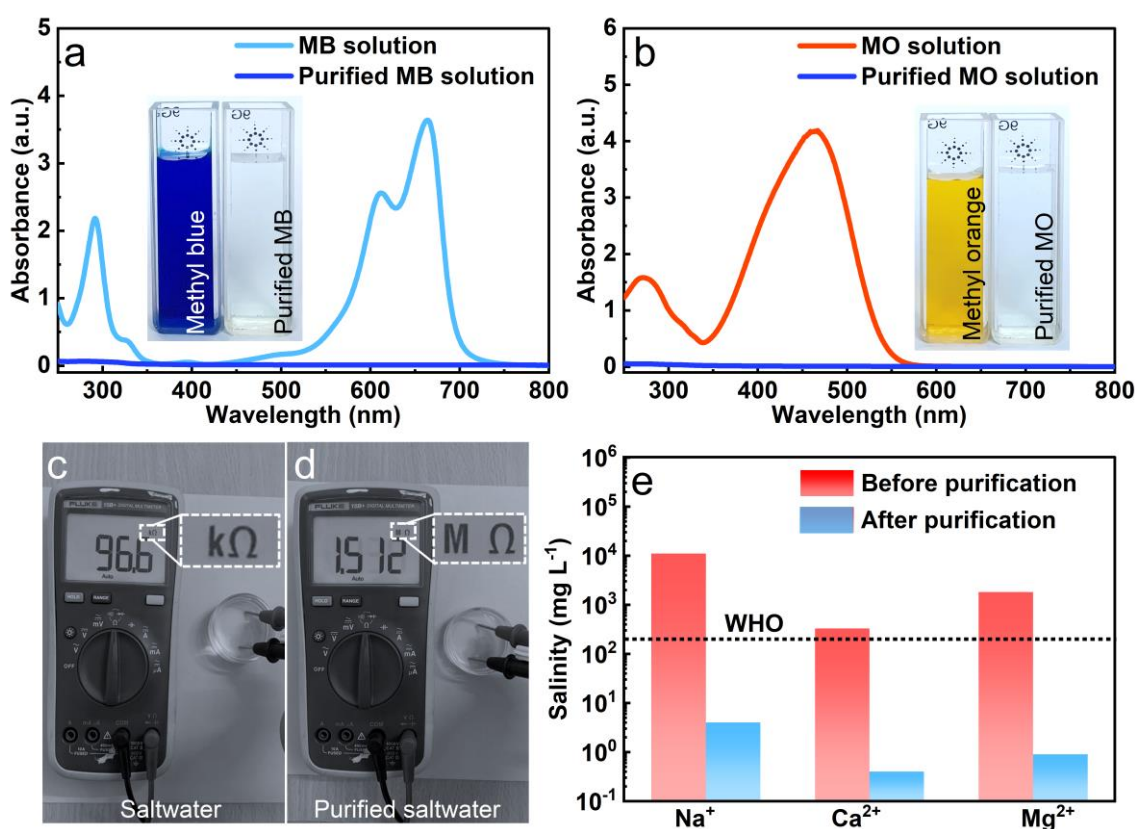


**Figure 6.6.** UV–vis spectrum of (a) MB and (b) MO solutions before and after purification and corresponding insets show the color images of MB and MO solutions before and after purification. Evaluation of water purity using a multimeter with a constant distance between electrodes for (c) saltwater and (d) purified water. (e) Ion concentration of seawater before and after purification.

To demonstrate the practical application of the solar water purifier, MB and MO were selected to simulate wastewater. The absorption spectra were used to examine the concentrations of pollutants. The purification of MB and MO is evident from the complete disappearance of the intense characteristic absorption peaks at 663 and 464 nm, respectively,

in the absorption spectra after purification (Figure 6.6a, b). The same is further visible from the optical images in the insets of Figure 6.6a, b. The desalination capacity of the device was verified by measuring the resistance before and after purification using a multimeter. As shown in Figure 6.6c, d, the resistance of the 3.5 wt % saltwater increased from 96.6 k $\Omega$  to 1.512 M $\Omega$  after purification, showing the high purification ability of the device. Further, for actual seawater desalination, we have used seawater from the Bay of Bengal. The Na<sup>+</sup>, Mg<sup>2+</sup>, and Ca<sup>2+</sup> ions concentration was estimated using AAS. The desalination capability of our device was confirmed by the substantial reduction of Na<sup>+</sup>, Mg<sup>2+</sup>, and Ca<sup>2+</sup> concentration (Figure 6.6e) below the salinity levels defined by the World Health Organization in the collected water.

## 6.4. Conclusion

In summary, we have designed a solar water purifier consisting of a conical evaporator with separated evaporation and absorption surfaces to avoid the optical losses otherwise present in conventional solar stills. Simply by changing the water transportation strategy, the water collection efficiency was increased by 133%, and the purifier attained a CR of around 1.4 L m<sup>-2</sup> h<sup>-1</sup> under 1 sun illumination, which was the same as the ER of the evaporator in an open atmosphere, leading to about 100% CR-to-ER ratio. Because of its low cost, simple design technique, and high CR-to-ER ratio, this work provides a step forward for utilizing the ISSG technique toward practicality.

## 6.5. References

- [1] F. Zhao, Y. Guo, X. Zhou, W. Shi, G. Yu, *Nat. Rev. Mater.* **2020**, *5*, 388.
- [2] Z. Huang, Y. Liu, S. Li, C.-S. Lee, X.-H. Zhang, *Small Methods* **2022**, *6*, 2200835.
- [3] Y. Liu, J. Zhao, S. Zhang, D. Li, X. Zhang, Q. Zhao, B. Xing, *Environ. Sci. Nano* **2022**, *9*, 2264.
- [4] Y. Bian, Q. Du, K. Tang, Y. Shen, L. Hao, D. Zhou, X. Wang, Z. Xu, H. Zhang, L. Zhao, S. Zhu, J. Ye, H. Lu, Y. Yang, R. Zhang, Y. Zheng, S. Gu, *Adv. Mater. Technol.* **2019**, *4*, 1800593.
- [5] L. Zhao, C. Du, C. Zhou, S. Sun, Y. Jia, J. Yuan, G. Song, X. Zhou, Q. Zhao, S. Yang, *ACS Sustain. Chem. Eng.* **2020**, *8*, 4362.
- [6] L. Noureen, Z. Xie, Y. Gao, M. Li, M. Hussain, K. Wang, L. Zhang, J. Zhu, *ACS Appl. Mater. Interfaces* **2020**, *12*, 6343.

- [7] F. Zhao, X. Zhou, Y. Shi, X. Qian, M. Alexander, X. Zhao, S. Mendez, R. Yang, L. Qu, G. Yu, *Nat. Nanotechnol.* **2018**, *13*, 489.
- [8] Y. Zhang, T. Xiong, D. K. Nandakumar, S. C. Tan, *Adv. Sci.* **2020**, *7*, 1903478.
- [9] T. Ding, Y. Zhou, W. L. Ong, G. W. Ho, *Mater. Today* **2021**, *42*, 178.
- [10] Z. Xu, Z. Li, Y. Jiang, G. Xu, M. Zhu, W.-C. Law, K.-T. Yong, Y. Wang, C. Yang, B. Dong, F. Xing, *J. Mater. Chem. A* **2020**, *8*, 25571.
- [11] G. Ni, S. H. Zandavi, S. M. Javid, S. V. Boriskina, T. A. Cooper, G. Chen, *Energy Environ. Sci.* **2018**, *11*, 1510.
- [12] A. E. Kabeel, *Energy* **2009**, *34*, 1504.
- [13] Z. M. Omara, A. S. Abdullah, A. E. Kabeel, F. A. Essa, *Renew. Sustain. Energy Rev.* **2017**, *78*, 176.
- [14] B. Janarthanan, J. Chandrasekaran, S. Kumar, *Desalination* **2006**, *190*, 51.
- [15] P. U. Suneesh, R. Jayaprakash, T. Arunkumar, D. Denkenberger, *Desalination* **2014**, *337*, 1-5.
- [16] W. Li, Z. Li, K. Bertelsmann, D. E. Fan, *Adv. Mater.* **2019**, *31*, 1900720.
- [17] Y. Guo, X. Zhou, F. Zhao, J. Bae, B. Rosenberger, G. Yu, *ACS Nano* **2019**, *13*, 7913.
- [18] Z. Xu, L. Zhang, L. Zhao, B. Li, B. Bhatia, C. Wang, K. L. Wilke, Y. Song, O. Labban, J. H. Lienhard, R. Wang, E. N. Wang, *Energy Environ. Sci.* **2020**, *13*, 830.
- [19] E. Chiavazzo, M. Morciano, F. Viglino, M. Fasano, P. Asinari, *Nat. Sustain.* **2018**, *1*, 763.
- [20] F. Wang, N. Xu, W. Zhao, L. Zhou, P. Zhu, X. Wang, B. Zhu, J. Zhu, *Joule* **2021**, *5*, 1602.
- [21] S. Cheng, Z. Sun, Y. Wu, P. Gao, J. He, Z. Yin, L. Liu, G. Li, *J. Mater. Chem. A* **2021**, *9*, 22428.
- [22] H. Lu, W. Shi, F. Zhao, W. Zhang, P. Zhang, C. Zhao, G. Yu, *Adv. Funct. Mater.* **2021**, *31*, 2101036.
- [23] P. Zhang, Q. Liao, H. Yao, H. Cheng, Y. Huang, C. Yang, L. Jiang, L. Qu, *J. Mater. Chem. A* **2018**, *6*, 15303.
- [24] X. Wang, Q. Liu, S. Wu, B. Xu, H. Xu, *Adv. Mater.* **2019**, *31*, 1807716.
- [25] Y. Guo, F. Zhao, X. Zhou, Z. Chen, G. Yu, *Nano Lett.* **2019**, *19*, 2530.
- [26] L. Wu, Z. Dong, Z. Cai, T. Ganapathy, N. X. Fang, C. Li, C. Yu, Y. Zhang, Y. Song, *Nat. Commun.* **2020**, *11*, 521.
- [27] Y. Xu, C. Tang, J. Ma, D. Liu, D. Qi, S. You, F. Cui, Y. Wei, W. Wang, *Environ. Sci. Technol.* **2020**, *54*, 5150.

- [28] L. Zhang, B. Tang, J. Wu, R. Li, P. Wang, *Adv. Mater.* **2015**, 27, 4889.
- [29] B. Gong, H. Yang, S. Wu, G. Xiong, J. Yan, K. Cen, Z. Bo, K. Ostrikov, *Nano-Micro Lett.* **2019**, 11, 51.

# Chapter 7

## **Simultaneous Freshwater and Electricity Generation in ISSG**

Introduction

Experimental section

Results and discussion

Conclusion

References

## 7.1. Introduction

Previous chapters discuss efficient freshwater production by developing an evaporator through a series of materials and structural design modifications. In addition to freshwater, energy is also a big challenge to humanity due to its high demand and limited sources.<sup>[1,2]</sup> Over the past few years, significant efforts have been invested in producing energy together with freshwater in ISSG.<sup>[3–5]</sup> For example, the temperature difference between the evaporative surface and bulk water and the salinity gradient caused by the water evaporation were used to produce electricity.<sup>[6–8]</sup> Unfortunately, these systems require a high solar illumination intensity to obtain sufficient temperature difference or maintain enough salinity gradient. This hinders their practical applications and limits the energy generation under illumination only. Furthermore, the power produced is insufficient to continuously operate a functional device (like an LED) without using energy storage devices, limiting their large-scale application. Therefore, finding an alternative system that can produce sufficient power to run functional appliances without using any energy storage devices under both illumination and dark conditions is essential.

Being flexible, eco-friendly, low cost, and easy to fabricate, the paper has gained significant interest as a substrate in various electronic devices such as thin-film transistors, sensors, photodiodes, and so forth.<sup>[9–14]</sup> The micro-channels of paper have an attractive characteristic that the fluid can flow within a microfluidic device using the capillary action without any external pumping, making it suitable for various applications.<sup>[15,16]</sup> Electricity is one of the applications produced by flowing an electrolyte through a small strip of filter paper.<sup>[17–19]</sup> Connecting such electricity-generating paper strips as the water-conducting paths to an evaporator in conventional ISSG will be an effective strategy to generate electricity and freshwater simultaneously.

This chapter presents two different ways of simultaneous production of freshwater and electricity. In the first case, a two-legged strip of Whatman filter paper with two electrodes on the side ends parallel to the flow direction was used to conduct water from the reservoir to the surface of a cone-shaped evaporator. The evaporator was made of an aluminum sheet coated with a SSA on the inner side and hydrophilic PVDF membrane filter wrapped on the outer side. Using 3.5 wt% saltwater on one leg and tap water on the other, the device shows an ER of around  $2.6 \text{ kg m}^{-2} \text{ h}^{-1}$  under 1 sun illumination and  $1.2 \text{ kg m}^{-2} \text{ h}^{-1}$  under the dark and simultaneously produces  $V_{OC}$  of 150 mV and  $I_{SC}$  of  $6.5 \mu\text{A}$  across each strip for one week of continuous operation. As electricity generation mainly depends on the ionic concentration gradient within the conducting channels,  $V_{OC}$  also persists at a low ER, showing its capacity for

all-day-long electricity generation. The  $V_{OC}$  increased gradually from 150 mV to 250 mV when salt concentration was increased from 3.5 wt% to 20 wt%, without any significant changes in the ER. Furthermore, we achieved a combined  $V_{OC}$  of 920 mV with a power density of  $9.9 \text{ mW m}^{-2}$  by connecting four channels to the evaporator. The device's versatility was tested by replacing saltwater with different ions (HCl, KCl, KOH), and it shows a stable  $V_{OC}$  over 100 mV. These results demonstrate the potential of our two-legged device for seawater desalination and power generation simultaneously.

In the second case, unlike the two-legged device, enhanced electricity production was observed when a single electrolyte solution was conducted in a strip with electrodes at the top and bottom. Four such strips were attached to the faces of a cuboid-shaped evaporator to produce both electricity and freshwater simultaneously. A single strip conducting 3.5 wt% of saltwater from the reservoir to the evaporator generated a  $V_{OC}$  of  $\sim 0.7 \text{ V}$  and  $I_{SC} \sim 26 \mu\text{A}$ . Also, an ER of  $0.5 \text{ kg m}^{-2} \text{ h}^{-1}$  in the dark and  $1.9 \text{ kg m}^{-2} \text{ h}^{-1}$  under 1 sun illumination were achieved with corresponding evaporation efficiency of 88%. Further, combining all four strips in series, the device produces a  $V_{OC}$  of  $\sim 2.7 \text{ V}$  and sufficient power to run an LED or a digital calculator without the help of any energy storage devices and irrespective of the illumination conditions. Also, the device could run a digital watch when two pairs of series-connected strips were connected in parallel. These integrated strategies show a significant advancement in simultaneous freshwater and electricity production.

## **7.2. Experimental section**

### **7.2.1. Materials**

The SSA consisting of a cermet (ETA plus) coated on an aluminum sheet was provided by Alanod Solar, India. Conductive silver paste, sodium chloride, potassium hydroxide, sodium hydroxide, magnesium sulphate, and hydrochloric acid were purchased from Sigma-Aldrich. The Whatman filter paper with pore  $11 \mu\text{m}$  was used. PVDF filter paper with pore sizes of  $0.45 \mu\text{m}$  was purchased from Merck Millipore Company. All the chemicals were used without further purification.

### **7.2.2. Device fabrication**

For electricity generation, the two-legged device was prepared following the method given in the report by Arun *et al.*<sup>[17]</sup> In brief, the Whatman filter paper was tailored into the desired shape, followed by soaking in DI water for 1 h to remove impurities. After drying, the pencil

was stroked on the filter paper to make the electrodes. The wires were connected using conductive silver paste and dried at 75 °C. Then an SSA-coated aluminum sheet was cut and molded into a conical shape of diameter 2 cm with a slant height of 2 cm and then fixed using copper tape. The final device was prepared by attaching the two-legged filter paper strips to the cone's outer surface covered by PVDF filter paper which acts as an evaporation surface. Similarly, a cuboid-shaped evaporator with dimensions 1.5 cm × 1.5 cm × 2.5 cm / 5 cm was prepared using the same SSA-coated aluminum sheet in the second case. The final device was designed by cutting filter paper into strips of length 8 cm / 10.5 cm, then attached to the outer walls of the cuboid using a stapler. The voltage was measured between the upper electrode at the top end of the strip and the lower electrode in the saltwater reservoir. The strips were dipped into the reservoir so that the channel length, which is the length between the upper electrode and the water surface, remained between 3 to 4 cm.

### **7.2.3. Material characterizations**

SEM (JEOL JSM 7900F) and EDX spectroscopy (ULTIM MAX- Oxford) were characterized to study the salt accumulation on the device. Absorption spectra were measured in the range of 300 to 2500 nm using a UV-vis-NIR spectrometer (Cary-5000).

### **7.2.4. Solar steam and electricity generation measurements**

The setup of the whole device was placed on an analytical balance (Mettler Toledo, ME204) with an accuracy of 100 µg to measure the real-time mass change used to calculate the ER. The light was illuminated on the device using a AAA solar simulator (ABET 110005). The intensity of incident light was adjusted at 1sun by a thermopile sensor (Newport Corporation, 919P-003–10) connected to a light meter (Newport Corporation, 843-R). The generated voltages and the currents were recorded using a sourcemeter (Keithley 2450). All the experiments were performed at a room temperature of ~26 °C and relative humidity of ~ 55%.

## **7.3. Results and discussion**

Transporting different electrolytes through a strip of filter paper using two different inlets produces electricity, and the same can be measured simply by connecting two electrodes formed by scribing a pencil (Figure 7.1a).<sup>[17]</sup> A constant fluid flow along the length of the strips is necessary for continuous long-term power generation, which can be obtained by connecting the outlet of the channels to a conventional solar steam generator, as shown in Figure 7.1b. Synergistic integration of such paper-based electricity generators with SSG can simultaneously

produce freshwater and electricity. Using a 3D conical evaporator will increase the ER by reducing the heat losses under illumination and providing a large effective surface area to maintain a sufficient dark ER necessary for all-day electricity generation.

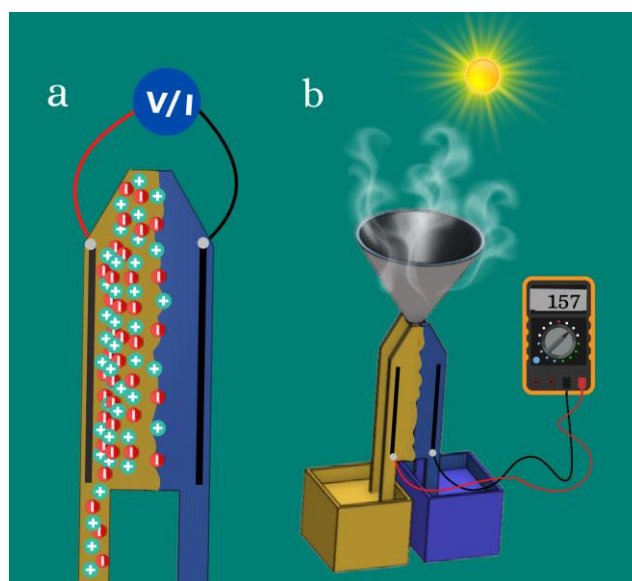


**Figure 7.1.** Schematic diagram of (a) a single two-legged strip showing the ionic concentration gradient perpendicular to the direction of fluid flow and (b) the two strips connected to the evaporator showing simultaneous generation of steam and electricity.

In the actual experiment, two strips were used to transport water from bulk to the bi-layered conical evaporator, as shown in Figure 7.2a. The inner layer of the evaporator consists of SSA coated on an aluminum sheet with a solar absorption of 96%, acts as a light absorber, and the outer PVDF membrane filter serves as the evaporation surface. Firstly, we used saltwater (3.5 wt% NaCl concentration) in one leg and regular tap water in the other as the wastewater sources to simulate our device, and the mass changes were recorded using a weighing balance under dark and light. Figure 7.2b shows the real-time mass changes of water, which were then used to calculate the water ER. The device offers an ER of 1.2 and 2.6 kg m<sup>-2</sup> h<sup>-1</sup> under dark and 1 sun illumination, respectively, which are much faster than pure water (0.4 kg m<sup>-2</sup> h<sup>-1</sup>). The ER achieved here is similar to the value reported by Zhang *et al.*<sup>[20]</sup> using the same SSA-coated aluminum sheet.

The two electrodes of a strip were connected to a sourcemeter to measure the  $V_{OC}$  and  $I_{SC}$  continuously. The  $V_{OC}$  gradually rises after connecting the legs to the regular tapwater and saltwater and saturates over 150 mV, and on the contrary, the  $I_{SC}$  decreased to a stable value of about 6.5  $\mu$ A, as shown in Figure 7.2c. The device was operated continuously for 6 h under illumination, followed by 6 h in the dark to check the continuity. As shown in Figure 7.2d,  $V_{OC}$  remained almost constant for 12 h, but the ER decreased to its dark value after switching off

the illumination. Further, to verify the long-term usability of the device for both steam and voltage generation, the experiment was repeated daily under 10 h of illumination, followed by 14 h in the dark for 8 days. The mass changes of water were recorded every hour, while the  $V_{OC}$  value was noted every morning and evening. As shown in Figure 7.2e, the ER does not change significantly, and the  $V_{OC}$  maintains an approximate value of 150 mV for 8 days.

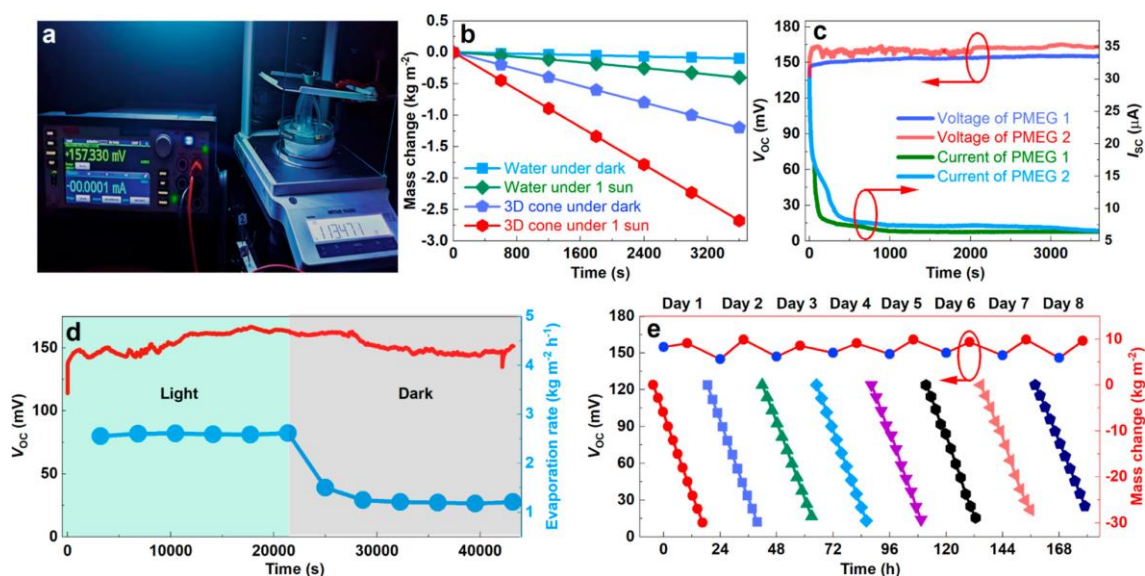


**Figure 7.2.** (a) Photograph showing the setup for simultaneous voltage and steam generation. (b) Mass change curves under different illumination conditions. (c) Time response of  $V_{OC}$  and  $I_{SC}$  of the two individual strips. (d) Continuous operation of the device for 6 h in light, followed by 6 h in the dark, and (e) 8 days of continuous operation of the device for both voltage and steam generation with 10 h in light, followed by 14 h in the dark. The blue dot in the voltage graph indicates the value in the morning (just before the light source was turned on), and the red dot represents the value in the evening (just before the light source was turned off)

The electricity generation is most likely attributed to the difference in diffusion rates between anions and cations<sup>[21]</sup> along the horizontal direction in presence of the ionic concentration gradient perpendicular to the direction of water flow, and the same was verified using SEM and EDX. Figure 7.3a shows the photograph of a dried strip after 10 hours of continuous operation with 3.5 wt% salt concentration on one leg and tap water on the other with a separation of 7 mm between the two electrodes. The SEM images of the interface (highlighted in the dotted rectangle) in Figure 7.3b show that one side of the channel is free of salt about up to 1.3 mm, followed by a gradual increase in salt concentration. The formation of a salinity gradient was prominently visible in the EDX images showing the presence of Na<sup>+</sup> and Cl<sup>-</sup> ions at one side of the interface (Figure 7.3c, d). Fluids with different salt concentrations were also used in the two legs of the strip to clarify our claim. The  $V_{OC}$  was close to zero when both the legs were conducting identical solutions while the voltage was

increasing gradually with an increase in the salinity gradient between the two legs, as shown in Figure 7.3e. Our proposition was further confirmed by achieving significant values of the  $V_{OC}$  by using different ions (HCl, KOH, KCl) on one leg and tapwater on the other (Figure 7.3f). The pH dependence of  $V_{OC}$  can be explained by the variation of the zeta potential of filter paper.<sup>[18]</sup>

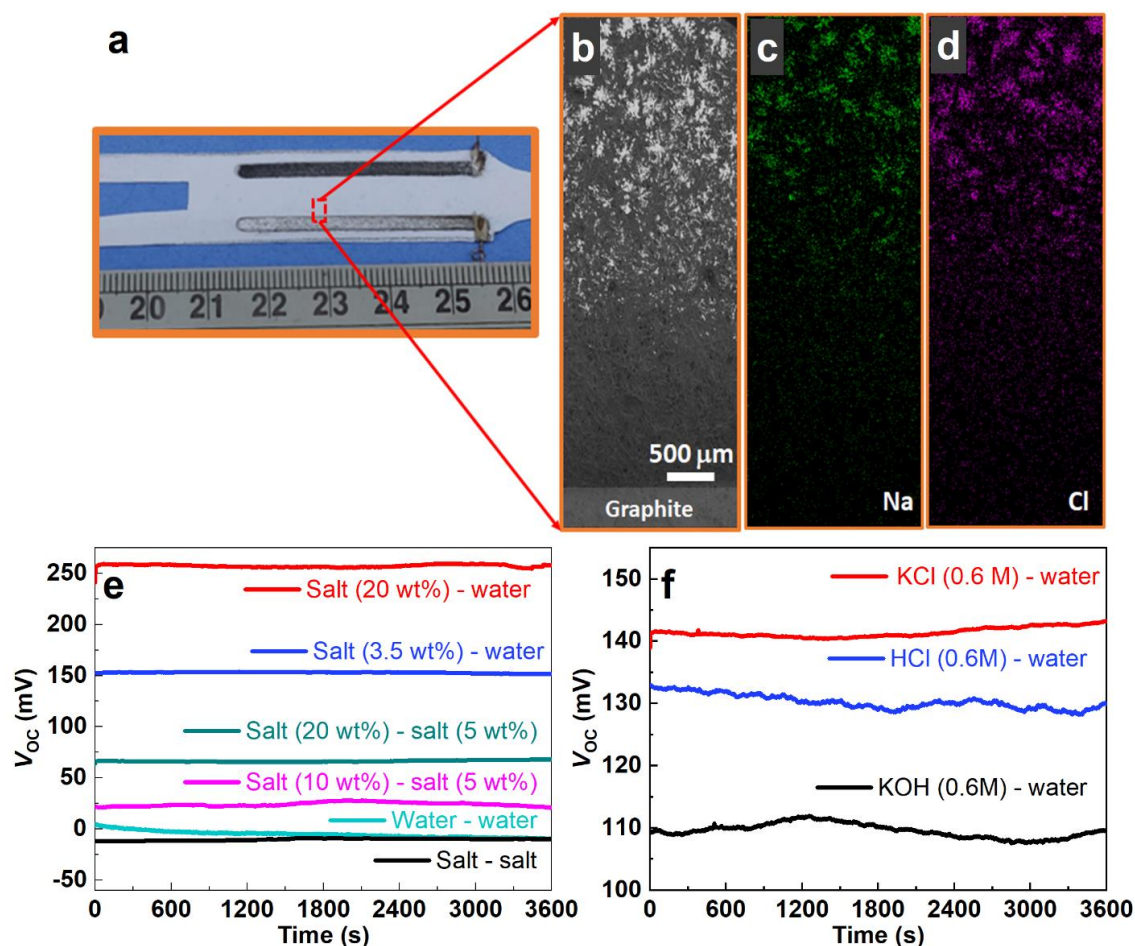


**Figure 7.3.** (a) Photograph of the dried strip after 10 h of continuous operation. (b) The SEM image shows the salinity gradient. EDX images showing the ionic concentration gradient for (c) Na and (d) Cl. (e) Time response of  $V_{OC}$  across the strip when solutions of different salt concentrations are transported in two legs. (f) Time response of  $V_{OC}$  across the strip with tap water on one leg and solutions of different ions flowed on the other.

To improve the overall device performance further, we attached the four strips with the evaporator, and the saltwater concentration was kept at 20 wt%. In addition, by connecting all four strips in series, we achieved a  $V_{OC}$  of about 920 mV and  $I_{SC} \sim 15.5 \mu A$  (Figure 7.4a). The  $V_{OC}$  value achieved here is higher than the earlier reported values,<sup>[22–29]</sup> as shown in Figure 7.4b. We also evaluated the voltage and current by connecting the devices in different series and parallel combinations. As shown in Figure 7.4c, the  $V_{OC}$  and  $I_{SC}$  increased linearly by increasing the number of devices connected in series and parallel. The maximum  $I_{SC}$  of 50  $\mu A$

was achieved by connecting all four devices in parallel. We further studied the output performance of the device by connecting various load resistance to the output circuit keeping all the devices in a series combination. As shown in Figure 7.4d, the current of the circuit drops from 15.4 to 0  $\mu\text{A}$  while the voltage increases from 0 to 920 mV with the increase in load resistance, and the maximum power output value of  $9.9 \text{ mW m}^{-2}$  (Figure 7.4e) was achieved at a load resistance of  $2 \times 10^4 \Omega$ . Although our maximum output power density is lower than some reports, the simple design technique and all-day-long electricity generation provide a significant advancement in terms of simultaneous electricity and freshwater generation. We also observed that the device could directly act as a power source to charge capacitors. As shown in Figure 7.4f, two different capacitors of capacitance 470 and 4700  $\mu\text{F}$  were fully charged in about 20 and 33 min, respectively, using the four strips in series. Connecting two such fully charged capacitors (4700  $\mu\text{F}$ ), the stored electricity lit a 1.5 V red LED (inset of Figure 7.4f), demonstrating a considerable practical application.

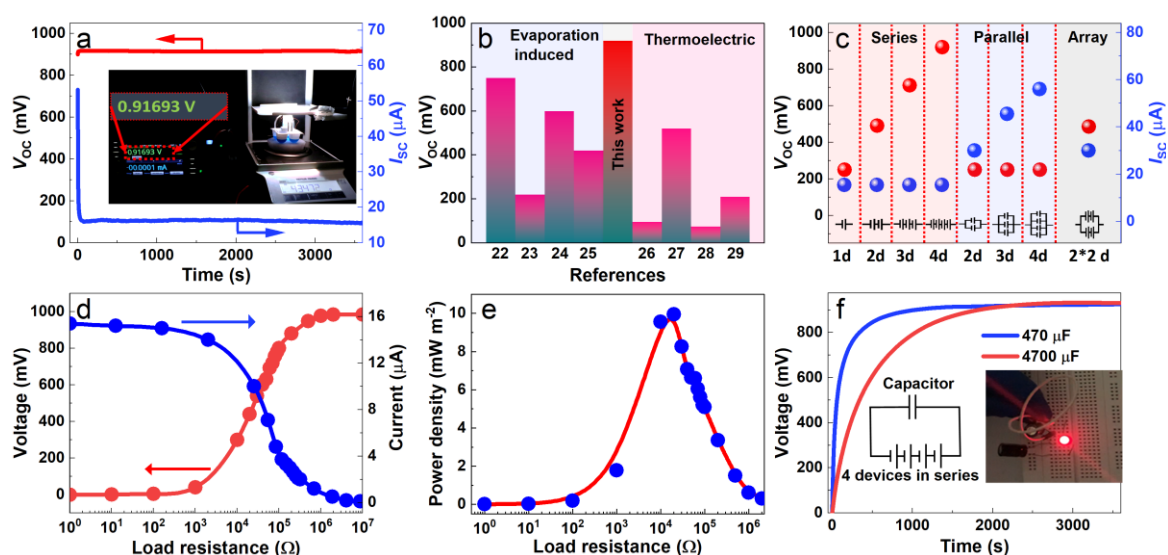


**Figure 7.4.** (a) The  $V_{OC}$  and  $I_{SC}$  of 4 strips connected in series, keeping one leg of every device at 20 wt% saltwater and tap water on the other. (b) Comparison of  $V_{OC}$  of our device with recent reports. (c) Current–voltage values of several individual strips and their series/parallel combinations. Variation of output (d) voltage and current, and (e) power density of the device measured as a function of external load resistance when all four strips were connected in series. (f) Voltage–time curves of 470 and 4700  $\mu\text{F}$  capacitors being charged by four strips in series, inset shows the screenshot of a video of a glowing red LED taken after connecting it across two charged capacitors (4700  $\mu\text{F}$ ) attached in parallel.

Further, it was observed that the voltage generation increases when a device with electrodes now at the top and bottom conducts a single electrolyte solution from both legs. Also, for better performance, the conical evaporator was replaced with a cuboid shaped evaporator with no change in the material. Figure 7.5a shows the schematic arrangement of a

cuboid-shaped evaporator with a projected area of  $1.5 \times 1.5 \text{ cm}^2$  and a height of 2.5 cm connected with four independent water-conducting strips attached to its outer walls. The lower end of the strips is dipped vertically into the reservoir to uptake saltwater to the evaporator (3.5 wt% NaCl solution). On illumination, the evaporator absorbed  $> 96\%$  of the incident light and converted it into heat via the photothermal effect<sup>[20]</sup> used to evaporate the saltwater. The evaporation performance of the device was monitored under the light intensity of 1 sun. As shown in Figure 7.5b, the device shows ERs of  $0.5 \text{ kg m}^{-2} \text{ h}^{-1}$  and  $1.9 \text{ kg m}^{-2} \text{ h}^{-1}$  under dark and 1 sun illumination, respectively, faster than pure water.

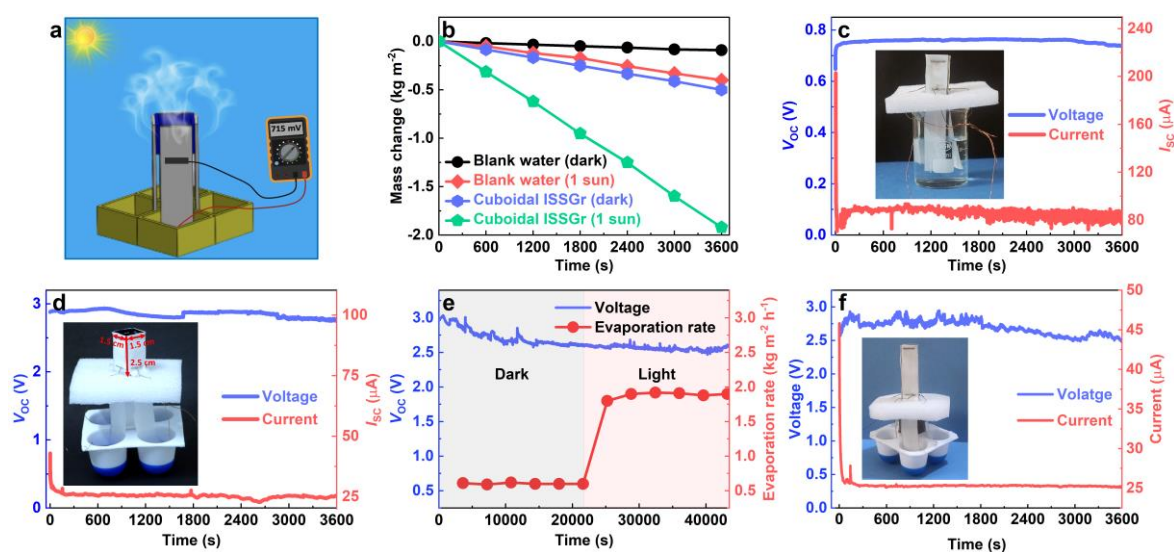


**Figure 7.5.** (a) Schematic model of a cuboid-shaped freshwater-electricity generator with four filter paper strips attached to the outer surfaces. (b) Mass change curves of salt water under different illumination conditions. Time response of  $V_{OC}$  and  $I_{SC}$  of the device connecting all four strips in (c) parallel and (d) series. Insets of the respective figures show the device with the strips connected in parallel and series. (e) Continuous operation of the device for 6 h in the dark followed by 6 h under 1 sun illumination. (f) Time response of  $V_{OC}$  and  $I_{SC}$  for the device of height 5 cm with all four strips connected in series.

The voltage starts to appear immediately after the fluid touches the upper electrode of the strip and gradually rises and reaches a maximum, followed by a steady state. Each water conducting strip saturates at an approximate  $V_{OC}$  and  $I_{SC}$  of 0.7 V and 26  $\mu\text{A}$ , respectively. Connecting all the strips in parallel, we achieved a  $V_{OC}$  of  $\sim 0.7 \text{ V}$  and an  $I_{SC}$  of  $\sim 85 \mu\text{A}$  (Figure 7.5c), whereas a series combination shows a maximum  $V_{OC}$  of  $\sim 2.7 \text{ V}$  and  $I_{SC}$  of  $\sim 26 \mu\text{A}$  (Figure 7.5d). It is important to mention that for the parallel combination, all four strips can be dipped in a single reservoir (inset of Figure 7.5c), but to get a series combination, separate reservoirs are required, as given in the inset of Figure 7.5d. The device was also operated continuously for 6 h in the dark followed by 6 h in constant light (1 sun) to study the long-term light dependence. Although the ER jumps to  $1.9 \text{ kg m}^{-2} \text{ h}^{-1}$  on illumination from the dark value,

the  $V_{OC}$  does not show any significant change from its maximum value for the entire measurement duration of 12 h (Figure 7.5e), indicating an additional advantage of the all-day-long electricity production capacity of our evaporator. Furthermore, we tested the device's performance by increasing the height to 5 cm, keeping the same projected area, and observed no change in the  $V_{OC}$  and  $I_{SC}$ , as plotted in Figure 7.5f. The performances of our two types of devices are compared with the recent reports for simultaneous steam and electricity generators in Table 7.1.<sup>[8,22,32,33,23–28,30,31]</sup>

**Table 7.1.** Comparison of the evaporation and electricity performances of devices with some recent reports.

| References                          | ER<br>( $\text{kg m}^{-2}$<br>$\text{h}^{-1}$ ) | Output power<br>density ( $\text{mW m}^{-2}$ ) | All-day<br>electricity<br>generation | Salt<br>harvesting |
|-------------------------------------|---|--|--------------------------------------|--------------------|
| Liu <i>et al.</i> <sup>[25]</sup>   | 1.93  | 0.04   | No                                   | No                 |
| Xiao <i>et al.</i> <sup>[24]</sup>  | 1.15  | ---  | Decreased<br>in dark                 | No                 |
| Zhu <i>et al.</i> <sup>[30]</sup>   | 1.35  | 400  | No                                   | No                 |
| Zhang <i>et al.</i> <sup>[26]</sup> | 1.3354  | 400  | No                                   | No                 |
| Zong <i>et al.</i> <sup>[27]</sup>  | 1.72  | ---  | No                                   | No                 |
| Dao <i>et al.</i> <sup>[22]</sup>   | 1.48  | 248.57   | Yes                                  | No                 |
| Yang <i>et al.</i> <sup>[8]</sup>   | 1.1   | 1000   | No                                   | No                 |
| Zheng <i>et al.</i> <sup>[31]</sup> | 1.69  | 974  | No                                   | No                 |
| Xu <i>et al.</i> <sup>[32]</sup>    | 6.8   | ---  | No                                   | No                 |
| Wei <i>et al.</i> <sup>[28]</sup>   | 1.38  | ---  | No                                   | No                 |
| Ding <i>et al.</i> <sup>[23]</sup>  | 1.19  | 0.35   | No                                   | No                 |
| Ma <i>et al.</i> <sup>[33]</sup>    | 2.07  | 18.2   | Yes                                  | No                 |
| <b>Two legged-device</b>            | <b>2.6</b>                                      | <b>9.9</b>                                     | <b>Yes</b>                           | <b>Yes</b>         |
| <b>Single-legged device</b>         | <b>1.9</b>                                      | <b>96/1200</b>                                 | <b>Yes</b>                           | <b>Yes</b>         |

The applicability of the generated electricity from our device was verified by operating small electronic appliances. In a series combination, our device was able to light up an LED continuously (Figure 7.6a) and run a digital calculator (Figure 7.6b) in the dark condition. The device also ran a digital watch (Figure 7.6c) under the dark condition when the two pairs of series-connected strips were connected in parallel. For the first time, we could generate

sufficient electricity from a single device to perform such practical applications without scaling up in situ with SSG.

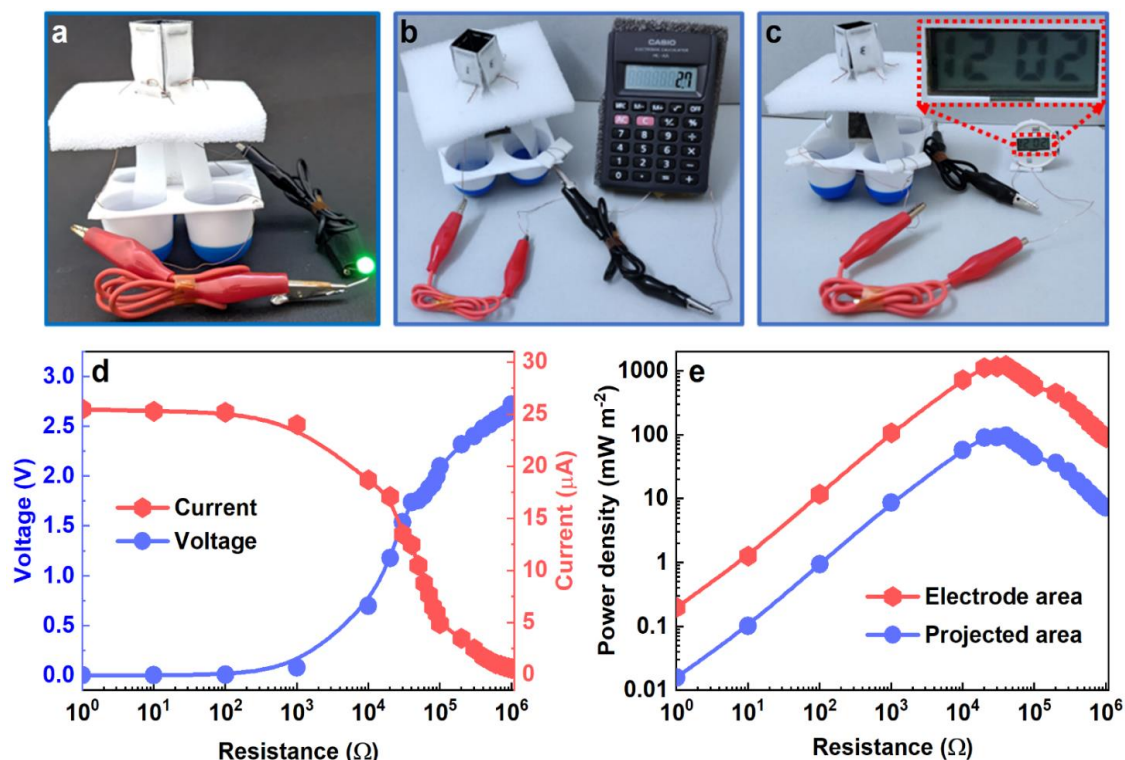


**Figure 7.6.** Optical photographs of (a) glowing green LED and (b) calculator powered by the device with all the four strips connected in a series combination. (c) Photograph of the digital watch run by the device with two pairs of series-connected strips connected in parallel. Variation of output (d) voltage and current, and (e) power density of the device measured as a function of external load resistance when all four strips were connected in series.

Further, to comprehensively characterize our device as a power source, the output performance of the device was evaluated by adding various load resistances across the output circuit when all four strips were electrically connected in series. The summarized results in Figure 7.6d show that the current drops from 26 to 0  $\mu\text{A}$ , while the voltage increases from 0 to 2.7 V with the increase in load resistance. Considering the electrode area as the active area, the maximum output power density was estimated as  $1.2 \text{ W m}^{-2}$  at a load resistance of 40 k $\Omega$ , as given in Figure 7.6e.<sup>[19]</sup> However, we feel that the illumination area will be the effective area of electricity generation, and the maximum output power of the device was  $96 \text{ mW m}^{-2}$  considering the projected area of  $1.5 \times 1.5 \text{ cm}^2$ .

Electrokinetics is a well-known phenomenon, and the origin of electricity generation within the water-conducting channels has also been extensively explained elsewhere.<sup>[18,34–39]</sup> In brief, when the microchannel of the filter paper comes in contact with an electrically neutral solution, the surface acquires some negative charge due to the negatively charged free surface

groups (such as  $-\text{COOH}$  and  $-\text{OH}$ ) of cellulose filter paper. When the ionic liquid flows through the microchannels, the negatively charged ions (co-ions) are repelled away from the surface while the positively charged ions (counter ions) are attracted towards the surface and making a static positively charged layer hence the formation of an EDL with the free surface groups, as shown in red dotted rectangles of Figure 7.7a. Due to the presence of an EDL at the solid-liquid interface, the saltwater flowing through a microchannel by capillary-driven pressure can result in a streaming potential between two ends of microchannels due to the accumulation of ions or charges.<sup>[39]</sup> So, in our case, the device uses the interactions between electrokinetics and microfluidics to directly convert the capillary-driven pressure of a liquid into electrical work.

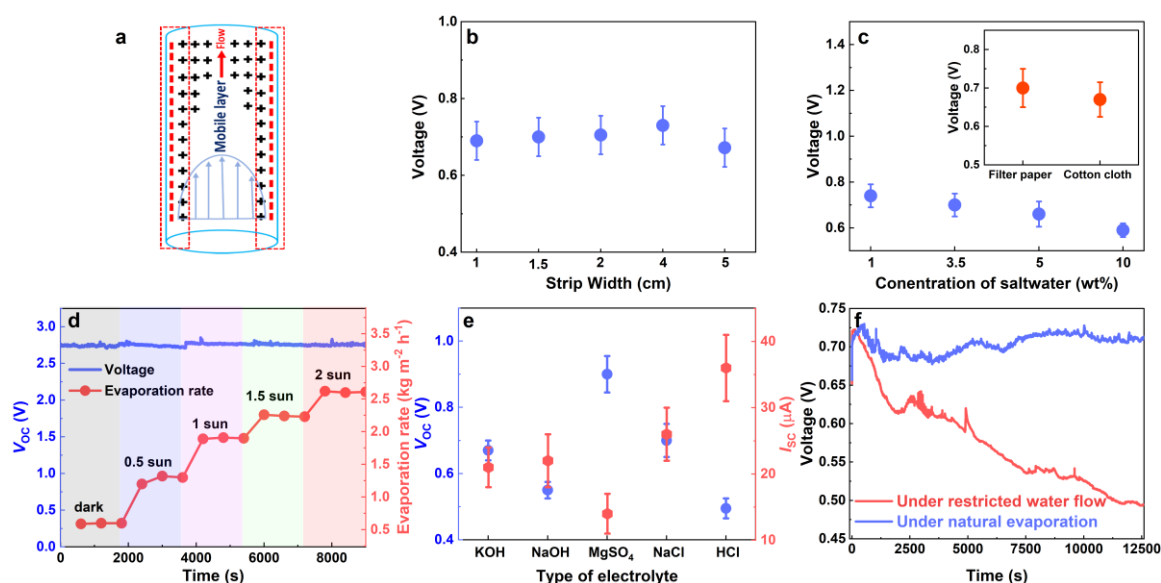


**Figure 7.7.** (a) Schematic illustration of electrolyte flow-induced streaming potential within a microchannel. (b) Variation of the  $V_{OC}$  against different strip widths. (c) Variation of the  $V_{OC}$  against different saltwater concentrations and the inset show the variation of  $V_{OC}$  with different materials. (d) Time response of  $V_{OC}$  with different flow rates originated from varying the ER with change in illumination intensities. (e) Measurement of  $V_{OC}$  and  $I_{SC}$  for different electrolyte solutions flowing through a single strip. (f) Time response of  $V_{OC}$  for a single strip with and without taping the whole strip under natural evaporation.

The effect of strip width on the  $V_{OC}$  was studied and is plotted in Figure 7.7b. The  $V_{OC}$  increases with the strip width because of the decreased channel hydraulic resistance; however, a further rise in strip width may amplify the channel impedance, reducing  $V_{OC}$ .<sup>[18]</sup> Hence to design an evaporator of a large surface area, it is recommended to use multiple strips with small widths. Moreover, the variation of  $V_{OC}$  was estimated at different concentrations of saltwater and different materials and is given in Figure 7.7c and its inset. Although a maximum  $V_{OC}$  was achieved at a lower salt concentration, we focused our experiment on 3.5 wt%, as we are dealing with seawater desalination. We also study the flow rate dependence on electricity

production by measuring the  $V_{OC}$  with different ERs achieved by changing the illumination intensities. Figure 7.7d shows that the ER increases almost linearly with the increase in solar intensities. However, the  $V_{OC}$  remained almost constant in all illumination intensities (blue line in Figure 7.7d), showing that the voltage generation is independent of the electrolyte flow rates and it only depends on the interaction between mobile ions of the electrolyte and cellulose fibres of the filter paper. Our proposition was further confirmed by using different electrolytes with similar concentrations to that of saltwater, and we found that all electrolytes can produce sufficient voltages along the microfluidic channels of the filter paper. The variation of  $V_{OC}$  with a change in electrolytes, as shown in Figure 7.7e, can be explained by the variation of the zeta potential of the filter paper.<sup>[18]</sup> However, it is important to mention that a minimum flow rate is essential to maintain a continuous voltage that can be provided by dark evaporation. Restricting the evaporation by taping the whole conducting strip leads to a drastic fall in the voltage generation, as plotted in Figure 7.7f.

## **7.4. Conclusions**

In summary, we designed two types of ISSG devices in which the saltwater was supplied via strips of filter paper which could produce freshwater and electricity simultaneously. The first device consists of a conical evaporator attached with four two-legged strips which conduct saltwater of different ionic concentrations through two legs from the reservoir to the evaporative surface. The device was able to achieve an ER of  $2.6 \text{ kg m}^{-2} \text{ h}^{-1}$  and produced a  $V_{OC}$  of 150 mV from one strip while conducting saltwater of 3.5 wt% on one leg and tap water on the other. The  $V_{OC}$  increased to 250 mV by increasing the salinity to 20 wt% without sacrificing the ER. Further, the  $V_{OC}$  of 920 mV was achieved when all four strips were connected in series producing a power density of  $9.9 \text{ mW m}^{-2}$  sufficient to fully charge the capacitors of capacitance 470 and 4700  $\mu\text{F}$  in about 20 and 33 min, which were then used to lit 1.5 V red LED. In the second device, the voltage was increased significantly by using a strip with electrodes at the top and bottom and conducting a single saltwater solution. The device consists of a cuboid-shaped evaporator made of the same SSA-coated aluminum sheet and four filter paper strips on its outer walls for water transportation. The device shows an ER of  $1.9 \text{ kg m}^{-2} \text{ h}^{-1}$  under 1 sun illumination leading to an evaporation efficiency of 88% using 3.5 wt% of saltwater. In addition, each strip can generate a  $V_{OC}$  of 0.7 V and an  $I_{SC}$  of 26  $\mu\text{A}$  both in light and dark. Further, we attained a  $V_{OC}$  of  $\sim 2.7 \text{ V}$  and an output power density of  $1.2 \text{ W m}^{-2}$  when all four strips were electrically connected in series. The output power obtained was enough to

glow a green LED and to run a calculator continuously without using any energy storage devices. This work would open a new avenue for the synergistic production of freshwater and electricity to meet the ever-increasing demand for clean water and energy.

## 7.5. References

- [1] Z.-Y. Huo, D.-M. Lee, S. Wang, Y. Kim, S.-W. Kim, *Small Methods* **2021**, *5*, 2100093.
- [2] M. Hightower, S. A. Pierce, *Nature* **2008**, *452*, 285.
- [3] T. Ding, G. W. Ho, *Joule* **2021**, *5*, 1639.
- [4] T. Ding, Y. Zhou, W. L. Ong, G. W. Ho, *Mater. Today* **2021**, *42*, 178.
- [5] X. Zhou, F. Zhao, P. Zhang, G. Yu, *ACS Mater. Lett.* **2021**, *3*, 1112.
- [6] M. Shen, X. Zhao, L. Han, N. Jin, S. Liu, T. Jia, Z. Chen, X. Zhao, *Chem. – A Eur. J.* **2022**, *28*, e202104137.
- [7] H. Wang, W. Xie, B. Yu, B. Qi, R. Liu, X. Zhuang, S. Liu, P. Liu, J. Duan, J. Zhou, *Adv. Energy Mater.* **2021**, *11*, 2100481.
- [8] P. Yang, K. Liu, Q. Chen, J. Li, J. Duan, G. Xue, Z. Xu, W. Xie, J. Zhou, *Energy Environ. Sci.* **2017**, *10*, 1923.
- [9] K. A. Bushra, K. S. Prasad, *Talanta* **2022**, *239*, 123085.
- [10] S. K. Mahadeva, K. Walus, B. Stoeber, *ACS Appl. Mater. Interfaces* **2015**, *7*, 8345.
- [11] C. Lee, S. Kim, Y.-H. Cho, *Adv. Sustain. Syst.* **2022**, *6*, 2000216.
- [12] T. Pan, S. Liu, L. Zhang, W. Xie, *iScience* **2022**, *25*, 103782.
- [13] F. Sharifi, S. Ghobadian, F. R. Cavalcanti, N. Hashemi, *Renew. Sustain. Energy Rev.* **2015**, *52*, 1453.
- [14] Y. Lin, D. Gritsenko, Q. Liu, X. Lu, J. Xu, *ACS Appl. Mater. Interfaces* **2016**, *8*, 20501.
- [15] Y. Xu, Q. Fei, M. Page, G. Zhao, Y. Ling, S. B. Stoll, Z. Yan, *iScience* **2021**, *24*, 102736.
- [16] S. M. Khan, J. M. Nassar, M. M. Hussain, *ACS Appl. Electron. Mater.* **2021**, *3*, 30.
- [17] R. K. Arun, S. Halder, N. Chanda, S. Chakraborty, *Lab Chip* **2014**, *14*, 1661.
- [18] S. S. Das, V. M. Pedireddi, A. Bandopadhyay, P. Saha, S. Chakraborty, *Nano Lett.* **2019**, *19*, 7191.
- [19] R. K. Arun, P. Singh, G. Biswas, N. Chanda, S. Chakraborty, *Lab Chip* **2016**, *16*, 3589.
- [20] C. Zhang, Y. Shi, L. Shi, H. Li, R. Li, S. Hong, S. Zhuo, T. Zhang, P. Wang, *Nat. Commun.* **2021**, *12*, 998.
- [21] T. Ding, K. Liu, J. Li, G. Xue, Q. Chen, L. Huang, B. Hu, J. Zhou, *Adv. Funct. Mater.* **2017**, *27*, 1700551.

- [22] V.-D. Dao, N. H. Vu, H.-S. Choi, *J. Power Sources* **2020**, *448*, 227388.
- [23] Y. Ding, S. Li, J. Tian, F. Wang, Y. Shi, X. Tao, X. Wang, R. Lei, X. Chen, *ACS Appl. Electron. Mater.* **2021**, *3*, 5287.
- [24] P. Xiao, J. He, F. Ni, C. Zhang, Y. Liang, W. Zhou, J. Gu, J. Xia, S.-W. Kuo, T. Chen, *Nano Energy* **2020**, *68*, 104385.
- [25] J. Liu, J. Gui, W. Zhou, X. Tian, Z. Liu, J. Wang, J. Liu, L. Yang, P. Zhang, W. Huang, J. Tu, Y. Cao, *Nano Energy* **2021**, *86*, 106112.
- [26] Y. Zhang, S. K. Ravi, S. C. Tan, *Nano Energy* **2019**, *65*, 104006.
- [27] L. Zong, M. Li, C. Li, *Nano Energy* **2018**, *50*, 308.
- [28] Z. Wei, C. Cai, Y. Huang, Y. Wang, Y. Fu, *Nano Energy* **2021**, *86*, 106138.
- [29] Z. Zheng, H. Li, X. Zhang, H. Jiang, X. Geng, S. Li, H. Tu, X. Cheng, P. Yang, Y. Wan, *Nano Energy* **2020**, *68*, 104298.
- [30] L. Zhu, T. Ding, M. Gao, C. K. N. Peh, G. W. Ho, *Adv. Energy Mater.* **2019**, *9*, 1900250.
- [31] Z. Zheng, H. Li, X. Zhang, H. Jiang, X. Geng, S. Li, H. Tu, X. Cheng, P. Yang, Y. Wan, *Nano Energy* **2020**, *68*, 104298.
- [32] Y. Xu, J. Xu, J. Zhang, X. Li, B. Fu, C. Song, W. Shang, P. Tao, T. Deng, *Nano Energy* **2022**, *93*, 106882.
- [33] X. Ma, Z. Li, Z. Deng, D. Chen, X. Wang, X. Wan, Z. Fang, X. Peng, *J. Mater. Chem. A* **2021**, *9*, 9048.
- [34] J. F. Osterle, *J. Appl. Mech.* **1964**, *31*, 161.
- [35] J. Yang, D. Y. Kwok, *Langmuir* **2003**, *19*, 1047.
- [36] H. Daiguji, P. Yang, A. J. Szeri, A. Majumdar, *Nano Lett.* **2004**, *4*, 2315.
- [37] F. H. J. van der Heyden, D. J. Bonthuis, D. Stein, C. Meyer, C. Dekker, *Nano Lett.* **2007**, *7*, 1022.
- [38] F. H. J. van der Heyden, D. J. Bonthuis, D. Stein, C. Meyer, C. Dekker, *Nano Lett.* **2006**, *6*, 2232.
- [39] J. Yang, F. Lu, L. W. Kostiuk, D. Y. Kwok, *J. Micromechanics Microengineering* **2003**, *13*, 963.

# **Chapter 8**

## **Summary and Conclusions**

In this thesis, evaporators with different photothermal materials and structural designs have been fabricated and characterized to optimize a stable ER with proper salt management, followed by a suitable condenser design to condense steam and collect freshwater as the final product. In addition to water purification, electricity was also generated simultaneously by the principle of electrokinetic voltage generation. Conducting wastewater through the water-conducting channels of ISSG, enough power was generated that could run some practical appliances directly without using any energy storage devices. The findings of this thesis take the ISSG technique a step forward toward the water-energy nexus.

Initially, a cylindrical evaporator was prepared by flaming a piece of coconut husk on an LPG stove under environmental conditions. Due to the porous nature of coconut husk, the evaporator exhibits an average light absorption of about 96% and 97.5% in dry and wet states, respectively. Under light illumination, the outer surface of the evaporator was always lower than the ambient temperature, resulting in heat harvesting from the environment. By varying the height from 0.7 to 7 cm, the maximum ER of  $3.6 \text{ kg m}^{-2} \text{ h}^{-1}$  was achieved for the evaporator of 6 cm height under 1 sun illumination and corresponding efficiency of  $>100\%$ . The evaporator also shows a good desalination performance under higher solar intensities. The salt crystals accumulated on the outer surface during the daytime were dissolved back into the bulk water during nighttime, showing the evaporator's stability and self-cleaning property. However, the back diffusion of salt crystals into the bulk water is not considered an ideal strategy as it creates problems for aquatic life and land vegetation. Also, the inefficient condensation of the FCH-based evaporator limits its practical applications. Therefore, there is a need to develop a device having an effective salt-rejecting ability and a high condensation rate.

To deal with the saltwater, a conical evaporator was designed to provide a high ER with proper salt rejection ability. The cone was made of filter paper coated with a  $\text{LaMO}_3$  ( $M = \text{Ni, Co}$ )-based photothermal material. The narrow band gap of  $\text{LaMO}_3$ , in combination with the 3D conical structure, results in the light absorption of around 95% over the full range of solar spectrum ranging from 300 to 2500 nm. Under 1 sun illumination, the evaporators made from LNO and LCO offer a maximum ER of about  $2.4 \text{ kg m}^{-2} \text{ h}^{-1}$  with a corresponding evaporation efficiency of over 88%. The salt crystals accumulated only on the top edges of the conical evaporator through proper management of the water supply during the long-term desalination process, leaving the absorber surface unaffected. The salt crystals eventually fell automatically under gravity, providing an additional opportunity for salt harvesting. Despite the above advantages, the device doesn't perform well at the high solar intensity or high salt concentration

conditions, as it requires optimized water management for different salt concentrations and illumination intensities. However, for adaptability in practical applications, the device should withstand conditions of high solar intensities and higher salt concentrations.

To deal with the high salt concentrations or high solar intensities, a conical evaporator made from an impermeable sheet of SS coated with a commercial photothermal material was developed. In such a structure, the light-absorbing surface was separated from the evaporation surface, which makes it suitable for higher solar intensities or salt concentrations. Under 1 sun illumination, the evaporator showed a stable, moderate ER of  $1.4 \text{ kg m}^{-2} \text{ h}^{-1}$  for five continuous days for saltwater of 20 wt% concentration. After 4<sup>th</sup> day there was a small decrease in the ER due to the salt accumulation on the outer surface. The ER retains its original value after removing the salt. The device also offers a linear increase in the ER with increasing solar intensities.

Finally, to collect the generated steam, a solar water purifier was designed in which the same conical evaporator was attached to a cylindrical copper condenser of the same diameter as the cone. By supplying the wastewater through the outer surface of the condenser, the device was able to collect water at a rate of  $1.4 \text{ kg m}^{-2} \text{ h}^{-1}$  under 1 sun illumination. This CR is the same as the ER of the cone in an open atmosphere, leading to the collection-to-evaporation ratio of around 100%, which remained stable at higher intensities as well. The efficient condensation of the generated steam is ascribed to the significant temperature difference between the inner surface of the condenser surface and the generated steam.

Synergistic electricity generation in ISSG is an exciting application as it provides renewable and decentralized freshwater-energy solutions. In this work, we tried to produce all-day-long electricity simultaneously with freshwater. During the desalination process, electricity was produced from the paths that transport saltwater from bulk to the absorber layer in two ways. First, a two-legged strip of Whatmann filter paper was used to conduct saltwater of different concentrations from two legs, producing a certain voltage across the electrodes deposited at the two sides perpendicular to the flow direction. Flowing 3.5 wt% of salt water (NaCl) through one leg and regular tap water on the other, the strip produces a  $V_{OC}$  of 150 mV and  $I_{SC}$  of  $6.5 \mu\text{A}$ . The  $V_{OC}$  increased to 250 mV when the concentration of saltwater was increased from 3.5 to 20 wt%. When four strips were connected in series, a  $V_{OC}$  of around 920 mV was achieved. Secondly, by flowing a single solution of salt water through a filter paper strip, the enhanced voltage was produced across the electrodes now at the top and bottom of the strip. By flowing a solution of saltwater with a concentration of 3.5 wt%, a  $V_{OC}$  of 750 mV and  $I_{SC}$   $16 \mu\text{A}$  were achieved. When four such strips were connected in series, a voltage of 2.7

V was achieved with sufficient power to run some functional appliances like an LED, calculator, or a digital watch without using any energy storage devices or any scaling up of the device.

In summary, a conical evaporator was fabricated successfully, which operates efficiently under real situations of variable solar intensity and high salt concentrations irrespective of the photothermal material. The evaporator was utilized to design a solar water purifier capable of producing freshwater at a rate of  $1.4 \text{ L m}^{-2} \text{ h}^{-1}$  and corresponding solar-to-freshwater collection efficiency of 88% at 1 sun of solar intensity. Also, simultaneous electricity was produced in ISSG, regardless of the illumination conditions, with enough power to run some practical appliances directly without using any energy storage device or scaling up the devices. The work in this thesis would open new avenues for the synergistic production of freshwater and electricity to satisfy the increasing global demands for clean water and energy.

## Scope of Future Work

In this thesis, different materials and structural designs were prepared to increase the ER along with efficient salt rejection strategies. Also, the focus of this thesis was to minimize the issues faced by conventional solar stills during the condensation process by designing a solar water purifier that condenses the steam at a rate the same as ER of the evaporator in the open atmosphere. Still, there remains enough scope for further studies in designing evaporators of high performance. The following research can be considered as the future scope of the proposed work:

1. The solar water purifier presented in this thesis produces freshwater at a low rate of  $1.4 \text{ kg m}^{-2} \text{ h}^{-1}$ , but the device was also able to condense steam generated at a high rate. Therefore, the work can be extended to design the evaporators of high ER in order to enhance the CR.
2. This thesis presents the purification of wastewater such as MO, MB, laundry, kitchen, and seawater, but there is no discussion on the purification of volatile organic compounds. Therefore, the work can be extended to fabricate such ISSG systems that effectively deal with such compounds, which is crucial for practical applications.
3. Although the thesis discussed the removal of primary salt ions like  $\text{Na}^+$ ,  $\text{Ca}^{2+}$ , and  $\text{Mg}^{2+}$  from seawater, the removal of heavy ions like  $\text{Pb}^{2+}$ ,  $\text{Pd}^{2+}$ ,  $\text{Cu}^{2+}$ , *etc.*, had been overlooked. Therefore, further studies can be carried out to design ISSG devices with the ability to separate heavy ions.

*Summary and conclusions*

4. After resolving all the abovementioned issues, developing a prototype for interface solar still for domestic use is essential.

## List of Publications

### Included in this thesis

1. **T. A. Wani**, P. Garg, and A. Bera. An Environmental Pollutant to an Efficient Solar Vapor Generator: An Eco-Friendly Method for Freshwater Production. *Materials Advances*, 2021, 2, 3856-3861.
2. **T. A. Wani**, P. Garg, S. Bera, S. Bhattacharya, S. Dutta, H. Kumar, and A. Bera. Narrow-Bandgap LaMO<sub>3</sub> (M = Ni, Co) Nanomaterials for Efficient Interfacial Solar Steam Generation. *Journal of Colloid and Interface Science*, 2022, 612, 203-212.
3. **T. A. Wani**, P. Kaith, P. Garg, and A. Bera. Microfluidic Salinity Gradient-Induced All-Day Electricity Production in Solar Steam Generation. *ACS Applied Materials & Interfaces*, 2022, 14, 35802–35808.
4. **T. A. Wani**, P. Garg, P. Kaith, and A. Bera. Freshwater-Electricity Co-Generation in Solar-Driven Water Desalination: An Effective Approach Toward Water-Energy Nexus. *Journal of Materials Chemistry A*, 2022, 10, 21273-21278.
5. **T. A. Wani**, V. Gupta. and A. Bera. In-Situ Latent Heat Transfer for Nearly 100% Condensation in Single-Stage Interfacial Solar Steam Generation. Communicated, 2023.

### Not included in this thesis

1. N. Kumar, **T. A. Wani**, P. K. Pathak, A. Bera, and R. R. Salunkhe. Multifunctional Nanoarchitected Porous Carbon for Solar Steam Generation and Supercapacitor Applications. *Sustainable Energy Fuels*, 2022, 6, 1762-1769.